



저작자표시-비영리-변경금지 2.0 대한민국

이용자는 아래의 조건을 따르는 경우에 한하여 자유롭게

- 이 저작물을 복제, 배포, 전송, 전시, 공연 및 방송할 수 있습니다.

다음과 같은 조건을 따라야 합니다:



저작자표시. 귀하는 원저작자를 표시하여야 합니다.



비영리. 귀하는 이 저작물을 영리 목적으로 이용할 수 없습니다.



변경금지. 귀하는 이 저작물을 개작, 변형 또는 가공할 수 없습니다.

- 귀하는, 이 저작물의 재이용이나 배포의 경우, 이 저작물에 적용된 이용허락조건을 명확하게 나타내어야 합니다.
- 저작권자로부터 별도의 허가를 받으면 이러한 조건들은 적용되지 않습니다.

저작권법에 따른 이용자의 권리는 위의 내용에 의하여 영향을 받지 않습니다.

이것은 [이용허락규약\(Legal Code\)](#)을 이해하기 쉽게 요약한 것입니다.

[Disclaimer](#)

이학박사 학위논문

**The sources and fates of dissolved
organic carbon in aerosols and
seawater revealed by its isotopes and
optical characteristics**

동위원소와 광학적 특성을 이용한 대기 에어로졸과
해수 중 용존유기탄소의 기원과 거동

2021 년 2 월

서울대학교 대학원

지구환경과학부

한 희 준

**The sources and fates of dissolved
organic carbon in aerosols and
seawater revealed by its isotopes and
optical characteristics**

지도 교수 김 규 범, 황 점 식

이 논문을 이학박사 학위논문으로 제출함

2020 년 10 월

서울대학교 대학원

지구환경과학부

한 희 준

한희준의 이학박사 학위논문을 인준함

2021 년 1 월

위 원 장 남 성 현 (인)

부위원장 김 규 범 (인)

위 원 황 점 식 (인)

위 원 김 태 훈 (인)

위 원 김 정 현 (인)

Abstract

The sources and fates of dissolved organic carbon in aerosols and seawater revealed by its isotopes and optical characteristics

Heejun Han

School of Earth and Environmental Sciences

The Graduate School

Seoul National University

Dissolved or water-soluble organic carbon (DOC/WSOC) in atmospheric aerosols and seawater plays a significant role in the radiative forcing of the global climate system and the global carbon cycle. DOC/WSOC is composed of a substantial portion with a light-absorbing fraction consisting of the humic matter, which absorbs in the range of ultraviolet to visible radiation, termed as brown carbon (BrC) in aerosols and colored dissolved organic matter (CDOM) in aquatic environments. Since this fraction is responsible for the optical properties, which is essential for all living organisms, and displays a conservative behavior, BrC and CDOM have been used as powerful DOM and DOC indicators in various environmental settings. Although it is crucial to study the light-absorbing organic matter to better understand the general behavior and cycling of organic carbon in

aerosols and seawater, current understandings of the production and degradation mechanisms of DOC/WSOC in the atmosphere and oceans still remain uncertain. Thus, in this study, a combination of various biogeochemical tools such as stable- and radio-carbon isotopes, optical properties of CDOM (absorbance and fluorescence), and radionuclide was used to investigate the sources, sinks, fluxes, and processes of DOC/WSOC in atmospheric aerosols and different aquatic environments.

In the atmosphere, the air mass back trajectory model combined with the fire burning activity maps found that biomass burning emission is a significant source of BrC in the urban city, Seoul, Korea. Based on yearlong monitoring, significant seasonal changes in optical and chemical properties of BrC and WSOC were found from the cold seasons (October–January) to the warm seasons (June–September). The laboratory experiment has also confirmed that photochemical degradation is an important removal mechanism of BrC in the atmosphere. Thus, photochemical degradation has a dominant role in controlling the quantity and quality of light-absorbing organic carbon in different seasons.

In Sihwa Lake, different sources and distributions of high DOC concentrations occurring in two different seasons were found based on the DOC- $\delta^{13}\text{C}$ values and spectral slope ratio. This study revealed that the higher DOC concentrations occurring in low-salinity water, which are generally believed to be from terrestrial sources, were actually from marine sediment source, while the excess DOC concentration occurring in high-salinity waters, which are generally believed to be from marine sources, were found to be from terrestrial DOM sources from the

reclaimed land area. This land-derived DOM source was likely associated with direct land-seawater interaction through the tidal inundation of seawater experiencing extended exposure to light and bacterial degradation.

The sources and fluxes of DOC over the East China Sea continental shelf were investigated based on its radiocarbon ages and $\delta^{13}\text{C}$ values of DOC and its relationship to water age deduced from ^{228}Ra . In this region, the Changjiang River appears to be the primary source of DOC in summer, while the potential source of additional DOC was found to be from the sedimentary organic matter produced in the shelf-water in winter and spring. The flux of the shelf-borne DOC was estimated to be $2.2 \pm 0.6 \text{ Tg C yr}^{-1}$, which is almost comparable to that from the Changjiang River discharge (1.6 Tg C yr^{-1}) to the East China Sea. This result suggests that the shelf-borne DOC may play a significant role in the global carbon cycle and budget.

In the East Sea, the distributions, sources, and sinks of fluorescent DOM (FDOM) were investigated. The humic-like FDOM (C and M peaks) was produced mainly by oxidation of sinking organic matter in the water column and by anaerobic processes in the bottom sediment. However, there was a large difference in the distributions of C peak (terrestrial humic-like) and M peak (marine humic-like) caused by two possible processes: (1) more effective UV degradation of C peak in the surface layer and/or (2) relatively ineffective production of M peak in the deep ocean. This result suggests that the vertical distributions of humic-like FDOM seem to be influenced by their production (water column) and photochemical degradation (surface layer) mechanisms in the

ocean.

This study has provided important implications for our understanding of and insight into the sources and fates of DOC/WSOC using multiple biogeochemical tracers in the atmosphere and various aquatic environments. Combining these tools can be further applied effectively in many different settings where the sources and nature of organic carbon are complex.

Keywords: Dissolved organic matter, dissolved organic carbon, brown carbon, stable carbon isotope, radiocarbon, optical property

Student Number: 2017-30218

Table of Contents

Abstract	1
Table of Contents.....	5
List of Tables.....	6
List of Figures	6
1. Introduction.....	11
1.1 Biogeochemistry of dissolved organic matter	11
1.2 Sources and sinks of DOC.....	11
1.3 Fluxes of DOC	14
1.4 Aim of this study	14
2. Materials and Methods.....	17
2.1 Sampling methods	17
2.2 Analsis of DOC	21
2.3 Analysis of CDOM and FDOM.....	23
2.4 Analysis of stable and radiocarbon isotopes	26
2.5 Nutients analysis	30
2.6 Analysis of radium isotope.....	33
2.7 Trace element analysis	36
3. Organic carbon in aerosols	37
3.1 Study site and sampling	37
3.2 Brown carbon composition	39
3.3 Seasonal variations in BrC and WSOC.....	40
3.4 Sources and sink of BrC	51
4. Sources of DOC in coastal ocean	64
4.1 Study site and sampling	64
4.2 Distributions of DOM in Sihwa Lake.....	65
4.3 Origin of excess DOC	69
5. Sources and fluxes of DOC in the continental shelf.....	82
5.1 Study site and sampling	82
5.2 Distributions of DOC and FDOM _H in the ECS	84
5.3 Source of DOC in the YSW.....	85
5.4 Water mixing ratios in the ECS continental shelf.....	86
5.5 Estimation of shelf-borne DOC flux.....	90
6. Distributions, sources, and sink of DOM in the marginal sea.....	99

6.1 Study site	99
6.2 Distributions of DOC and FDOM _H in the East Sea	100
6.3 Sources and sink of DOM in the East Sea	103
7. Summary and conclusions	118
Bibliography	119
Abstract (in Korean)	143
Publications and Presentations	147

List of Tables

Table 3.1 Spectral characteristics of the fluorescent components identified by the PARAFAC model for the BrC samples	46
Table 3.2 Spectral characteristics of the fluorescent components identified by the PARAFAC model for the HULIS samples	47

List of Figures

Figure 1.1 Schematic overview of the DOC sources in the atmosphere and ocean	13
Figure 1.2 Schematic overview of the research scopes of this study	16
Figure 2.1 Schematic diagram of analytical procedure for the BrC extraction ...	19
Figure 2.2 Schematic diagram of analytical procedures for the preconditioning processes of DOC, DOC- $\delta^{13}\text{C}$, DOC- $\Delta^{14}\text{C}$, CDOM, and nutrient samples ..	20
Figure 2.3 Schematic diagram of analytical procedure for the measurement of DOC concentrations	22
Figure 2.4 Schematic diagram of analytical procedure for the measurement of CDOM	25
Figure 2.5 Schematic diagram of analytical procedure for the measurement of DOC- $\delta^{13}\text{C}$ values	28

Figure 2.6 Schematic diagram of analytical procedure for the ultraviolet oxidation and DOC vacuum line system	29
Figure 2.7 Schematic diagram of analytical procedure for the measurement of nutrient concentrations.....	31
Figure 2.8 Schematic diagram of analytical procedure for the determination of major ion species using HPLC.....	32
Figure 2.9 Schematic diagram of analytical procedure for the measurement of radium isotope.....	34
Figure 2.10 Schematic diagram of analytical procedure for the measurement of ^{228}Ra activity concentrations	35
Figure 3.1 Geographical map of the study site combined with the air mass transport pathways in different seasons: spring (green), summer (red), fall (blue), and winter (brown).....	38
Figure 3.2 Schematic diagram illustrating of aerosol compositions.....	43
Figure 3.3 Fluorescence EEM spectra and excitation-emission loadings of (a) terrestrial humic-like (C1) and (b) humic-like (C2) components identified from BrC samples collected from March 2015 to January 2016 in Seoul, Korea.....	44
Figure 3.4 Fluorescence EEM spectra and excitation-emission loadings of (a) humic-like (C1), (b) protein-like (tryptophan) (C2), and (c) humic-like (C3) components identified from the HULIS samples collected from March 2015 to January 2016 in Seoul, Korea	45
Figure 3.5 Correlations of the fluorescence intensity of (a) HULIS C1 versus HULIS C2, (b) HULIS C1 versus HULIS C3, and (c) BrC C1 versus BrC C247	
Figure 3.6 Correlations of the (a) fluorescence intensity of HULIS versus DEAE column extracted HULIS concentration and the (b) fluorescence intensity of HULIS versus MeOH-BrC.....	49
Figure 3.7 Temporal variations in (a) WSOC concentration, (b) fluorescence intensity of BrC, (c) ratio of BrC to WSOC, (d) $\delta^{13}\text{C}_{\text{WSOC}}$ values, (e) levoglucosan, (f) Ca^{2+} , (g) SO_4^{2-} , (h) NO_x , (i) non-crustal K, (j) non-crustal V, (k) sea-spray concentrations, (l) UV radiation rate, and temperature from March 2015 to January 2016 in Seoul.....	58

Figure 3.8 Correlations of the concentrations of (a) WSOC concentration, (b) WSOC versus HULIS, (c) HULIS versus levoglucosan, (d) HULIS versus non-crystal K, (e) HULIS versus non-crystal V, (f) HULIS versus Ca^{2+} , (g) HULIS versus NO_x (closed circle; $r^2=0.1$, $p>0.05$) and SO_4^{2-} (open circle; $r^2=0.02$, $p<0.05$), (h) HULIS versus sea-spray, (i) HULIS versus UV radiation rate. The dashed lines represent the regression line	59
Figure 3.9 The changes of HULIS and levoglucosan concentrations for four different samples during the UV radiation (7-day) experiment	60
Figure 3.10 Fire maps obtained by using the moderate resolution imaging spectroradiometer (MODIS) fire location data provided by NASA's fire information for resource management system (FIRMS) combined with the air mass back trajectories around the study site from March 2015 to January 2016	61
Figure 3.11 Correlations of the (a) HULIS versus UV-degradable HULIS and the (b) ratio of HULIS to WSOC versus UV-degradable HULIS in different seasons: spring (green), summer (red), fall (blue), and winter (brown). The dashed lines represent the regression lines	62
Figure 3.12 The absorption coefficients of the aerosol samples collected in winter (Dec/30/15) (blue) and summer (Aug/14/15) (red). The solid lines represent the initial values for the non-irradiated samples, and the dashed lines represent the final values for the irradiated samples	63
Figure 4.1 Geographical map of sampling stations in Sihwa Lake, South Korea	74
Figure 4.2 Fluorescence EEM spectra and excitation-emission loadings of terrestrial humic-like (C1 and C3), marine humic-like (C2), and protein-like (tryptophan; C3) components identified from the PAFARAC model in Sihwa Lake	76
Figure 4.3 Vertical distributions of salinity, DO, NH_4^+ , DOC concentrations, DOC- $\delta^{13}\text{C}$ values, FDOM_C , FDOM_A , FDOM_M , FDOM_P , and S_R values in Sihwa Lake in March 2017. The dashed blocks represent stations belonging to Group 1 and 2	77
Figure 4.4 Vertical distributions of salinity, DO, NH_4^+ , DOC concentrations, DOC- $\delta^{13}\text{C}$ values, FDOM_C , FDOM_A , FDOM_M , FDOM_P , and S_R values in Sihwa	

Lake in September 2018.....	78
Figure 4.5 Correlations of the salinity versus (a) DOC concentrations, (b) FDOM _H concentrations, (c) DOC- $\delta^{13}\text{C}$ values, and (d) S_R values in Sihwa Lake in March 2017 (red square) and September 2018 (blue circle). The dashed lines represent the regression lines.....	79
Figure 4.6 Correlations of the NH_4^+ concentrations versus (a) DOC concentrations and (b) FDOM _H concentrations in Sihwa Lake in March 2017 (red square) and September 2018 (blue circle). The dashed lines represent the regression lines..	80
Figure 4.7 Schematic diagram of DOC cycling in Sihwa Lake, South Korea....	81
Figure 5.1 Maps of sampling stations, bottom topography, and schematic patterns of surface currents on the northwestern Pacific continental shelf during the sampling periods.....	93
Figure 5.2 T-S diagrams for summer 2012, winter 2017, and spring 2018 (a, d, g) DOC concentrations, (b, e, h) FDOM _H , and (c, f, i) ^{228}Ra activities are presented in different color of the symbols	94
Figure 5.3 Contour figures of (a, d, g) salinity, (b, f, j) temperature, (c, g, k) DOC, (d, h, l) FDOM _H in the surface water of the ECS continental shelf in summer 2012, winter 2017, and spring 2018. The contour plots were created using Ocean Data View software version 4. 7. 6	95
Figure 5.4 Correlations of the (a) DOC concentrations versus salinity, (b) FDOM _H versus salinity, (c) DOC concentrations versus activities of ^{228}Ra , and (d) FDOM _H versus activities of ^{228}Ra in the continental shelf waters during the sampling periods. FDOM _H and ^{228}Ra data are from Kim et al. (2018) and Lee et al. (2014). Solid lines represent regression lines, while the dashed lines represent end-member mixing lines	96
Figure 5.5 A diagram between the activities of ^{228}Ra versus salinity.....	97
Figure 5.6 Correlations between the mixing fraction, f ($f=1$ for Yellow Sea water), against concentrations of (a) DOC, (b) FDOM _H , (c) DOC- $\Delta^{14}\text{C}$, and (d) DOC- $\delta^{13}\text{C}$ values. Dashed lines represent end-member mixing lines.....	98
Figure 6.1 Map of the bottom topography and sampling stations in the East Sea	109

Figure 6.2 Map showing a sea surface temperature and sea surface height in the East Sea.....	110
Figure 6.3 Contour plots of EEMs and loadings of fluorescent components determined by the PARAFAC model in the East Sea	111
Figure 6.4 Vertical distributions of salinity, temperature, concentrations of DIN, DSi, DOC, C peak, M peak, and T peak in the upper ocean (0–200 m) in a SW–NE cross section of the East Sea	112
Figure 6.5 Vertical distributions of salinity, temperature, concentrations of DOC, C peak, and M peak in a SW–NE cross section of the East Sea.....	113
Figure 6.6 Vertical distributions of DOC, C peak, M peak, T peak, and the ratio of C peak to M peak in the East Sea	114
Figure 6.7 Map showing the concentration of chlorophyll- <i>a</i> in the surface layer of the East Sea.....	115
Figure 6.8 Scatterplots of AOU against C peak and M peak in the East Sea (200 m–bottom depth). Empty circles represent the intermediate water layer (200–750 m), and filled circles represent the deep water layer (750 m–bottom depth)	116
Figure 6.9 Schematic diagram illustrating the fluorescence intensity of excess C peak	117

1. Introduction

1.1 Biogeochemistry of dissolved organic matter

Dissolved organic matter (DOM) plays a critical role in the global biogeochemical cycle of bio-reactive elements such as carbon, a major component of biological compounds and minerals, among different reservoirs including atmosphere, land, and ocean in terms of source and sink through formation and degradation of organic matter (Hansell and Carlson, 2015; Ward et al., 2017). In DOM, most of part is made up of dissolved organic carbon (DOC), which is a major compound of Earth's organisms (Hansell and Carlson, 2015). Since carbon primarily exists as gases form (CO_2) in the atmosphere and is immediately taken up by the ocean, DOC continuously flows through the Earth's surface layer between the atmosphere and oceans (Lead, 2001). Thus, understanding of sources and characteristics of DOC in the Earth's surface layer between the atmosphere and oceans is very important.

1.2 Sources and sinks of DOC

DOC sources and sinks are diverse depending on their reservoirs (Fig. 1–1). In the atmosphere, organic aerosols occur in two different forms as primary and secondary aerosols. The primary organic aerosols are categorized into natural and anthropogenic sources (Gelencsér et al., 2007).

Natural sources are including mineral dust, soils, plants, wildfires, volcanic eruptions, and marine organics, while anthropogenic sources are involving fossil fuel combustion, biomass burning, motor vehicle emissions, industrial and agricultural particles (Gelencsér et al., 2007). On the other hand, the major sink of atmospheric particles is wet and dry deposition (Mladenov et al., 2010).

DOC is the largest pool of reduced carbon (660 Pg C) in the oceans (Hopkinson and Vallino, 2005; Hansell et al., 2009). In coastal oceans, DOC sources include (1) in-situ biological production, (2) terrestrial sources such as soils and plant matters, and (3) anthropogenic sources such as industrial and agricultural wastewater (Opsahl and Benner, 1997; Tedetti et al., 2010; Bauer and Bianchi, 2011; Griffith and Raymond, 2011; Carlson and Hansell, 2015). On the other hand, DOC is mainly produced by primary production and other sources including grazing processes, dissolution of sinking particles, and microbial production in the open ocean (Carlson and Hansell, 2015), while microbial mineralization is known as the dominant sink of DOC (Hansell et al., 2009).

Since these DOC fluxes from various reservoirs may significantly contribute to the global carbon budget, understanding these DOC sources and sinks is crucial in the global carbon budget and cycle.

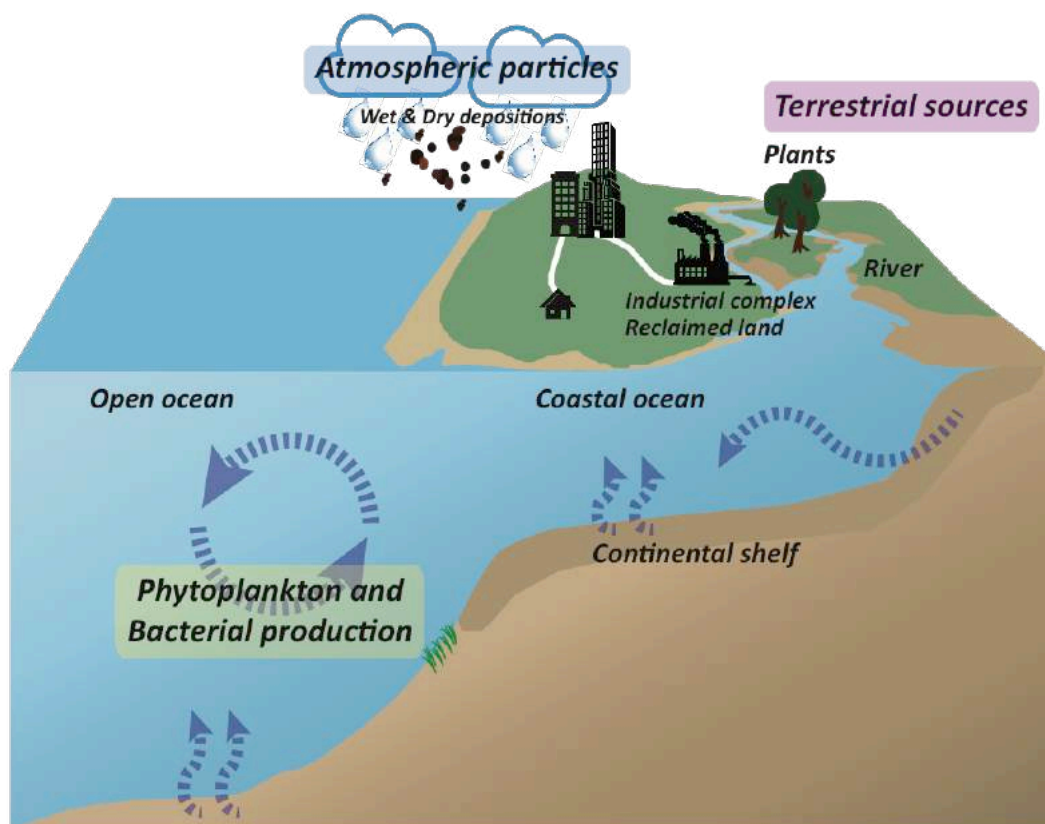


Figure 1.1 Schematic overview of the DOC sources in the atmosphere and ocean.

1.3 Fluxes of DOC

In coastal oceans, terrestrial sources of DOC transported through the atmosphere, rivers, and groundwater contribute significantly to ocean carbon budgets (Kuhlbusch, 1998; Masiello and Druffel, 1998; Raymond and Bauer, 2001a; Raymond and Bauer, 2001b; Guo and Macdonald, 2006; Yan and Kim, 2012; Huang et al., 2012; Kim et al., 2013; Lee and Kim, 2018). According to the previous studies, the global annual flux of DOC to the oceans through the river is 0.17 to 0.36 Pg C yr⁻¹, while that via groundwater system is estimated to be 0.12 Pg C yr⁻¹ (Maybeck, 1982; Dai et al., 2012; Bauer et al., 2013; Chen et al., 2018). The atmospheric deposition of total OC (dry and wet depositions) is estimated to be 0.30 to 0.64 Pg C yr⁻¹ (Willey et al., 2000; Goldstein and Galbally, 2007; Kanakidou et al., 2012; Iavorivska et al., 2016), and approximately 50% of total OC deposition occurs to the ocean surface. However, the potential role of the continental shelves where terrestrial and oceanic DOC are introduced and processes are poorly constrained.

1.4 Aims of this study

The objectives of this study are (Fig. 1–2):

- [1] To characterize the origins of organic carbon species in the atmosphere and oceans
- [2] To investigate the removal mechanism of light-absorbing

organic carbon, as known as BrC, in the atmosphere

[3] To determine the sources of excess DOC occurring in the artificial seawater lake

[4] To estimate the flux of shelf-borne DOC to the oceans

[5] To investigate the distributions, sources, and sink of FDOM in the deep ocean

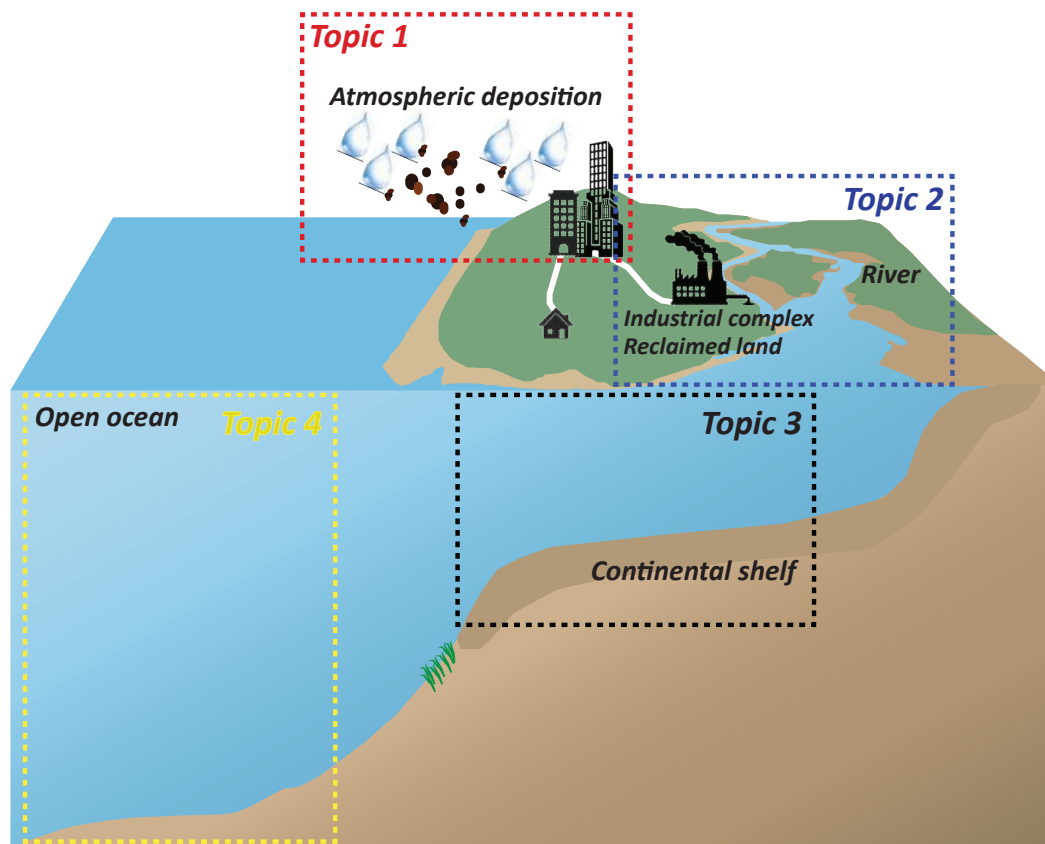


Figure 1.2 Schematic overview of the research scopes of this study.

2. Materials and Methods

2.1 Sampling methods

For the analyses of BrC in aerosols, atmospheric suspending particles must be collected using an air sampler through a pre-combusted (450 °C for 5 h) aerosol filter paper. For the BrC extraction, a portion of filter paper was cut into small pieces and placed in a pre-HCl-rinsed bottle. BrC components were extracted using a MeOH (HPLC grade; Fisher Chemical) and shaken at 125 rpm for 4 h (Wozniak et al., 2012). The extracts were filtered (pore size = 0.45 μm ; Whatman) for further analyses (Fig. 2–1).

For the seawater sampling, seawater samples were collected using a Niskin bottles mounted on a CTD rosette. During sampling, all bottles were thoroughly rinsed twice with seawater. Water samples were filtered through a pre-combusted (450°C for 5h) glass microfiber (GF/F) filter (pore size = 0.7 μm ; Whatman) and stored in an adequate container for each different analysis. Samples for DOC and DOC- $\delta^{13}\text{C}$ analyses were acidified samples to a pH ~2 with 6M HCl to avoid any bacterial activities and stored in pre-combusted glass ampoules at room temperature. Glass ampoules were fire-sealed to prevent any contamination (Fig. 2–2). Samples for DOC- $\Delta^{14}\text{C}$ analysis was stored in pre-combusted amber Boston round glass bottles at –20°C (Fig. 2–2). Samples for CDOM analysis were stored in pre-combusted

amber glass vial in a refrigerator at 4°C (Fig. 2–2). Samples for nutrient analysis were stored frozen in a HDPE bottle until analysis (Fig. 2–2).

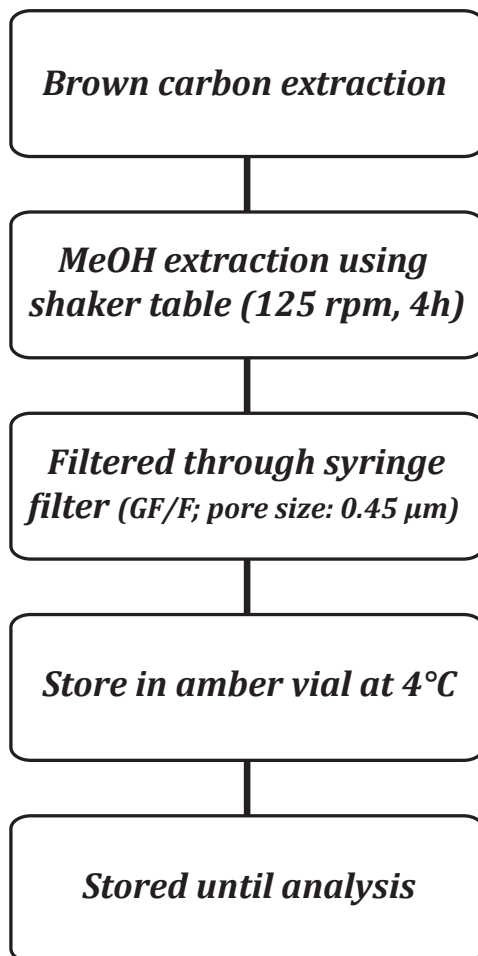


Figure 2.1 Schematic diagram of analytical procedure for the BrC extraction.

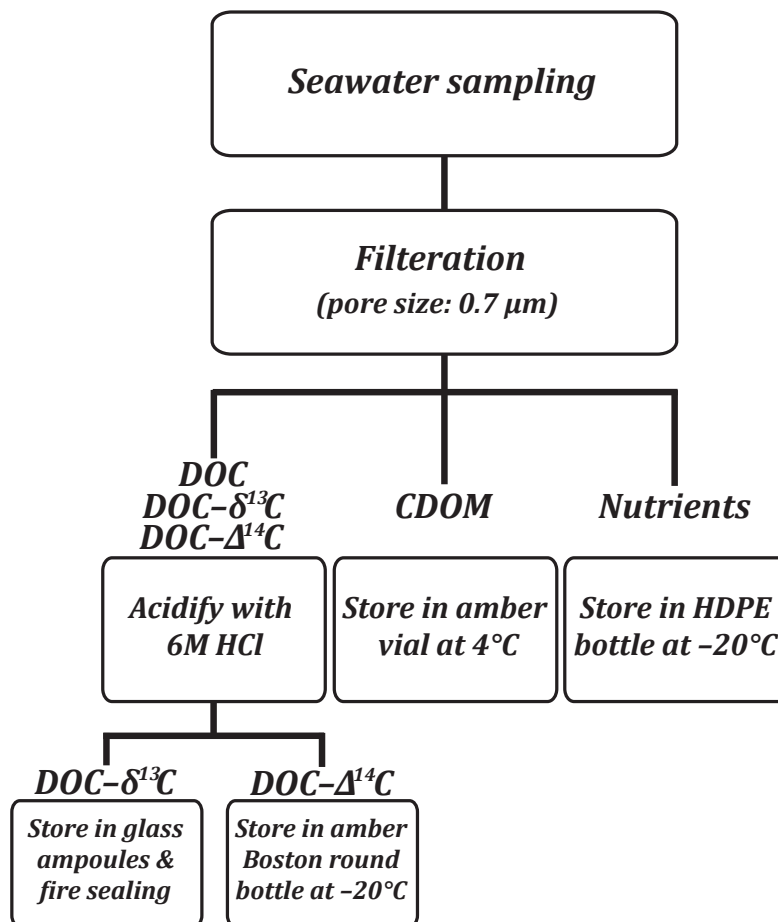


Figure 2.2 Schematic diagram of analytical procedure for the preconditioning processes of DOC, DOC- $\delta^{13}\text{C}$, DOC- $\Delta^{14}\text{C}$, CDOM, and nutrient samples.

2.2 Analysis of DOC

DOC concentrations were measured by a high temperature catalytic oxidation (HTCO) method using a total organic carbon (TOC) analyzer (TOC-V_{CPH} and TOC-L; Shimadzu, Japan) (Fig. 2–3). The analytical uncertainties were $\pm 2 \mu\text{M}$ for a consensus reference material (CRM) of deep seawater (DSR; $\sim 43 \mu\text{M}$, University of Miami; Hansell Organic Biogeochemistry Lab) based on multiple analyses (approximately three times per each sample batch) (Hansell, 2005). Calibration curve was produced using a standard solution of potassium hydrogen phthalate (KHP) stock solutions.

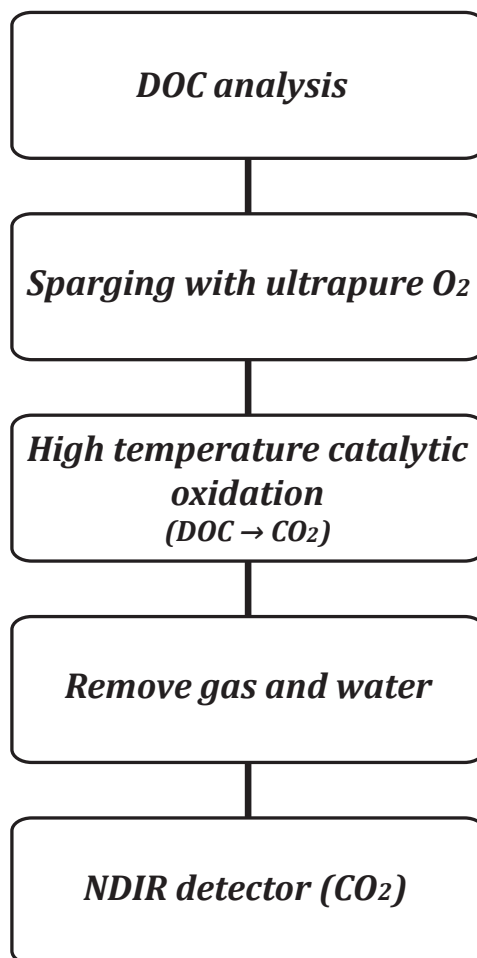


Figure 2.3 Schematic diagram of analytical procedure for the measurement of DOC concentrations.

2.3 Analysis of CDOM and FDOM

Fluorescence and absorbance optical properties of CDOM were determined using a spectrophotometer (Aqualog, Horiba) (Fig. 2–4). For FDOM analysis, emission-excitation matrix (EEM) data were measured using emission and excitation wavelength in the range of 240–700 and 250–500 nm, respectively, with scanning intervals of 1 to 5 nm. In addition, the ranges of emission and excitation wavelengths and the scanning intervals depend on optical measurements used for each analysis. The blank subtraction, Raman, and Rayleigh scattering signals were corrected using Milli-Q water (18.2 MΩcm) daily. The parallel factor analysis (PARAFAC) model was applied to characterize the major fluorescent components using the Solo software. The inner-filter effect was corrected using the Solo software (Han et al., 2020). The model results were validated by split-half analysis and random initialization (Bro, 1997; Zepp et al., 2004; Stedmon and bro, 2008). Since the fluorescence intensity of DOM is highly instrument dependent, a simple method for standardization is required. The fluorescence intensity was normalized by Raman peak area of pure Milli-Q water and presented as Raman unit (RU), which is the integrated area of water Raman peak at an excitation wavelength of 350 nm (Lawaetz and Stedmon, 2009; Han et al., 2020).

The absorption spectra of the samples were measured with a scanning

wavelength range of 240–700 nm. The optical indices and parameters were estimated using the absorbance measurement equations.

The absorption coefficient was calculated using the following equation:

$$a_{\lambda} = 2.303 A_{\lambda} / l, \quad (1)$$

where a is the absorption coefficient (m^{-1}), A_{λ} is the absorbance, and l is the optical path length of the quartz cuvette (m). The spectral slope ratio (S_R) was calculated with the ratio of spectral slope (S) of shorter wavelengths ($S_{275-295}$) to longer wavelengths ($S_{350-400}$) using the following equation:

$$a_{\lambda} = a_{\lambda_{\text{ref}}} e^{-S(\lambda - \lambda_{\text{ref}})}, \quad (2)$$

where a is the Napierian absorption coefficient (m^{-1}), λ is the wavelength, and λ_{ref} is the reference wavelength (Twardowski et al., 2004; Helms et al., 2008; Han et al., 2020).

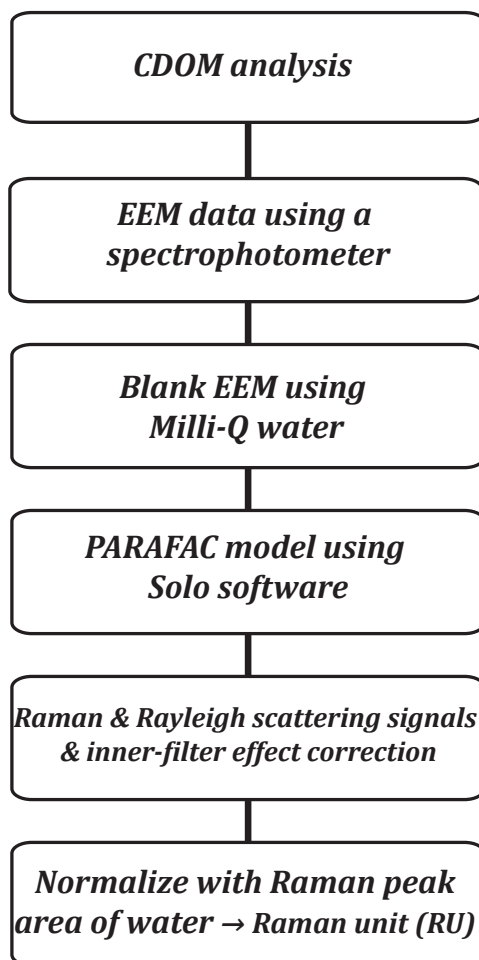


Figure 2.4 Schematic diagram of analytical procedure for the measurement of CDOM.

2.4 Analysis of stable and radiocarbon isotopes

Stable carbon isotope of DOC ($\text{DOC-}\delta^{13}\text{C}$) was measured using an isotope ratio mass spectrometer (IRMS) (Isoprime, Elementar) connected with a TOC analyzer (TOC-IRMS) (Fig. 2–5). After sample solution passed the combustion tube for the HTCO method, CO_2 gases from the non-dispersive infrared sensor (NDIR) in TOC analyzer was introduced to IRMS via an interface (isoTOCinterface, Elementar), which removes O_2 gases and trap CO_2 gases (Panetta et al., 2008; Troyer et al., 2010; Han et al., 2020). The $\delta^{13}\text{C}$ values were determined using the following equation:

$$\delta^{13}\text{C} = \left(\frac{(^{13}\text{C}/^{12}\text{C})_{\text{sample}}}{(^{13}\text{C}/^{12}\text{C})_{\text{standard}}} - 1 \right) \times 1000\text{‰} \quad (3)$$

The isotopic composition $\delta^{13}\text{C}$ is reported as Vienna Pee Dee Belemnite (VPDB) scale (Troyer et al., 2010).

Prior to the sample analysis, analytical test was conducted on certified IAEA-CH6 sucrose ($\delta^{13}\text{C} = -10.45 \pm 0.03\text{‰}$; International Atomic Energy Agency), reference material of deep seawater (DSR; $\delta^{13}\text{C} = -21.5 \pm 0.1\text{‰}$; University of Miami), and Suwannee River Fulvic Acid (SRFA) ($\delta^{13}\text{C} = -27.6 \pm 0.12\text{‰}$; International Humic Substances Society) to evaluate the precision of the measurements (Hansell, 2005; Lang et al., 2007; Panetta et al., 2008; Troyer et al., 2010; Han et al., 2020).

Radiocarbon isotope ratio of DOC ($\text{DOC}-\Delta^{14}\text{C}$) sample was measured by UV oxidation method (Beaupre et al., 2007) (Fig. 2–6). $\text{DOC}-\Delta^{14}\text{C}$ samples were acidified to $\sim\text{pH } 2$ with 85% phosphoric acid, purged with ultra-high purity nitrogen gas to remove dissolved inorganic carbon, and oxidized by UV irradiation (Beaupre et al., 2007) (Fig. 2–6). After the irradiation, the resultant CO_2 gas was analyzed for at the National Ocean Sciences Accelerator Mass Spectrometry Facility (NOSAMS) at the Woods Hole Oceanographic Institution.

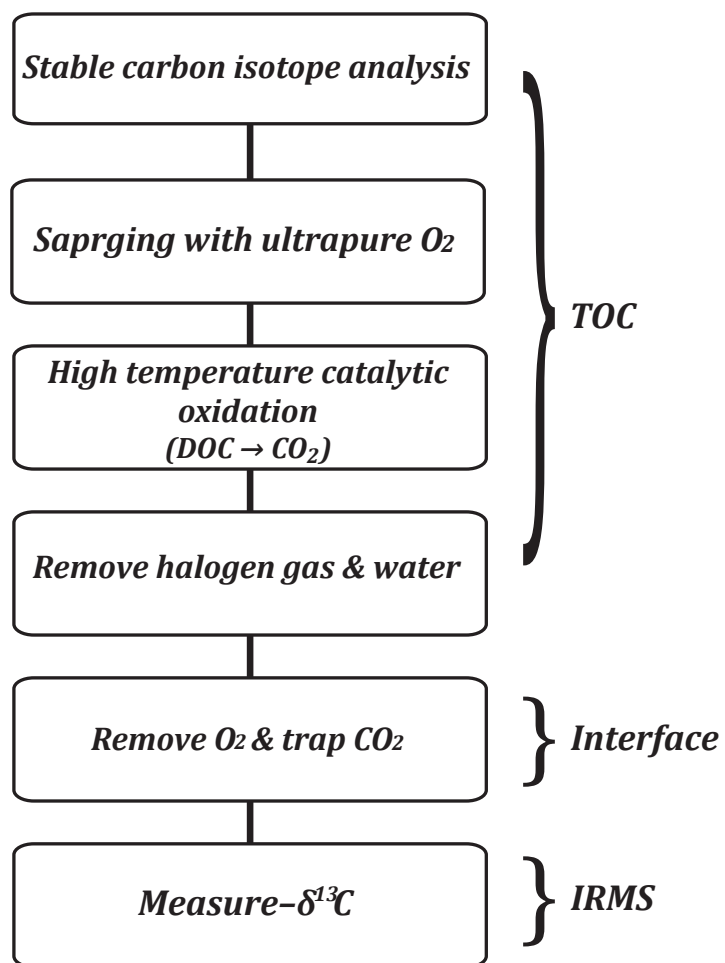


Figure 2.5 Schematic diagram of analytical procedure for the measurement of DOC- $\delta^{13}\text{C}$ values.

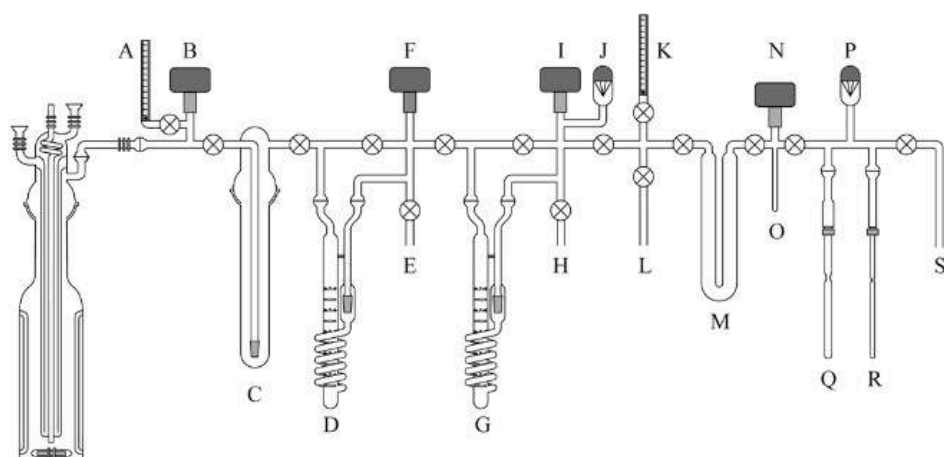


Figure 2.6 Schematic diagram of analytical procedure for the ultraviolet oxidation and DOC vacuum line system (Beaupre et al., 2007).

2.5 Nutrients analysis

Inorganic and organic nutrients were measured using a nutrient auto-analyzer (QuAatro39, SEAL analytical) (Fig. 2–7). Dissolved inorganic nitrogen (DIN) includes NO_2 , NO_3 , and NH_4^+ . Dissolved inorganic phosphate (DIP) includes PO_4^{2-} . Dissolved inorganic silicate (DSi) includes SiO_4 . The analytical uncertainties were <5% for the reference materials (KANTO).

For the analysis of cation (Na^+ , NH_4^+ , K^+ , and Ca^+) and anion (Cl^- , SO_4^{2-} , NO_3^- , and NO_2^-) species, high-performance liquid chromatography (HPLC) (Waters 2695) equipped with a conductivity detector (Waters 432) was used (Fig. 2–8). Cations were analyzed using a 0.1 mmol L^{-1} ethylenediaminetetraacetic acid (EDTA) and $3.0 \text{ mmol L}^{-1} \text{ HNO}_3$ as an eluent with a constant flow rate of 1.0 mL min^{-1} and a Waters IC-Pak C M/D column ($3.9 \text{ mm} \times 150 \text{ mm}$) was used. Anions were analyzed using a borate/gluconate eluent with a constant flow rate of 2.0 mL min^{-1} and a Waters IC-Pak A HC column ($4.6 \text{ mm} \times 150 \text{ mm}$) was used. The temperature of columns were maintained at 30°C and samples were at 4°C .

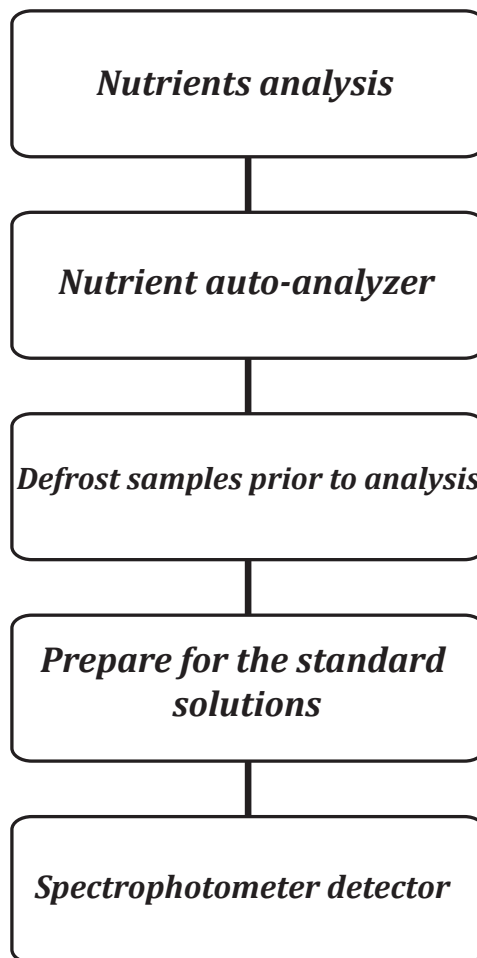


Figure 2.7 Schematic diagram of analytical procedure for the measurement of nutrient concentrations.

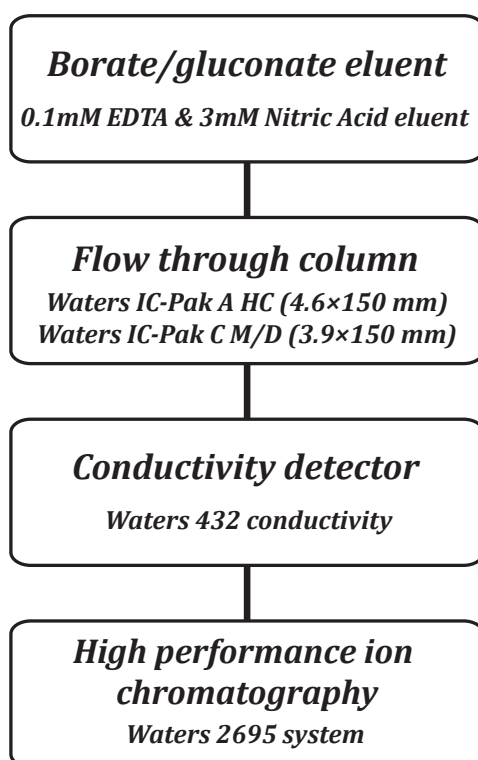


Figure 2.8 Schematic diagram of analytical procedure for the determination of major ion species using HPLC.

2.6 Analysis of radium isotope

For ^{228}Ra measurement, 100L of seawater samples were collected in polypropylene cubitainers. Then, the seawater sample was passed through a column of acrylic fiber impregnated with MnO_2 , as known as Mn-fiber, at $<1 \text{ L min}^{-1}$ by gravity (Moore, 1976). The Mn-fiber was brought to the laboratory for further analysis (Fig. 2–9). The Mn-fiber was rinsed with Ra-free deionized water to wash out any salts or particles, then ashed at 820°C for 16 h. The ashed Mn-fiber was transferred to hermetically sealed vials and analyzed for ^{228}Ra using a high-purity Germanium well-type detector (CANBERRA) (Fig. 2–10). ^{228}Ra activities were determined by counting the gamma peaks at 911 keV from its daughter ^{228}Ac (Kim et al, 2003). The geometry effect on the detection efficiency was corrected and applied to the final activity calculation.

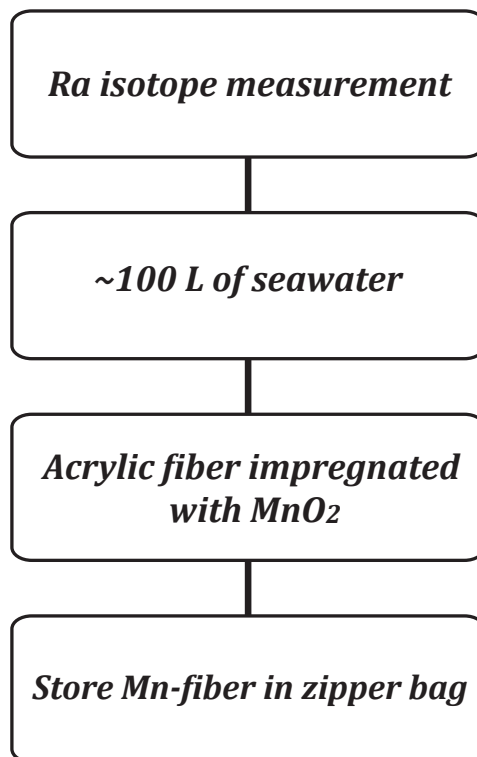


Figure 2.9 Schematic diagram of analytical procedure for the preconditioning process of radium isotope.

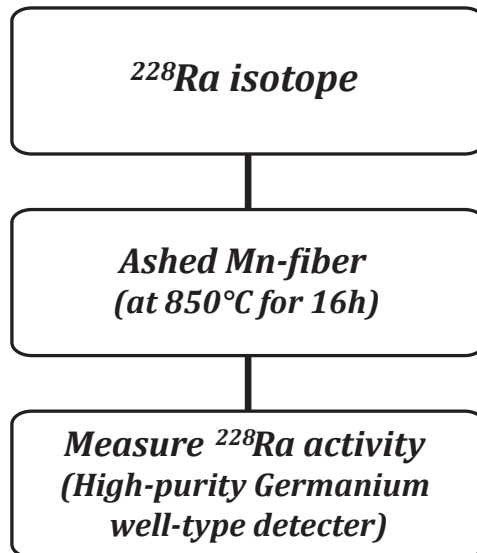


Figure 2.10 Schematic diagram of analytical procedure for the measurement of ²²⁸Ra activity concentrations.

2.7 Trace element analysis

The trace element samples were analyzed using a high-resolution inductively coupled plasma mass spectrometer (HR-ICP-MS) (Thermo Element 2). In order to correct the instrumental instability for the mass spectrometer, rhodium (Rh) was included as an internal standard prior to analysis. The trace element samples were acidified to 2% ultra-pure HNO₃.

The non-crustal element fractions [X] were estimated using the following equation (Yan and Kim, 2012):

$$[non - crustal X] = [X] - ([X]/[Al])_{crust} \times [Al]_{aerosol} \quad (4)$$

where the element compositions of the upper continental crust for potassium (K), aluminum (Al), and vanadium (V) are applied (Taylor and McLennan, 1995).

3. Organic carbon in aerosols

3.1 Study site and sampling

Seoul (37.5°N, 127.0°E) is the capital city of South Korea and one of the largest metropolitan cities in the world (Fig. 3–1). South Korea has been significantly affected by severe dust storms called Asian dust or the Yellow dust mostly originated from the Chinese and Mongolian deserts during the spring (Mar–May) and often during the winter (Dec–Jan) (Lin et al., 2012). Recently, significant increases in fine aerosols associated with anthropogenic emissions are of great concern and a focus of major environmental studies in this region (Seinfeld et al., 2004; Park et al., 2007).

Aerosol samples ($n=78$) were collected using a high-volume air sampler (HV-1000, SHIBATA) from March 2015 to January 2016 in Seoul city of South Korea (20 m above ground level) (Fig. 3–1). Aerosol samples were collected for 24 h at a constant flow rate of 1000 L min⁻¹ using a pre-combusted (450 °C for 5 h) glass microfiber filter paper (GF/F, 8 × 10 inch, 2 µm pore size, Whatman). For the blank sample, a filter paper was exposed shortly at the study site and analyzed in the same manner as those for the collected samples.

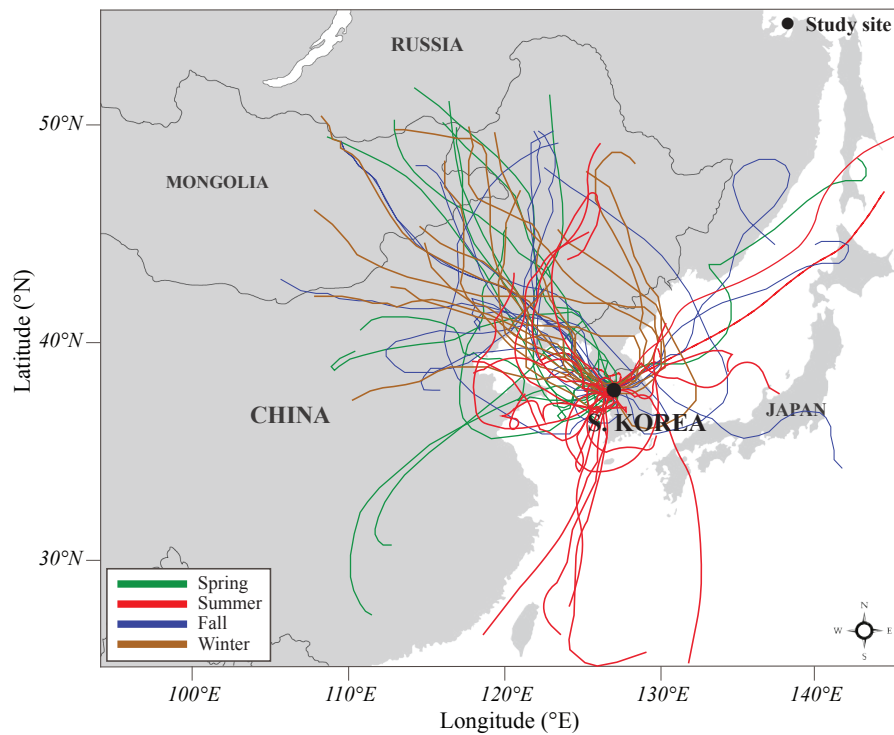


Figure 3.1 Geographical map of the study site combined with the air mass transport pathways in different seasons: spring (green), summer (red), fall (blue), and winter (brown).

3.2 BrC composition

Organic aerosols play an important role in air quality, atmospheric chemistry, and the global climate system (Ghan and Schwartz, 2007; Duarte and Duarte, 2013; Laskin et al., 2015). Organic aerosols are composed of a significant fraction with carbonaceous organic aerosols absorbing radiation, which is called the light-absorbing organic aerosols (Laskin et al., 2015). Recently, the light-absorbing organic aerosols, also known as brown carbon (BrC), have attracted great attention due to their significant roles in the radiative forcing affecting the global climate system by directly absorbing solar radiation and indirectly acting as cloud condensation nuclei (CCN) for cloud formation in the atmosphere (Kanakidou et al., 2005; Andreae and Gelencsér, 2006; Graber and Rudich, 2006; Ramanathan et al., 2007; Kirillova et al., 2014a; Saleh et al., 2014). The light-absorbing property of BrC is expected to be considerably weaker than that of the black carbon (BC), which is the best known light-absorbing carbonaceous aerosol, since BrC absorbs solar radiation in the range of ultraviolet (UV) to visible wavelengths, while BC absorbs over a wide spectral range from UV to near-infrared radiation (Feng et al., 2013; Laskin et al., 2015). However, BrC contributions would be significant in the atmosphere due to its higher abundances over source regions (Hoffer et al., 2006; Gustafsson et al., 2009; Feng et al., 2013). In addition, BrC contributes approximately 19% of the total atmospheric radiative forcing (Feng et al., 2013).

The origin of BrC is predominantly attributed to atmospheric humic-like substance (HULIS) due to their similar properties to terrestrial and aquatic humic and fulvic acids in aquatic environment (Andreae and Gelencsér, 2006; Graber and Rudich, 2006; Lukács et al., 2007; Laskin et al., 2015; Yan and Kim, 2017) (Fig. 3–2). The major source of HULIS includes both direct emission sources including biomass burning, marine aerosols, and soil re-suspension and indirect contribution from secondary formation in the atmosphere (Graber and Rudich, 2006; Hoffer et al., 2006; Lin et al., 2010; Yan and Kim, 2017). Recently, residential coal combustion was suggested as another important source of HULIS during cold seasons in many studies (Tan et al., 2016; Voliotis et al., 2017; Li et al., 2019). In addition, biological aerosols such as bacteria, algae, pollen, spores, fungi, plant debris, and animal tissue are another important sources of BrC in the atmosphere (Després et al., 2012; Pöhlker et al., 2012). Previous studies have suggested that the atmospheric HULIS contributes to ~70% of the water-soluble organic carbon (WSOC) (Laskin et al., 2015; Park and Son, 2017), while the WSOC contributes to 10 to 80% of the total organic carbon contents in aerosols (Kirillova et al., 2014a; Kirillova et al., 2014b; Fu et al., 2015) (Fig. 3–2). However, current understandings of the optical and chemical properties, and removal mechanism of light-absorbing organic aerosols are poorly understood.

The light-absorbing property of BrC was differentiated using its fluorescent property by the PARAFAC model. The PARAFAC model identified two humic-like fluorescent components in BrC samples, while the model identified two humic-like and one protein-like fluorescent component in HULIS samples (Figs. 3–3 and 3–4). In BrC samples, component 1 (C1; Ex/Em = 356/439 nm) and component 2 (C2; Ex/Em = 284/373 nm) are known to be highly associated with the atmospheric HULIS as well (Chen et al., 2016; Yan and Kim, 2017) (Table 3.1). In HULIS samples, component 1 (C1; Ex/Em = 305/416 nm) and component 3 (C2; Ex/Em = 365/484 nm) are known to be associated with the atmospheric HULIS (Chen et al., 2016; Yan and Kim, 2017) (Table 3.2). Component 2 (C2; Ex/Em = 290/340 nm) represents a protein-like peak associated with a biological production (Coble, 2007; Murphy et al., 2014) (Table 3.2).

In this study, C1 was used as a representative fluorescent component since C1 versus C2 ($r^2 = 0.9$; $p < 0.05$) and C1 versus C3 ($r^2 = 0.8$; $p < 0.05$) of HULIS and C1 versus C2 ($r^2 = 0.9$; $p < 0.05$) of BrC exhibited good correlations each (Fig. 3–5). In HULIS sample, a good correlation between C1 and C2 was found in the HULIS samples, although, in general, these two components have different sources and sinks in the atmosphere (Yan and Kim, 2017) (Fig. 3–5a).

In addition, the HULIS component (C1) obtained by the PARAFAC model agreed very well with the extracted HULIS concentration obtained by using the DEAE column ($r^2 = 0.81$; $p < 0.05$), indicating that the C1 fluorescent component represents the actual HULIS (Fig. 3–6a). Also, the extraction efficiencies of HULIS (water-soluble BrC) to that of the MeOH-soluble BrC were compared (Fig. 3–6b). Although the efficiency of the water-soluble BrC was approximately 20% lower than that of the MeOH-soluble BrC, they exhibited a good correlation ($r^2 = 0.9$; $p < 0.05$) (Fig. 3–6b). Therefore, this result conclude that the HULIS is a good representative of BrC.

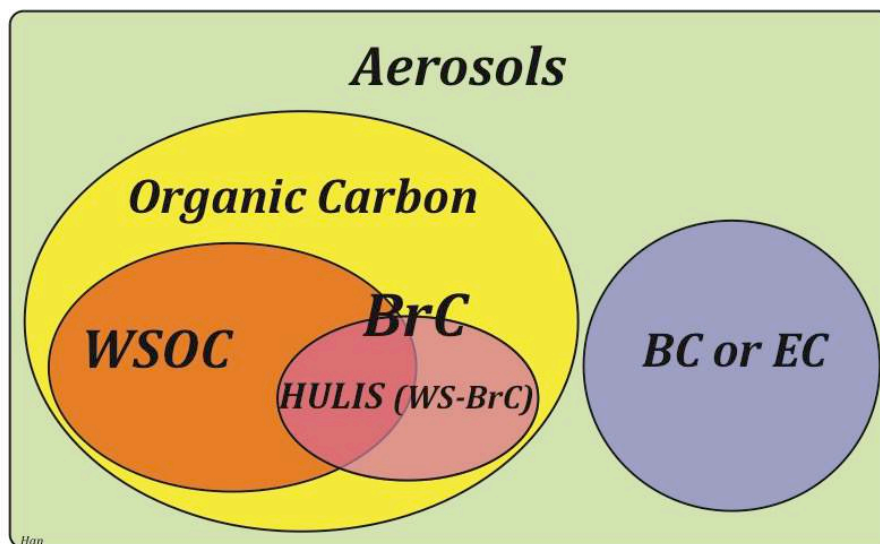


Figure 3.2 Schematic diagram illustrating of aerosol compositions.

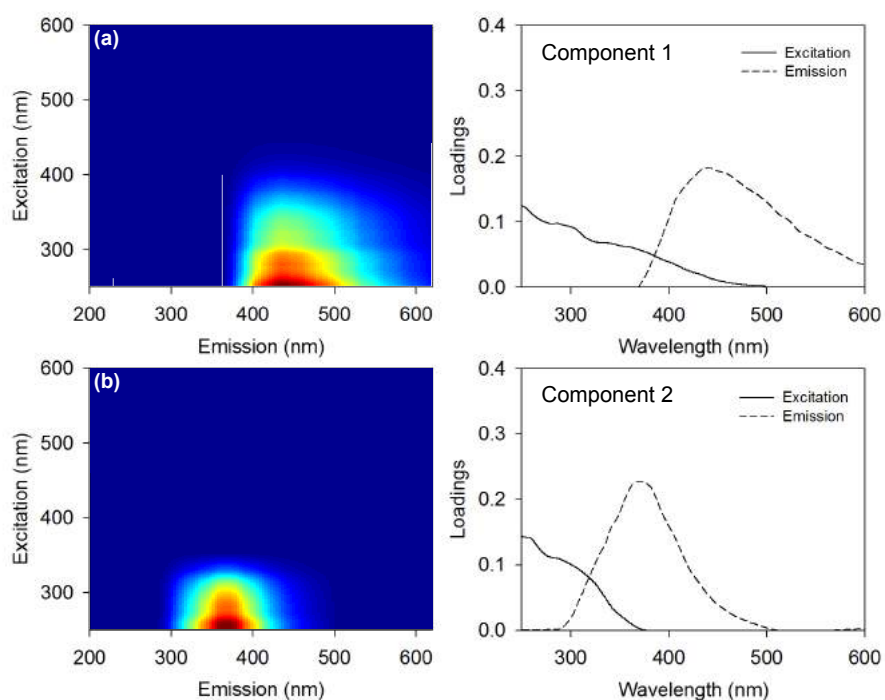


Figure 3.3 Fluorescence EEM spectra and excitation-emission loadings of (a) terrestrial humic-like (C1) and (b) humic-like (C2) components identified from BrC samples collected from March 2015 to January 2016 in Seoul, Korea.

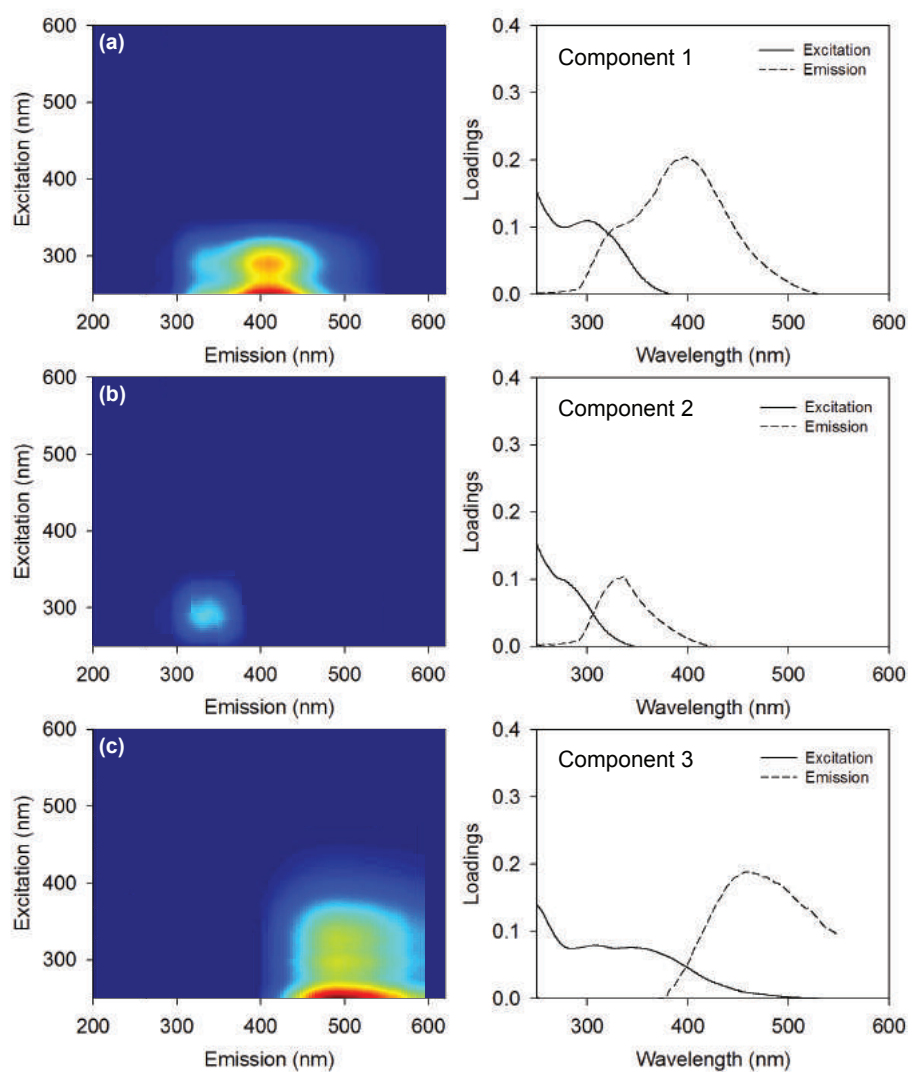


Figure 3.4 Fluorescence EEM spectra and excitation-emission loadings of (a) humic-like (C1), (b) protein-like (tryptophan) (C2), and (c) humic-like (C3) components identified from the HULIS samples collected from March 2015 to January 2016 in Seoul, Korea.

Table 3.1 Spectral characteristics of the fluorescence components identified by the PARAFAC model for the BrC samples.

Component	Ex/Em wavelength [nm]	Peak	Description and origin
C1	356/439	C	Terrestrial humic-like component (Stedmon and Markager, 2005); HULIS (Xie et al., 2020)
C2	284/373	M	Marine humic-like component (Stedmon and Markager, 2005); HULIS (Pöhlker et al., 2012)

Table 3.2 Spectral characteristics of the fluorescence components identified by the PARAFAC model for the HULIS samples.

Component	Ex/Em wavelength [nm]	Peak	Description and origin
C1	305/416	M	Marine humic-like component (Stedmon and Markager, 2005); HULIS (Pöhlker et al., 2012)
C2	290/340	T	Protein-like (tryptophan-like) component derived from autochthonous processes (Stedmon and Markager, 2005; Pöhlker et al., 2012)
C3	365/484	C	Terrestrial humic-like component (Stedmon and Markager, 2005); HULIS (Xie et al., 2020)

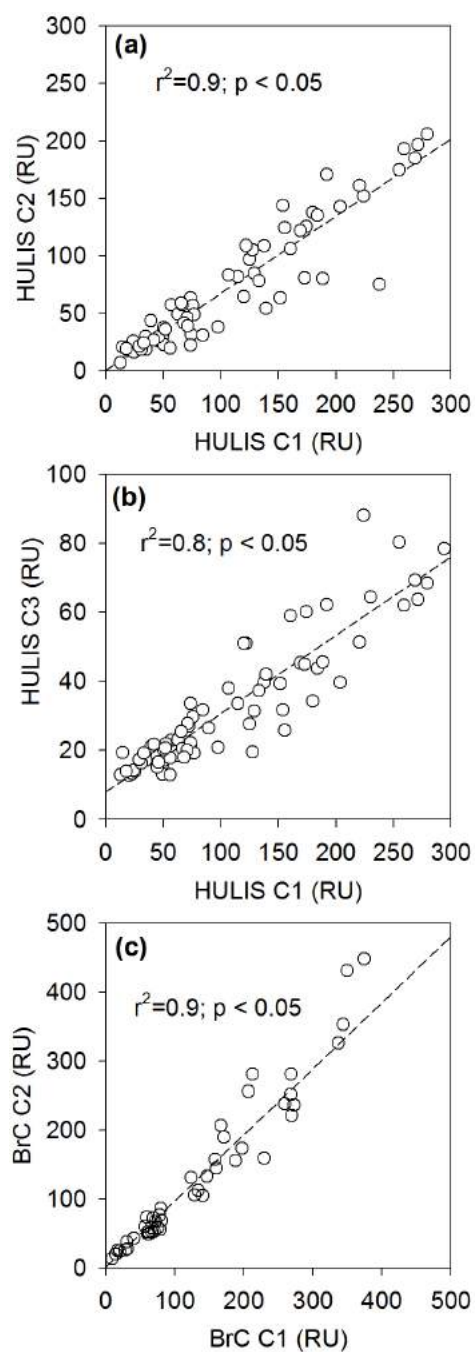


Figure 3.5 Correlations of the fluorescence intensity of (a) HULIS C1 versus HULIS C2, (b) HULIS C1 versus HULIS C3, and (c) BrC C1 versus BrC C2.

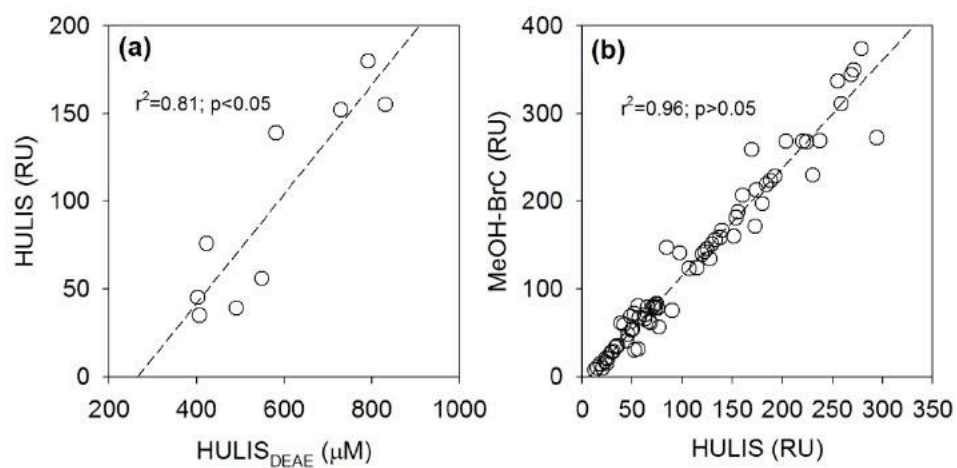


Figure 3.6 Correlations of the (a) fluorescence intensity of HULIS versus DEAE column extracted HULIS concentration and the (b) fluorescence intensity of HULIS versus MeOH-BrC.

3.3 Seasonal variations in BrC

The BrC concentrations showed seasonal variations in the range of 8–554 RU (average = 130 ± 107 RU) with higher values during the cold seasons (Oct–Jan) (average = 191 ± 119 RU) and lower values during the warm seasons (Jun–Sep) (average = 44 ± 23 RU) (Fig. 3–6). The concentrations of WSOC and HULIS showed similar seasonal variations from 3 to $40 \mu\text{g m}^{-3}$ (average = $16 \pm 7 \mu\text{g m}^{-3}$) and from 13 to 294 RU (average = 108 ± 77 RU), respectively (Fig. 3–6). The ratio of BrC to WSOC content showed similar seasonal trend with BrC and WSOC concentrations indicating that there was pronounced decrease in the average fraction of BrC relative to WSOC from the cold to the warm seasons (Fig. 3–6).

The $\delta^{13}\text{C}_{\text{WSOC}}$ values were in the range of -21.0 to -27.5% (average = $-24.0 \pm 1.5\%$), with no seasonal variation trend (Fig. 3–6). The levoglucosan concentration ranged from 0.5 to $2.2 \mu\text{g m}^{-3}$ (average = $1.1 \pm 0.5 \mu\text{g m}^{-3}$) with comparatively higher values during the cold seasons (Oct–Jan) and the lower values during Aug–Sep (Fig. 3–6). The temporal variations in major ion species' concentrations did not show such seasonal variations throughout the year (Fig. 3–6). The temporal variation in Ca^{2+} concentration (average = $0.8 \pm 0.2 \text{ mg L}^{-1}$) showed a relatively constant trend throughout the year (Fig. 3–6). The SO_4^{2-} concentrations (average = $12.0 \pm 10.3 \text{ mg L}^{-1}$) showed the highest values during the period of spring to summer and were

slightly decreased during the cold seasons (Fig. 3–6). The NO_x concentrations (average = $11.7 \pm 8.7 \text{ mg L}^{-1}$) were relatively high during the warm seasons (Jun–Oct) (Fig. 3–6). The concentration of non-crustal K (average = $0.4 \pm 0.2 \text{ mg L}^{-1}$) also showed a relatively constant trend throughout the year (Fig. 3–6). The non-crustal V concentrations (average = $0.01 \pm 0.01 \text{ mg L}^{-1}$) showed no such seasonal variations throughout the year (Fig. 3–6). The sea-spray concentrations were in the range of 4.0–33.6 mg L^{-1} (average = $17.3 \pm 6.4 \text{ mg L}^{-1}$), showing the highest concentration in July (Fig. 3–6). Both temperature and UV radiation rate were high during the warm seasons and low during the cold seasons, showing typical patterns of middle latitudes (Fig. 3–6).

3.4 Sources and sink of BrC

In order to identify the potential sources of BrC, the source of WSOC was investigated based on the $\delta^{13}\text{C}_{\text{WSOC}}$ values together with various chemical constituents. The annual average $\delta^{13}\text{C}_{\text{WSOC}}$ ($-24.0 \pm 1.5\text{‰}$) value suggests that the biomass burning activity of terrestrial C3 plant-origin materials including grassland, crop-residue, fuel-wood could be a dominant source in this region (Kelly et al., 2005; Das et al., 2010; Kawashima and Haneishi, 2012; Fu et al., 2015). The average $\delta^{13}\text{C}_{\text{WSOC}}$ was in good agreement with that of HULIS ($-25.4 \pm 1.6\text{‰}$) reported from the previous study on rainwater in Seoul, Korea (Yan and Kim, 2017).

The WSOC and WSON concentrations showed a good correlation ($r^2 = 0.6$; $p > 0.05$) indicating that these two variables are highly associated with a common organic source in this region (Yan and Kim, 2015) (Fig. 3–7). The WSOC and HULIS concentrations also showed a good correlation ($r^2 = 0.5$; $p < 0.05$) indicating the WSOC is mostly consisting of HULIS in this region (Fig. 3–7). HULIS showed a good correlation with the levoglucosan concentrations ($r^2 = 0.5$; $p < 0.05$), which is a biomarker tracing the biomass burning in the atmosphere, indicating that biomass burning is a significant source of HULIS in this region (Fu et al., 2015; Kuang et al., 2015) (Fig. 3–7). This result is consistent with the previous study of BrC in Seoul, which has suggested that the BrC in the rainwater was primarily derived from biomass burning and terrestrial biogenic emissions ($>70\%$) based on the ^{14}C measurements in the HULIS (Yan and Kim, 2017). However, significant decreases ($35 \pm 2\%$) in levoglucosan concentrations by the UV irradiation experiment were observed (Fig. 3–8). This is also consistent with the previous finding that levoglucosan could be easily oxidized by the hydroxyl radical in the atmosphere (Hennigan et al., 2010; Hoffmann et al., 2010). Thus, the major source of HULIS was derived from biomass burning activity in this region. However, such low concentrations in WSOC and HULIS in summer could not be evaluated by using the levoglucosan biomarker in this case.

In order to evaluate the effect of biomass burning activity during the study period, we compiled the fire maps obtained from the Moderate Resolution Imaging Spectroradiometer (MODIS) fire location data provided by NASA's Fire Information for Resource Management System (FIRMS) in combination with the air mass back trajectory model provided by National Oceanic and Atmospheric Administration (NOAA) Air Resources Laboratory (Fig. 3–9). Such evidence of the biomass burning effect in this region can be found by the fire maps combined with the air mass back trajectory model (Fig. 3–9). The higher occurrences of fire spots correspond to the active agricultural burning practices in this region (Fig. 3–9). According to Fig. 3–9, the burning practices mostly occurred during spring and summer in the East Asia continents (Fig. 3–9). However, no significant influence of open burning activity was observed during winter (Fig. 3–9). These results suggest that the distinctive biomass burning was not directly linked to the seasonal variations in BrC (HULIS) and WSOC concentrations in this region.

On the other hand, non-crustal K, an indicator of biomass burning or fossil fuel combustion, did not show such seasonal variation (Gabriel et al., 2002; Baduel et al., 2010) (Fig. 3–6). The relationship between the concentrations of HULIS and non-crustal K was also insignificant ($r^2 = 0.3$;

$p < 0.05$) (Fig. 3–7). In addition, the ratio of K to V (K/V) is often used to trace V-purified fossil fuels, since V in fossil fuel is mostly removed during the refining processes (Yan et al., 2012). The possible source of non-crustal V is use of raw materials such as crude oil and coal (Tsukuda et al., 2005; Yan and Kim, 2012). However, the correlation between HULIS and non-crustal V was also insignificant in this region ($r^2 = 0.04$; $p < 0.05$) (Fig. 3–7), with K/V ratios in the range of 17–673 (average = 124 ± 154). This result is consistent with the previous study in precipitation that the use of V-purified fossil fuel was insignificant in this region (Yan et al., 2012). Also, no significant correlations were found between the HULIS versus Ca^{2+} ($r^2 = 0.1$; $p < 0.05$), NO_x ($r^2 = 0.1$; $p > 0.05$), SO_4^{2-} ($r^2 = 0.02$; $p < 0.05$), and sea-spray ($r^2 = 0.02$; $p > 0.05$) (Fig. 3–7). This indicates that the seasonal variations in BrC and HULIS concentrations were not influenced by crustal minerals, sea salts, and fossil fuels. All these tracers suggest that the summer decreases in BrC and WSOC concentrations were not associated with the changes in source inputs in this region.

The HULIS concentration showed a significant negative correlation ($r^2 = 0.5$; $p < 0.05$) with the UV radiation (Fig. 3–7). The HULIS concentration was greatly reduced during the warm seasons (Jun–Sep) when the solar UV radiation and the temperature were annual maximum (Fig. 3–6). Many previous studies have found that photochemical degradation is an important

process of the efficient removal or alteration of photo-resistivity and compositions of chromophoric dissolved organic matter (CDOM) in rainwaters and aerosols (Kieber et al., 2006; Mladenov et al., 2009; Forrister et al., 2015; Dasari et al., 2019; Healy et al., 2019). Significant seasonal changes in ratios of the BrC to WSOC concentration, although the BrC and WSOC concentrations showed similar seasonal variations, also suggest that BrC is more effectively removed by the UV radiation during the warm seasons (Fig. 3–6). These results were in good agreement with the following laboratory experiments.

In order to quantify the UV-degradable BrC, the UV radiation experiments for short-term (12 h; 48 samples) and long-term (42 days; 2 samples) were performed using the aerosol sample filters. Here, HULIS (water-soluble BrC) was measured instead of BrC to measure the WSOC concentration together with the HULIS concentration for the small portion of filter sample. After the 12 h of UV irradiation, the HULIS concentrations in the winter samples (characterized by high HULIS concentrations, $N=35$) were greatly reduced by $\sim 13\%$ (Fig. 3–10). Similar decreases were observed for the WSOC concentrations for the winter samples (Fig. 3–10). However, negligible changes ($<2\%$) were observed for the summer samples (characterized by low HULIS concentrations, $N=13$) (Fig. 3–10). These results indicate that the summer samples might consist largely of a photo-

refractory WSOC pool owing to the high UV irradiation, while the winter sample consisted largely of a photo-labile WSOC pool.

The light-absorbing property of HULIS with the UV radiation experiment also showed a similar result with that of fluorescence property of HULIS (Fig. 3–11). The absorption coefficient of the summer sample was not changed after the UV irradiation, while that of the winter sample exhibited an approximately twofold change (Fig. 3–11). The photochemical degradation of HULIS was more considerably effective at shorter wavelengths ($S_{275-295}$), while no significant change was observed at longer wavelengths ($S_{350-400}$), as expected from the previous finding that the absorption losses are higher in shorter wavelengths than the longer wavelengths (Del Vecchio and Blough, 2002). In order to look at the changes in light absorption property of HULIS, the spectral slope ratios (S_R), ratio of shorter wavelength ($S_{275-295}$) to longer wavelength ($S_{350-400}$), were compared for the summer and winter aerosol samples (Fig. 3–11). In general, the S_R value increases on irradiation (Del Vecchio and Blough, 2002; Helms et al., 2008). The S_R values of non-irradiated samples were about 1.1 for the winter sample and 1.4 for the summer sample, and the irradiated samples were 1.4 for both winter and summer samples (Fig. 3–11). The S_R values of non-irradiated and irradiated samples collected in summer showed no measureable changes during the UV irradiation

experiment (Fig. 3–11). If the fresh HULIS input is constant throughout the year, the S_R values should be constant throughout the season. However, S_R values of non-irradiated samples were 1.1 for the winter sample and 1.4 for the summer sample (Fig. 3–11), while the S_R value of the non-irradiated summer sample was similar to that of the irradiated winter sample (1.4) (Fig. 3–11). Thus, this result indicates that the lower summer BrC concentration was highly associated to the photochemical degradation rather than to the reduced source inputs.

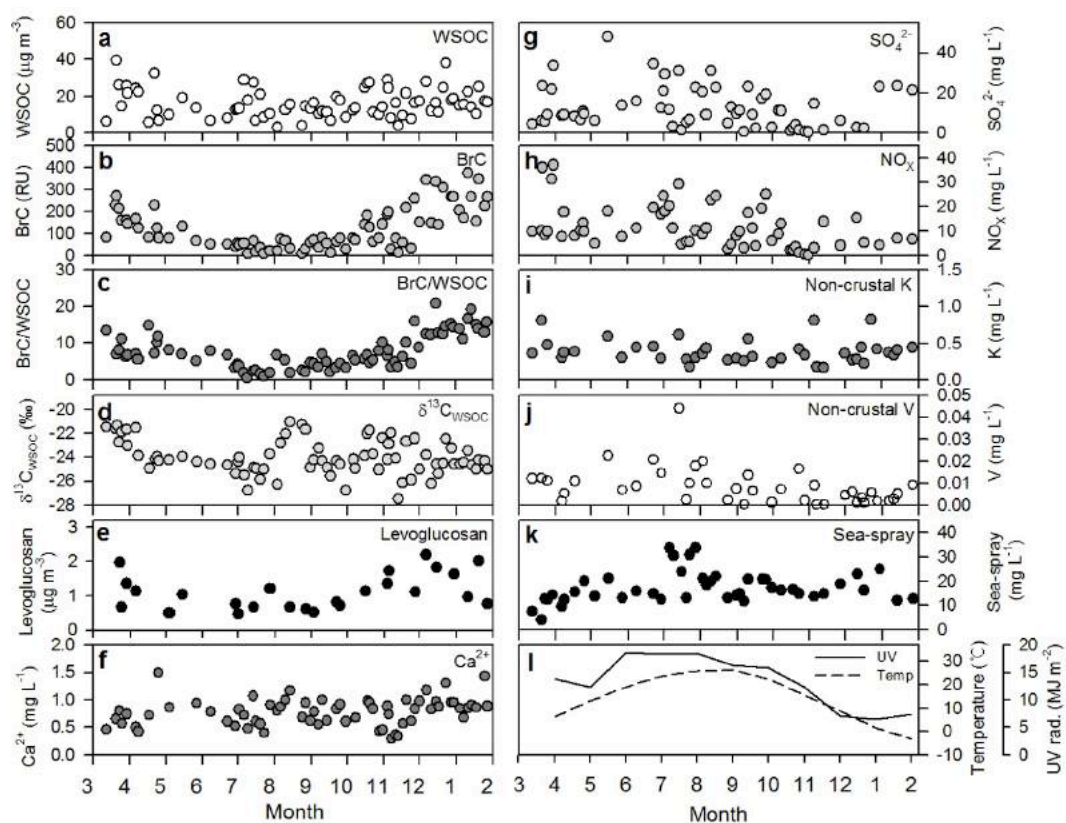


Figure 3.7 Temporal variations in (a) WSOC concentration, (b) fluorescence intensity of BrC, (c) ratio of BrC to WSOC, (d) $\delta^{13}\text{C}_{\text{WSOC}}$ values, (e) levoglucosan, (f) Ca^{2+} , (g) SO_4^{2-} , (h) NO_x , (i) non-crustal K, (j) non-crustal V, (k) sea-spray concentrations, (l) UV radiation rate, and temperature from March 2015 to January 2016 in Seoul, Korea.

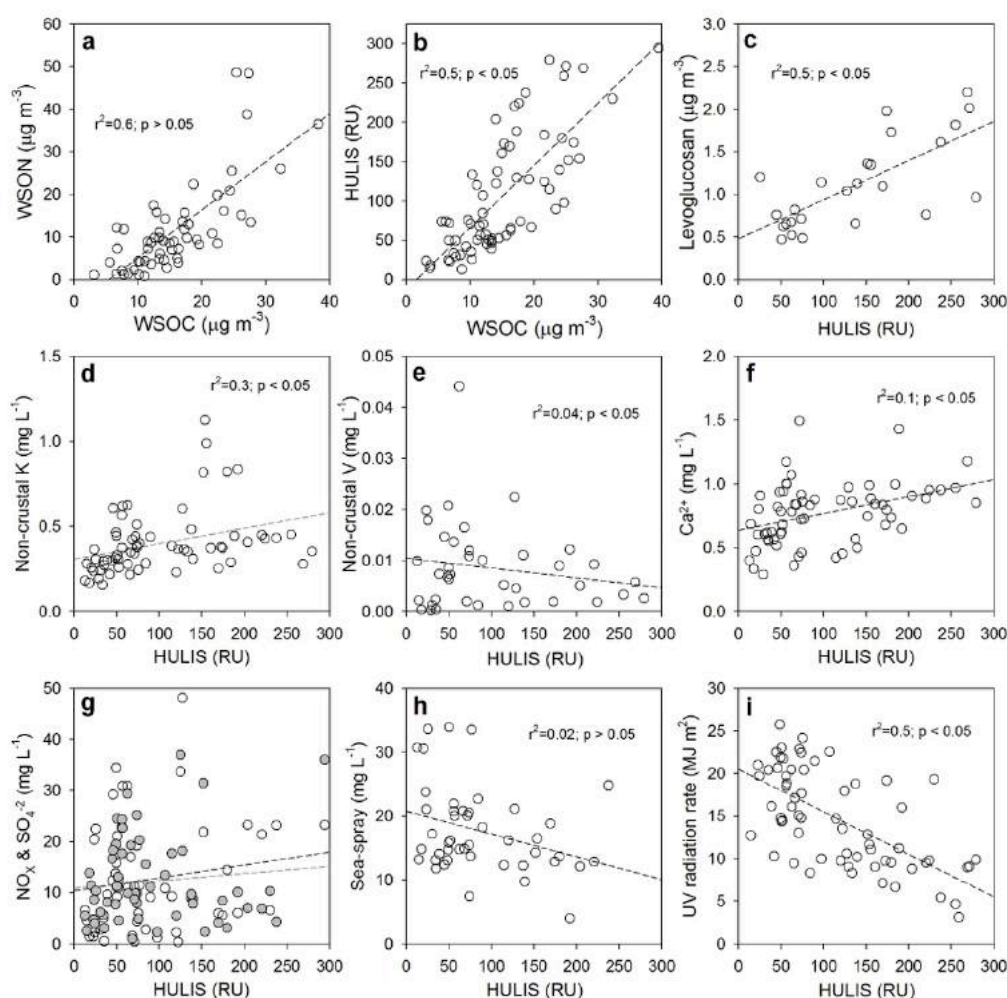


Figure 3.8 Correlations of the concentrations of (a) WSOC concentration, (b) WSOC versus HULIS, (c) HULIS versus levoglucosan, (d) HULIS versus non-crustal K, (e) HULIS versus non-crustal V, (f) HULIS versus Ca^{2+} , (g) HULIS versus NO_x (closed circle; $r^2=0.1$, $p>0.05$) and SO_4^{2-} (open circle; $r^2=0.02$, $p<0.05$), (h) HULIS versus sea-spray, (i) HULIS versus UV radiation rate. The dashed lines represent the regression line.

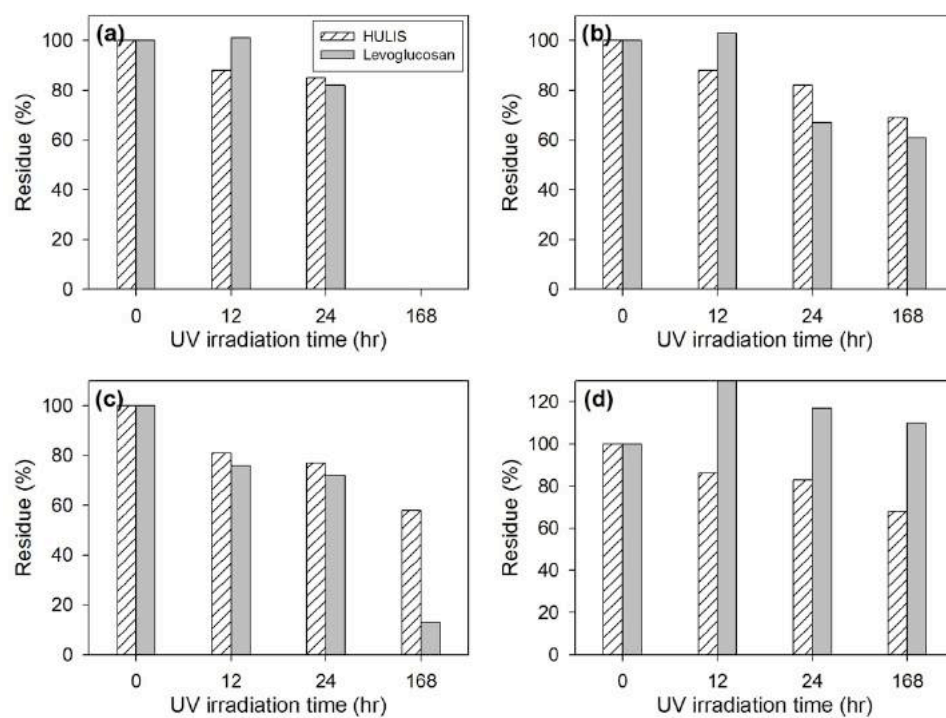


Figure 3.9 Changes of HULIS and levoglucosan concentrations for four different samples during the UV radiation (7-day) experiment.

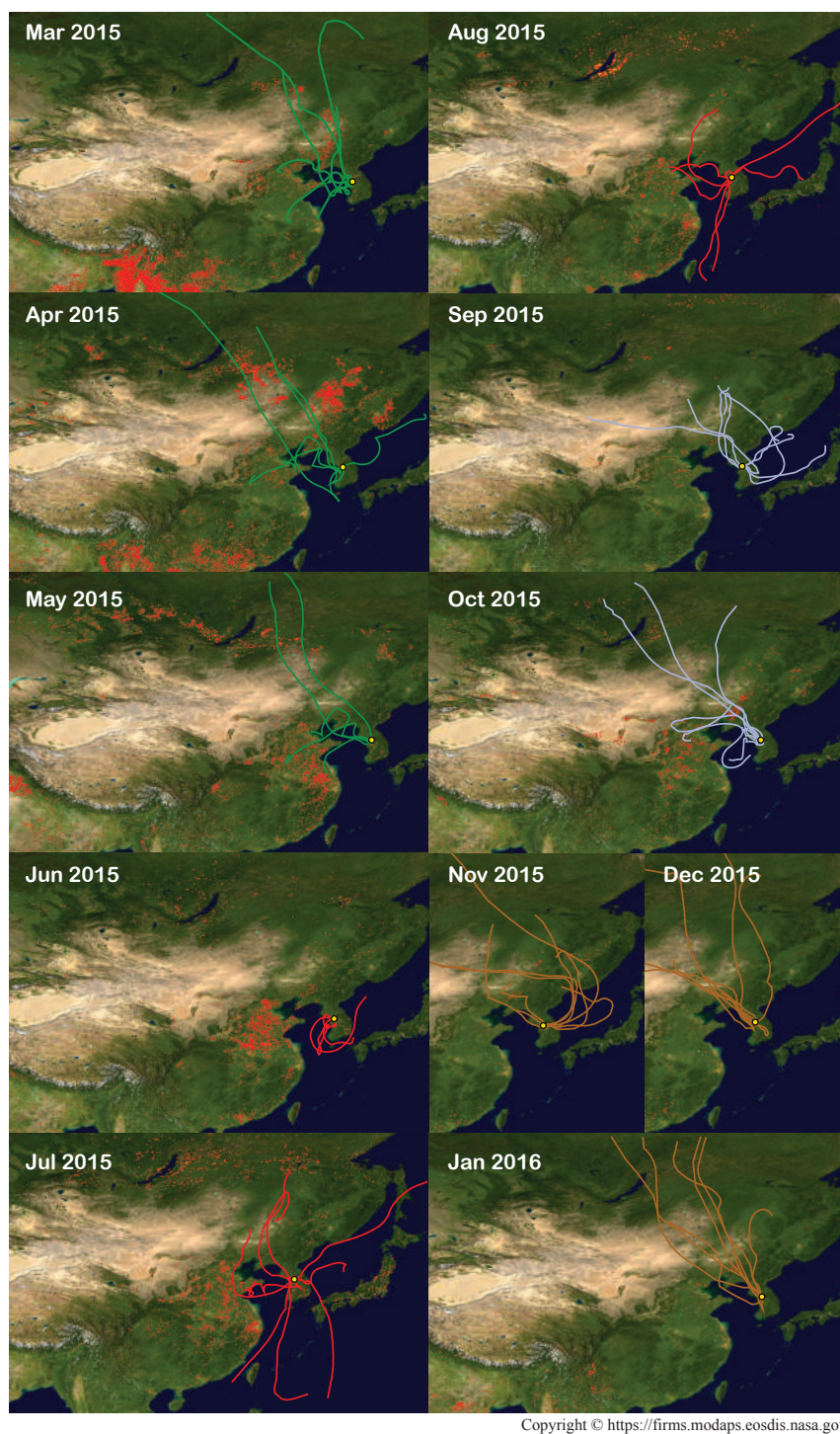


Figure 3.10 Fire maps obtained by using the MODIS fire location data provided by NASA's FIRMS combined with the air mass back trajectories around the study site from March 2015 to January 2016.

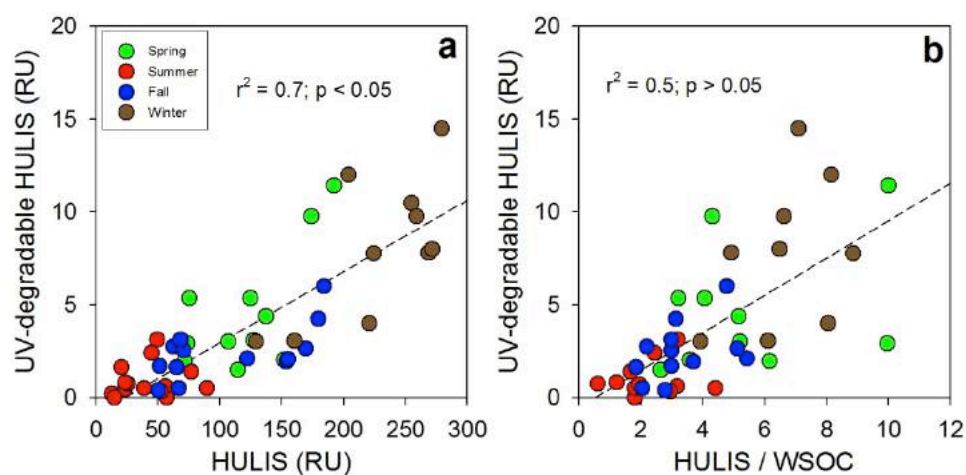


Figure 3.11 Correlations of the (a) HULIS versus UV-degradable HULIS and the (b) ratio of HULIS to WSOC versus UV-degradable HULIS in different seasons: spring (green), summer (red), fall (blue), and winter (brown). The dashed lines represent the regression lines.

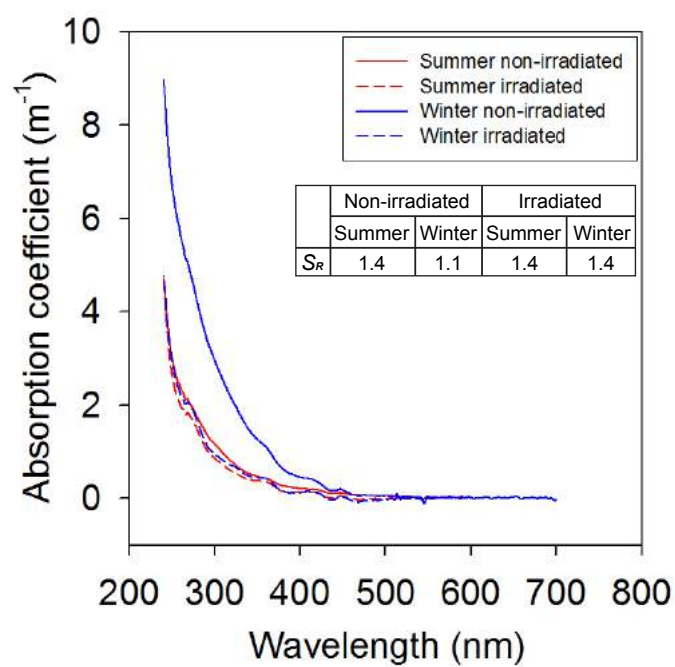


Figure 3.12 Absorption coefficients of the aerosol samples collected in winter (Dec/15) (blue) and summer (Aug/15) (red). The solid lines represent the initial values for the non-irradiated samples, and the dashed lines represent the final values for the irradiated samples.

4. Sources of DOC in coastal ocean

4.1 Study site and sampling

Sihwa Lake (126.6 °E; 37.3 °N) is located on the western coast of South Korea, with an area of 57 km² and average depth of 3.2 m (maximum depth = 18 m). This lake was originally constructed as a land reclamation project planned by the government to provide agricultural land and water for the nearby metropolitan area during the 1980s and 1990s (Bae et al., 2010) (Fig. 4–1). Freshwater runs through the six small streams into the lake and four waterways connect the lake to the Banwol industrial complex (Fig. 4–1). Since the lake experienced serious deterioration of water quality owing to the wastewater discharge from the industrial complexes under the limited water circulation, the sluice gates were constructed and opened twice a day for the water exchange between the lake and the Yellow Sea since 2012. The dyke is currently used as a tidal power plant (Lee et al., 2017) (Fig. 4–1). The total volume of the Sihwa Lake water is $\sim 3.3 \times 10^8$ m³. The discharge rate is approximately 3.4×10^8 m³ y⁻¹, enough to replace the entire reservoir in a year (Lee et al., 2003; Lee et al., 2014).

Water samples for the entire water column were collected onboard a boat (~1 ton) in two different seasons in March 2017 and September 2018. In 2018, only surface water samples were collected at shallow stations

(station number 1–6) since the water level of the reservoir was lower than in 2017, and the full depth sampling was conducted at stations 12–14. In order to check the industrial wastewater effect from the Banwol industrial complex, an additional sampling was conducted in station B4 in 2018 only (Fig. 4–1). The temperature and salinity were measured using a conductivity-temperature-depth (CTD) instrument (Ocean Seven 304, INDONAUT Srl).

4.2 Distributions of DOM in Sihwa Lake

The PARAFAC model characterized total four different fluorescent components (one marine humic-like, one protein-like, and two terrestrial humic-like components) (Fig. 4–2). The spectral characteristics of component 1 (FDOM_H; Ex/Em = 342/427 nm) and component 3 (FDOM_{H2}; Ex/Em = 381/493 nm) are associated with the terrestrial humic-like component originating from terrestrial environment (Coble 2007). Component 2 (FDOM_M; Ex/Em = 297/388 nm) is associated with the marine humic-like component originating from microbial remineralization (Coble, 2007; Jørgensen et al., 2011). Component 4 (FDOM_P; Ex/Em = 282/322 nm) is known as a protein-like (tryptophan-like) component, which originates mainly from biological production (Coble, 2007). In this study, FDOM_C was used as a representative of humic FDOM (FDOM_H) since all humic-like components showed a similar pattern.

The spectral shapes of fluorescent components were compared with other models from the OpenFluor database (<https://openfluor.lablicate.com>), which is an online database of fluorescence spectra published in earlier studies (Murphy et al., 2014). All components (C1–C4) were matched with the major components from 36, 39, 62, and 19 studies, respectively, with similarity scores of 95%.

In 2017, the vertical distribution of salinity indicated a well-mixed water column (salinity = 28–32) (Fig. 4–3). Similarly, DO and NH_4^+ concentrations were vertically uniform (Fig. 4–3). The concentrations of DO and NH_4^+ were in the ranges of 7–13 mg L^{-1} (average = $10.1 \pm 2.4 \text{ mg L}^{-1}$) and 0.1–25 μM (average = $8.7 \pm 8.1 \mu\text{M}$), respectively. However, horizontally, the DO concentration gradually increased with increasing salinity from the innermost station to the outermost station, while the NH_4^+ concentration decreased with increasing salinity (Fig. 4–3). The NH_4^+ concentration showed the lowest values ($< 1 \mu\text{M}$) between station 10 and station 13 (Fig. 4–3).

In 2017, the vertical distribution of DOC concentrations was quite different from those of salinity and DO concentrations observed in 2018 (Fig. 4–3). The DOC concentrations were in the range of 97–349 μM

(average = 184 ± 76 μM). The highest concentrations of DOC were observed in the surface waters at stations 3, 4, 5, 6, 7, 8, 9 and the bottom waters of stations 3, 4, and 5 (Fig. 4–3). The DOC- $\delta^{13}\text{C}$ values ranged from -19.2‰ to -27.8‰ (average = $-21.8 \pm 1.9\text{‰}$) (Fig. 4–3). The most depleted DOC- $\delta^{13}\text{C}$ values were found in the surface waters at stations 5, 6, 7, 9, and 10 (-22.6‰ to -27.8‰) (Fig. 4–3). The concentration of FDOM_C (terrestrial humic-like component 1), FDOM_A (terrestrial humic-like component 2), FDOM_M (marine humic-like component), and FDOM_P (protein-like component) were in the ranges of 1.6–4.1 RU (average = 2.3 ± 0.8 RU), 0.6–1.8 RU (average = 1.1 ± 0.3 RU), 1.0–2.4 RU (average = 1.5 ± 0.5 RU), and 1.6–6.1 RU (average = 2.8 ± 1.0 RU), respectively (Fig. 4–3). The concentrations of all FDOM components were generally higher in the upstream stations and decreased with salinity (Fig. 4–3). The FDOM_P concentration was slightly higher in the bottom water at station 10 (Fig. 4–3). The S_R values, a proxy for DOM molecular weight, were in the range of 0.70–1.76 (average = 1.21 ± 0.20). Higher S_R values were observed in the surface waters at stations 6, 8, 9, and 10 in 2017 (Fig. 4–3).

In 2018, salinity was in a larger range (salinity = 18–30) compared with that of 2017 (Fig. 4–4). Especially, low salinity waters (salinity = 18–27) were observed from the innermost station to station 9 (Fig. 4–4). The concentrations of DO and NH_4^+ were in the ranges of 6–11 mg L^{-1} (average

= $8.2 \pm 1.6 \text{ mg L}^{-1}$) and $0.4\text{--}25 \text{ }\mu\text{M}$ (average = $13.1 \pm 7.9 \text{ }\mu\text{M}$), respectively (Fig. 4–4). The relatively low salinity and DO concentrations were likely associated with the increased freshwater inputs (Fig. 4–4). The NH_4^+ concentrations in the outermost stations were lower than the detection limit (Fig. 4–4). While the sharp gradients of DO and NH_4^+ concentrations were observed at station 9 in 2017, the gradients occurred near station 14 in 2018, associated with the expansion of low-salinity water further to the outer stations (Fig. 4–4).

In 2018, the concentrations of DOC were in the range of $101\text{--}195 \text{ }\mu\text{M}$ (average = $130 \pm 32 \text{ }\mu\text{M}$). The DOC concentrations gradually decreased with increasing salinity (Fig. 4–4). The DOC- $\delta^{13}\text{C}$ values ranged from -19.1‰ to -21.5‰ (average = $-20.0 \pm 0.6\text{‰}$) (Fig. 4–4). The concentrations of FDOM_C , FDOM_A , FDOM_M , and FDOM_P were in the ranges of $1.4\text{--}5.1 \text{ RU}$ (average = $1.9 \pm 0.9 \text{ RU}$), $1.3\text{--}4.1 \text{ RU}$ (average = $1.8 \pm 0.7 \text{ RU}$), $1.4\text{--}4.9 \text{ RU}$ (average = $2.1 \pm 0.9 \text{ RU}$), and $1.1\text{--}2.5 \text{ RU}$ (average = $1.6 \pm 0.4 \text{ RU}$), respectively (Fig. 4–4). All humic-like FDOM concentrations were higher in 2018 than in 2017 (Fig. 4–4). The FDOM_P concentrations were generally higher in the surface water and showed a slight increase at station 12 where the salinity is slightly lower (Fig. 4–4). The S_R values were in the range of $0.72\text{--}1.08$ (average = 0.87 ± 0.10) (Fig. 4–4). The S_R values were relatively constant at all sampling stations (Fig. 4–4).

4.3 Origin of excess DOM

In both sampling periods, low-salinity waters showed higher DOC, lower DO, higher NH_4^+ , and higher FDOM_H concentrations (Figs. 4–3 and 4–4). As such, the DOC and FDOM_H concentrations exhibited significant negative correlations against salinity (Fig. 4–5), indicating low-salinity associated inputs of both DOM components. However, the patterns of DOC distributions were very different from those of FDOM_H distributions (Figs. 4–3 and 4–4), indicating decoupling of major sources for both DOM components.

In both periods, the concentrations of FDOM_H showed significant correlations against salinities and NH_4^+ (Figs. 4–5 and 4–6), with two slopes against salinity and a single slope against NH_4^+ . This correlation trend suggests that the main source of FDOM_H is dependent on the supply of NH_4^+ , rather than fresh water. In this lake, Kim and Kim (2018) hypothesized that FDOM_H is produced by anaerobic decomposition of organic matter in bottom sediments in the freshwater-seawater mixing zone, based on good correlations among salinity, NH_4^+ , and FDOM_H concentrations as well as low Eh values in higher FDOM_H concentration samples, although possible terrestrial inputs could not be excluded. Such correlations could be observed if terrestrial fresh water, which has higher FDOM_H and lower NH_4^+ , passes through the salinity mixing zone where

extremely higher amounts of NH_4^+ and lower FDOM_H are introduced from the bottom sediments. However, our $\text{DOC-}\delta^{13}\text{C}$ values ($-20.0\pm0.2\text{‰}$) in low salinity (<28) waters exclude possible significant contributions of terrestrial sources, indicating effective degradation of terrestrial sources before reached the mixing zone. Thus, the large inputs (i.e., seepage) of FDOM_H , together with NH_4^+ could happen from marine sediments, without significant decreases in DO, as the shore water runs a wide range of tidal flat sediments over a tidal cycle. In this case, depending on salinity ranges of overlying water column, different slopes of FDOM_H against salinities could be observed for different seasons as shown in this study. In addition, anthropogenic source was also insignificant since there was no anomalous increases in DOC and FDOM_H concentrations in 2018 at station B4 where the waterway connects to the Banwol industrial complex (Fig. 4–4).

In 2018, the distribution pattern of DOC concentrations was similar to that of FDOM_H (Fig. 4–4). In this period, fresh water contribution was relatively larger compared to 2017, with the lowest salinity of 18. However, the $\text{DOC-}\delta^{13}\text{C}$ values in all samples in this period ranged from -19.1‰ to -21.5‰ (average = $-20.0\pm0.6\text{‰}$), falling within the range of marine phytoplankton values (-18‰ to -22‰) (Fig. 4–5c). The S_R values were relatively low and constant (average = 0.86 ± 0.1) at all stations in 2018, indicating no significant changes in input sources or effects of

photodegradation (Fig. 4–5d). Thus, we conclude that the main source of DOC in 2018 was mainly from marine sediments, together with FDOM_H and NH_4 , as external terrestrial source of DOC was insignificant or effectively degraded on the tidal flat.

In 2017, the sources of DOC were more complicated, showing significantly higher DOC concentrations and the excess DOC independent of salinity (Fig. 4–3). Here, the excess denotes the concentrations higher than the incoming seawater from the Yellow Sea (highest salinity and lowest DOC concentration) observed in 2018 (Fig. 4–5a). The excess DOC samples observed in 2017 were ~69% higher than the DOC values of incoming seawater ($\sim 110 \mu\text{mol L}^{-1}$) (Fig. 4–5a). Thus, the higher DOC samples observed in 2017 were separated into two major groups (Group 1 and Group 2) based on their DOC concentrations, $\text{DOC-}\delta^{13}\text{C}$ values, and salinities (Fig. 4–3). Group 1 ($n=3$) includes excess DOC samples observed in stations 12 and 13 (Fig. 4–3). Group 2 ($n=11$) includes excess DOC samples observed in the surface waters of stations 4, 5, 6, 7, 8, 9, and 10, and the bottom waters of stations 3, 4, 5, and 6 (Fig. 4–3).

For Group 1 samples, the DOC concentrations ranged from 144 to $223 \mu\text{mol L}^{-1}$ (average = $175 \pm 42 \mu\text{mol L}^{-1}$) (Fig. 4–3 and 4–5c). The $\text{DOC-}\delta^{13}\text{C}$ values ranged from -19.1‰ to -22.1‰ (average = $-20.6 \pm 1.5\text{‰}$),

which are close to the $\delta^{13}\text{C}$ values of marine organisms (-18‰ to -22‰) (Gearing, 1988) (Fig. 4–3 and 4–5c). The S_R values (average = 1.07 ± 0.03) in this group showed relatively lower and constant values than that of Group 2 (Fig. 4–3 and 4–5d). The higher DOC concentrations observed in this group seem to be from in-situ biological production. Although high DOC was observed in the bottom waters near the sediments, the FDOM_H concentrations showed no concurrent increases, indicating benthic inputs was negligible in this region. Thus, the main source of DOC in Group 1 seems to be from in-situ biological production.

For Group 2 samples, the DOC concentrations ranged from 103 to $330 \mu\text{mol L}^{-1}$ (average = $213 \pm 69 \mu\text{mol L}^{-1}$) (Fig. 4–3 and 4–5a). The DOC- $\delta^{13}\text{C}$ values ranged from -21.5‰ to -27.8‰ , which include the signature of terrestrial C_3 plants (-23‰ to -32‰) (Gearing, 1988) (Fig. 4–3 and 4–5c). For this group, FDOM_H concentrations showed no significant increases relative to NH_4^+ or salinity, indicating this excess DOC concentration was not associated with the common FDOM_H sources observed in both sampling periods (Fig. 4–3, 4–4, 4–5a). However, S_R values (average = 1.26 ± 0.2) were higher than the other stations likely due to the influence of low-molecular weight DOM (Helms et al., 2008) (Fig. 4–5d). Thus, our results suggest that the excess DOC occurring in high-salinity waters in Group 2, which are characterized with non-fluorescent terrestrial sources, were

introduced by direct land-seawater interaction through the tidal inundation of seawater on the reclaimed land as this study site is constructed on the reclaimed land (Lee et al., 2020). This may happen if terrestrial DOM (based on $\text{DOC-}\delta^{13}\text{C}$ values) went through intense light exposure (producing non-fluorescent DOM) and/or bacterial degradation on land.

If only salinity and FDOM_H were used to trace the source of the excess DOC occurring in Group 2, in-situ biological production of DOC can be simply regarded as a main source since there were no significant changes in these parameters. As such, terrestrial source could be regarded as a main source of the excess DOC occurring in low-salinity waters since there were good correlations between salinities and DOC or FDOM_H . Therefore, our study suggests that the combination of stable carbon isotope, FDOM_H , and S_R values provides a critical tool to decipher the sources and characteristics of DOM in coastal waters where various DOM sources are present.

The different sources and distributions of DOM were determined in different seasons using various tracers in the Sihwa Lake, South Korea. Our results revealed that the high DOC concentrations occurring in low-salinity water, which are previously believed to be from terrestrial sources, went from marine sediment sources based on $\text{DOC-}\delta^{13}\text{C}$ values (-21.5‰ to -19.1‰) together with significant correlations among DOC, FDOM_H , and

NH_4^+ concentrations. The high DOC concentrations occurring in high-salinity waters, which are generally believed to be from marine sources, were found to be from non-fluorescent, low-molecular-weight, terrestrial DOM sources from the reclaimed land area based on depleted $\text{DOC-}\delta^{13}\text{C}$ values (-21.5‰ to -27.8‰) and higher S_R values (1.26 ± 0.2), without concurrent increases in FDOM_H and NH_4^+ concentrations. Our results demonstrate possibility that the combination of these multiple DOM tracers can be used successfully in other coastal waters where the sources and characteristics of DOM are complicated.

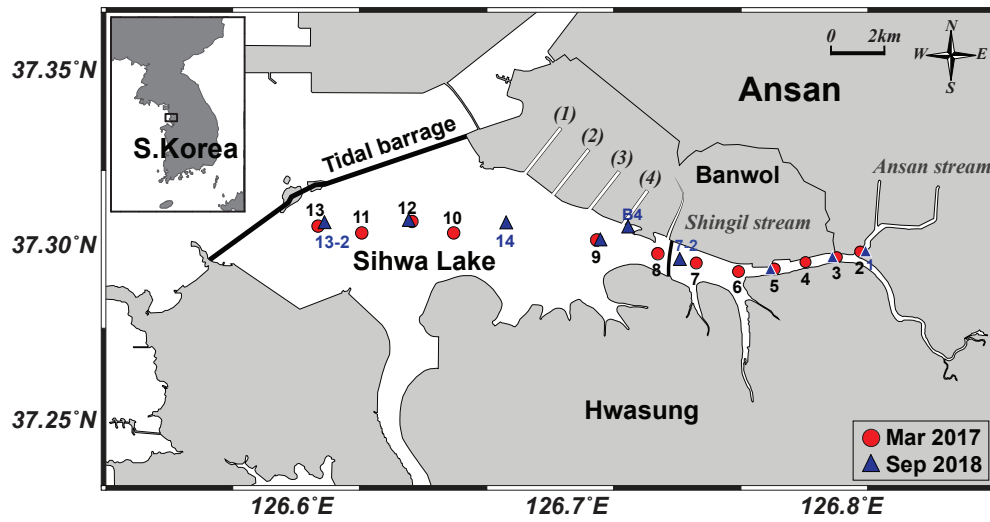


Figure 4.1 Geographical map of sampling stations in Sihwa Lake, South Korea.

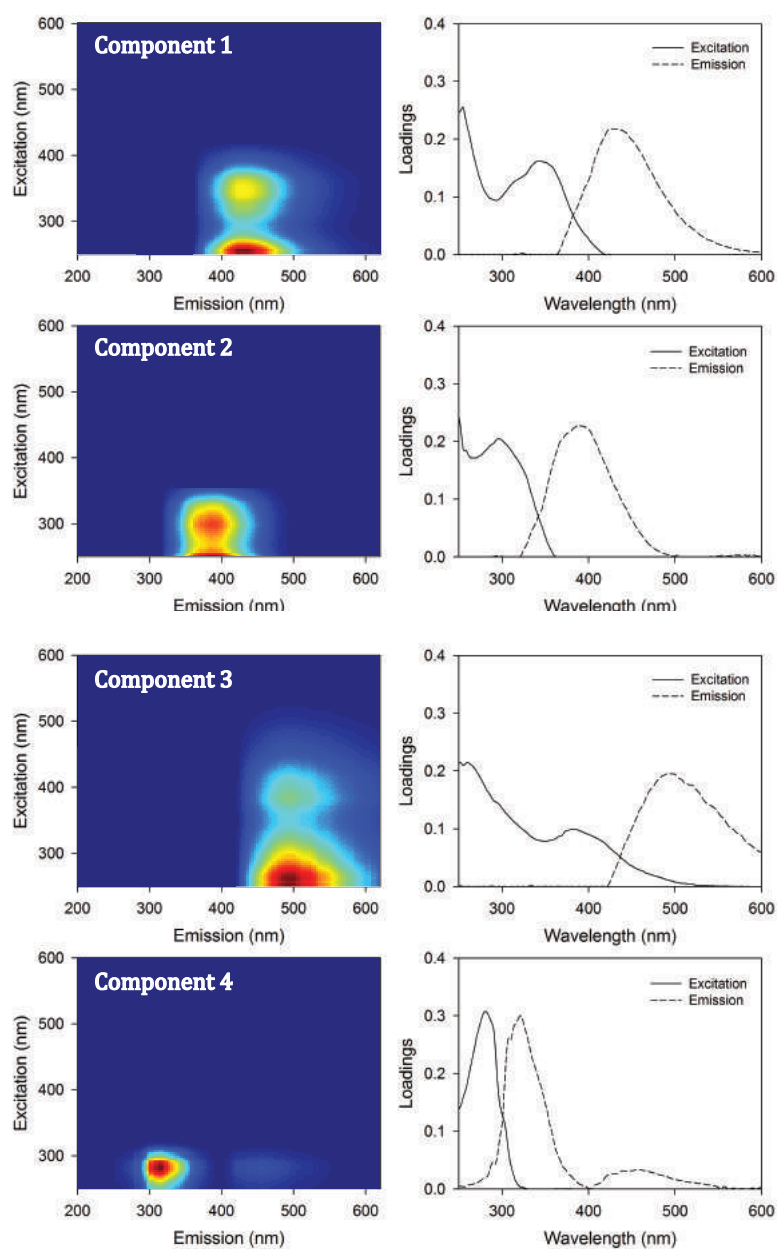


Figure 4.2 Fluorescence EEM spectra and excitation-emission loadings of terrestrial humic-like (C1 and C3), marine humic-like (C2), and protein-like (tryptophan; C3) components identified from the PAFARAC model in Sihwa Lake.

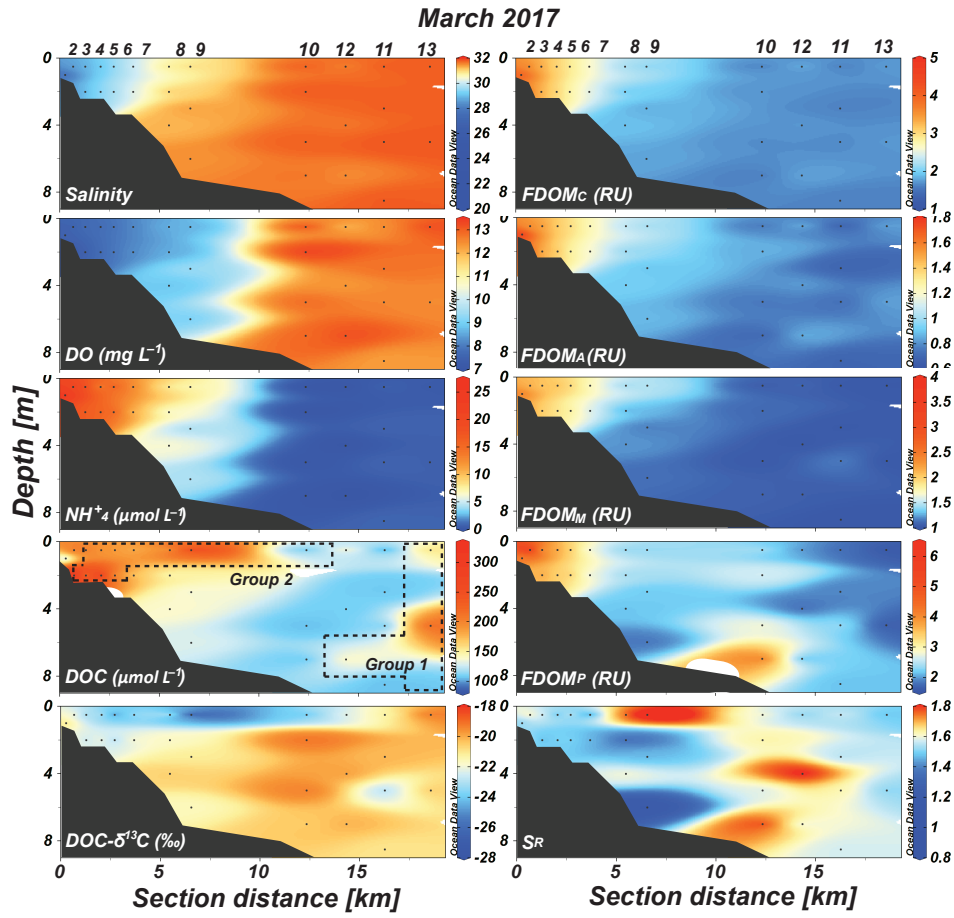


Figure 4.3 Vertical distributions of salinity, DO, NH₄⁺, DOC concentrations, DOC-δ¹³C values, FDOM_C, FDOM_A, FDOM_M, FDOM_P, and S_R values in Sihwa Lake in March 2017. The dashed blocks represent stations belonging to Group 1 and 2.

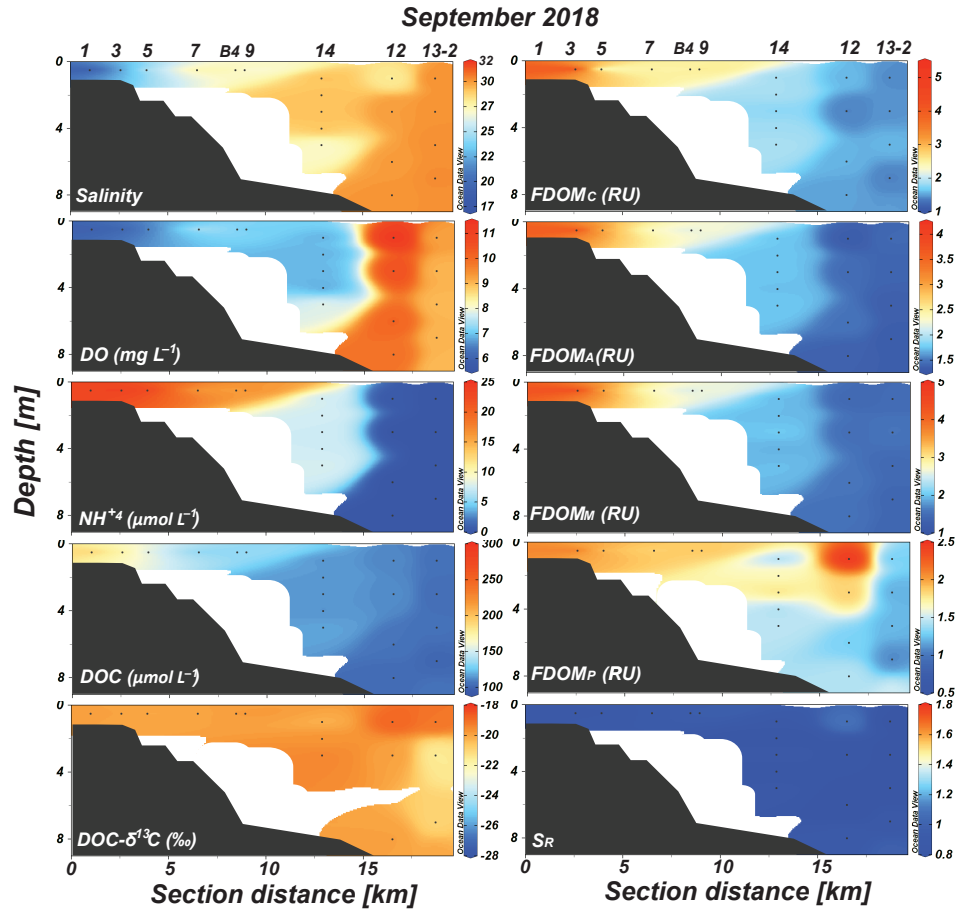


Figure 4.4 Vertical distributions of salinity, DO, NH_4^+ , DOC concentrations, $\text{DOC-}\delta^{13}\text{C}$ values, FDOM_C , FDOM_A , FDOM_M , FDOM_P , and S_R values in Sihwa Lake in September 2018.

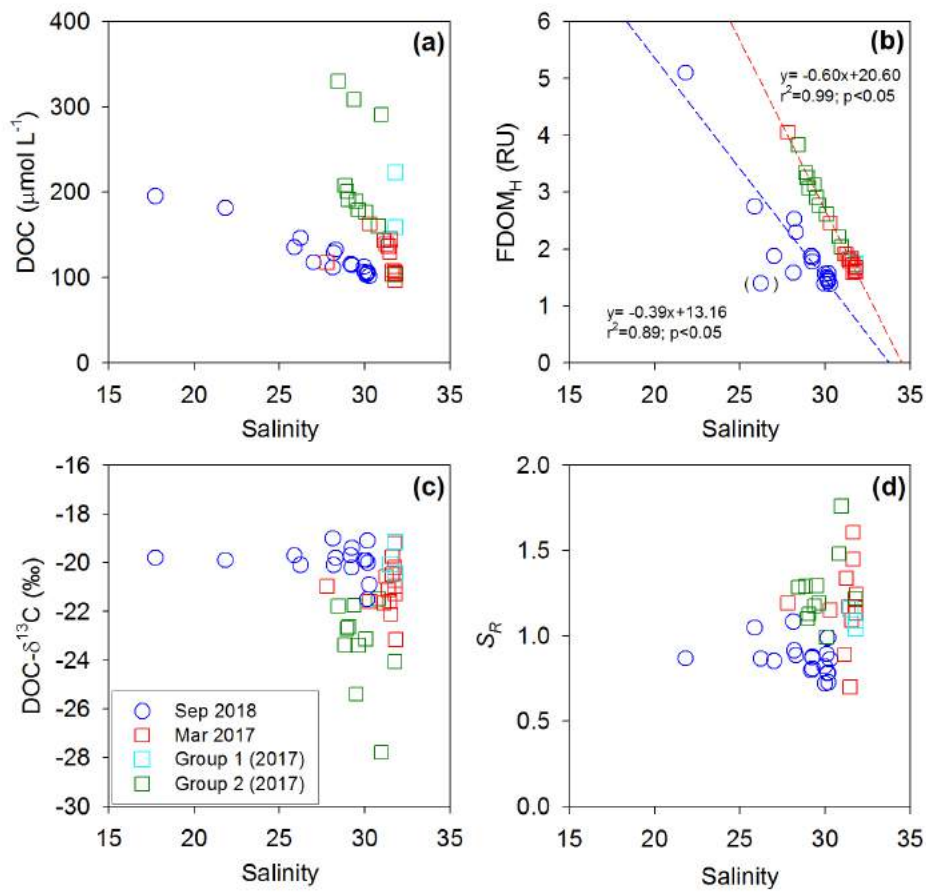


Figure 4.5 Correlations of the salinity versus (a) DOC concentrations, (b) FDOM_H concentrations, (c) DOC- $\delta^{13}\text{C}$ values, and (d) S_R values in Sihwa Lake in March 2017 (red square) and September 2018 (blue circle). The dashed lines represent the regression lines.

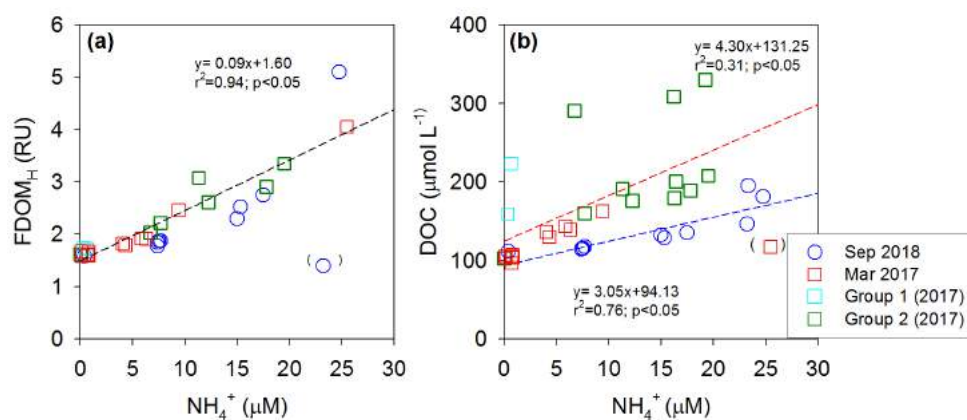


Figure 4.6 Correlations of the NH_4^+ concentrations versus (a) DOC concentrations and (b) FDOM_H concentrations in Sihwa Lake in March 2017 (red square) and September 2018 (blue circle). The dashed lines represent the regression lines.

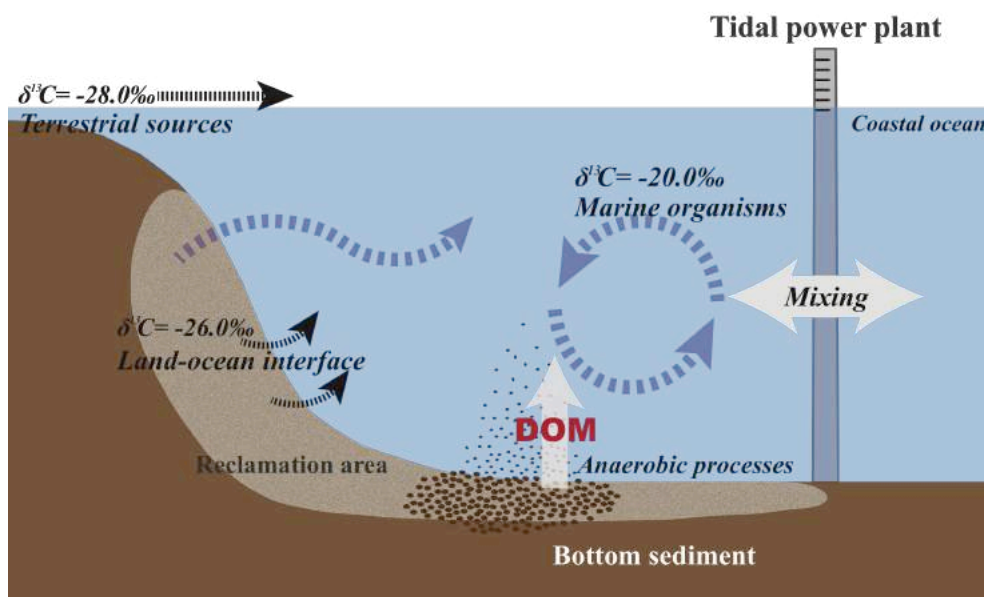


Figure 4.7 Schematic diagram of DOC cycling in Sihwa Lake.

5. Sources and fluxes of DOC in the continental shelf

5.1 Study site and sampling

This study is held in the East China Sea (area = 1×10^6 km²) located in the northwestern Pacific continental shelf. In this region, the Yellow Sea water (YSW), the Kuroshio Current water (KCW), and the Changjiang diluted water (CDW) are present with different seasonal contributions (Kim et al., 2018; Wang et al., 2000) (Fig. 5–1). In general, the YSW is originates from KCW and CDW, but its biogeochemical characteristics are significantly altered during its residence time (~5 years) in the Yellow Sea (Nozaki et al., 1991; Kim et al., 2005). In this region, the Changjiang River plays a dominant role in supplying about 80% of freshwater and delivering terrestrial organic matter to the YSW and ECS (Ichikawa and Beardsley, 2002; Wang et al., 2012; Bauer et al., 2013). In summer, the Changjiang River flows northward upon entering the Yellow Sea and then turns clockwise by the current system, while in winter the river flows southeastward along the Chinese coast (Ichikawa and Beardsley, 2002; Chen, 2009; Lie and Cho, 2016) (Fig. 5–1). Thus, sampling campaign was designed to include the influence of CDW in summer and to exclude the influence of CDW in winter and spring (Ichikawa and Beardsley, 2002; Chen, 2009; Kim et al., 2018; Lie and Cho, 2016).

In this region, five major water masses were distinguished based on the

temperature versus salinity (T-S) distributions: CDW, Kuroshio surface water (KSW), Kuroshio tropical water (KTW), Yellow Sea bottom water (YSBW), and YSW (Hur et al., 1999; Chen, 2009; Kim et al., 2018) (Fig. 5–2). In addition, the KTW flows underneath the KSW, which are differentiated based on their differences in temperature and salinity (Chen, 2009). In this study, the KCW includes both KSW and KTW. In summer, the water masses mainly consisted of CDW and KCW, while in winter and spring, salinity varied depending on the different contributions of the YSW, YSBW, and KTW (Fig. 5–2). The CDW characterized with high temperature and low salinity water was mainly observed in the central part of the Yellow Sea (Fig. 5–3). However, the CDW was observed only in summer 2012 (Fig. 5–2 and 5–3).

Water sampling was conducted four times from August to September 2012 for the summer sampling on R/Vs Tamgu 3 and Tamgu 8 of the National Fisheries Research and Development Institute (NRFDI) of Korea and on Badaro of a Korea Coast Guard vessel. Further sampling was conducted in February 2017 for the winter sampling and April 2018 for the spring sampling on R/V Onnuri of the Korea Institute of Ocean Science and Technology (KIOST). Samples were collected using 10 L Niskin bottles connected on a rosette system equipped with a conductivity temperature and depth (CTD) probe. In summer 2012, sampling was conducted for the

surface layers only at most stations except for four stations where the water column samples were collected. In winter 2017 and spring 2018, sampling was conducted for various depths at all stations.

5.2 Distributions of DOC and FDOM_H in the ECS

The concentrations of DOC were ranged from 63 to 134 μM (average = 94 ± 14 μM) in summer, 51 to 108 μM (average = 62 ± 10 μM) in winter, and 55 to 143 μM (average = 69 ± 11 μM) in spring. Relatively high DOC concentrations were mainly found near the CDW in summer 2012 (Fig. 5–4). Spatially, DOC concentration in the surface water showed the highest values near the central Yellow Sea region and gradually decreased toward the ECS and the southern sea of Korea in all sampling periods (Fig. 5–3). In winter and spring, the DOC concentration was generally higher in YSW than in KTW (Fig. 5–3).

The FDOM_H concentrations were ranged from 0.5 to 2.7 RU (average = 1.3 ± 0.4 RU) in summer, 0.2 to 2.3 RU (average = 0.8 ± 0.4 RU) in winter, and 0.1 to 1.2 (average = 0.5 ± 0.3 RU) in spring (Fig. 5–2 and 5–3). The FDOM_H in the surface water exhibited a similar spatial distribution with that of DOC in this region (Fig. 5–3). However, high FDOM_H values, decoupled from DOC concentration, were also observed on sampling stations in line C in winter and spring (Fig. 5–3).

The ^{228}Ra activity concentrations were ranged from 10 to 58 dpm 100 L^{-1} (average = 29 ± 10 dpm 100 L^{-1}) in summer, 7 to 58 dpm 100 L^{-1} (average = 29 ± 17 dpm 100 L^{-1}) in winter, and 4 to 58 dpm 100 L^{-1} (average = 23 ± 17 dpm 100 L^{-1}) in spring (Fig. 5–2). The ^{228}Ra activity showed the highest values in YSBW and the lowest values in KTW (Fig. 5–2). However, the ^{228}Ra activity concentrations higher than 40 dpm 100 L^{-1} were also observed in CDW in summer 2012 due to the riverine input of ^{228}Ra (Fig. 5–2).

5.3 Source of DOC in the YSW

For all sampling periods, both DOC and FDOM_H concentrations showed significant correlations with salinity, indicating predominant influence of riverine source in this region (Figs. 5–4a and 5–4b). Especially in summer, DOC and FDOM_H variations can be explained by the mixing between CDW and KSW (Fig. 5–2). However, significant deviation toward higher values over the mixing line in DOC concentrations was observed for some stations in the Yellow Sea water (Fig. 5–4a). In winter and spring, significant deviating increases over the two end-member mixing line between CDW and KTW were also observed, indicating additional DOC source in the YSW (Fig. 5–4a). These deviations in winter and spring were observed when the influence of CDW on the central Yellow Sea region was negligible based on the T-S diagram (Fig. 5–2).

In order to determine the main factor controlling the distributions of DOC and FDOM_H in winter and spring, DOC and FDOM_H concentrations were plotted against the ²²⁸Ra activity concentration, which is generally enriched in the YSW with about 5 years of residence time (Nozaki et al., 1989). DOC and FDOM_H showed good correlations with ²²⁸Ra activities, indicating that their source is associated with the water ages (~5 years) (Figs. 5–4c and 5–4d). The FDOM_H and ²²⁸Ra data in August 2012 (summer) and February 2017 (winter) were obtained from Lee et al. (2014) and Kim et al. (2018). Kim et al. (2018) showed that the FDOM_H flux was found to be produced from anaerobic production in bottom sediments accounting for about 30–40% of the riverine source in the ECS continental shelf. In the Yellow Sea, ²²⁸Ra activity concentration increases toward the central area up to 73 dpm 100 L⁻¹, which accounts for 9–66 times that in the KCW (Nozaki et al., 1991; Kim et al., 2005; Kawakami and Kusakabe, 2008; Lee et al., 2014). Even rivers are known to be a major source of ²²⁸Ra in the oceans and there should be considerable inputs of ²²⁸Ra from the Changjiang River, only a small fraction of it goes into the Yellow Sea, which is <10% of the benthic inputs (Lee et al., 2014; Kim et al., 2015b).

5.4 Water mixing ratios in the ECS continental shelf

Mixing ratio among the major water masses, CDW, KCW, and the YSW,

was estimated based on the ^{228}Ra –salinity relationship (Lee et al., 2014) (Fig. 5–5). The end-member values of ^{228}Ra and salinity were assigned as 7.6, 36.3, and 78.7 dpm 100 L⁻¹ and 34.7, 27.8, and 31.5 for KCW, CDW, and the YSW, respectively, based on this study and the previous literature data (Nozaki et al., 1991; Gu et al., 2012; Lee et al., 2014). The data observed in this study and previous literature data were bracketed by three end-member values with symbols (Fig. 5–5). In summer, the major water masses were mainly composed of CDW and KCW, while winter and spring values were clearly on the mixing line between the YSW and KCW and the influence of CDW is negligible (Fig. 5–5). Based on this diagram (Fig. 5–5), the proportion of the YSW in the mixture of the YSW and KCW, f , was calculated for the winter and spring data. When the two end-member mixing model was applied, f value would be 1 if the water is composed of the YSW only.

The relative proportions of the YSW in the mixture of the YSW and KCW, f value, showed a good correlation with DOC concentrations (Fig. 5–6a). In Figure 6a, the outlier (f , DOC: 0.71, 143 μM) is excluded and enclosed in brackets in order to avoid large uncertainties. Based on the relationship between f value and DOC concentrations, the DOC concentration extrapolated to $f=1$, the end-member value of the YSW, was estimated to be 101 ± 12 μM (the uncertainty was estimated with 95%

confidence interval of the linear regression; Fig. 5–6a). This end-member value is higher than the DOC value of KCW, which is the measured value (55 μM), by $\sim 45 \pm 12 \mu\text{M}$ (Fig. 5–6a).

The f value also exhibited good correlations with FDOM_{H} and $\text{DOC}-\Delta^{14}\text{C}$ (Figs. 5–6b and 5–6c). In contrast, $\text{DOC}-\delta^{13}\text{C}$ values remained constant (average = $-21.1 \pm 1.1\text{‰}$) regardless of the f values (Fig. 5–6d). Previous study has shown that the average $\delta^{13}\text{C}$ DOC value in the Changjiang River was reported to be $-30.3 \pm 1.2\text{‰}$ (Wang et al., 2012). Assuming conservative mixing between the marine end-member value of -20‰ (Gearing, 1988) and the Changjiang River value of -30‰ , the observed $\text{DOC}-\delta^{13}\text{C}$ values can be obtained by the inclusion of 0–20% of riverine DOC. However, the observed $\delta^{13}\text{C}$ DOC values between -18.8‰ and -22.8‰ (average = $-21.1 \pm 1.1\text{‰}$; Fig. 5–6d), with no correlation with f values indicating that there is only small contribution of riverine DOC to the YSW DOC pool at most. However, the average $\delta^{13}\text{C}$ value in the surface sediments of the central Yellow Sea is reported to be $-22.2 \pm 0.3\text{‰}$ (Bao et al., 2016). Therefore, DOC from surface sediments can be the potential source of the additional DOC produced in this region. According to Kim et al. (2018), FDOM_{H} is produced mainly from marine sediment and enriched over the water residence time in the ECS continental shelf and thus the positive correlation observed between the f value and FDOM_{H} also supports

the notion of DOC flux from the surface sediments in the continental shelf.

Potential sources of the additional DOC produced in the YSW were further investigated by DOC- $\Delta^{14}\text{C}$ measurements. The average DOC- $\Delta^{14}\text{C}$ values were $-271 \pm 18\text{‰}$ (2500 ± 200 yr; $n=9$) along the sampling station in Line A where KCW was dominant (Fig. 5–6c). The average DOC- $\Delta^{14}\text{C}$ values were slightly higher, $-222 \pm 38\text{‰}$ (2000 ± 400 yr; $n=14$), along the sampling station in Line C where the YSW was dominant (Fig. 5–6c). These values fit within the range previously reported (-175‰ to -300‰) in the surface layer (<200 m) of the north central Pacific Ocean (Druffel and Griffin, 2015). The end-member value of DOC- $\Delta^{14}\text{C}$ in the YSW was estimated to be $-170 \pm 50\text{‰}$ by extrapolation (when $f=1$) (Fig. 5–6c). Then, the $\Delta^{14}\text{C}$ value of the additional DOC to the total DOC pool in the YSW is estimated as -49‰ based on a simple mass balance calculation. Also, previous studies have found that the $\Delta^{14}\text{C}$ values of the surface sediments were relatively high (-174‰ to -280‰) in the central Yellow Sea compared with the outer shelf of the ECS (-274‰ to -682‰) (Bao et al., 2016). Thus, the additional DOC found in the YSW could be mainly produced from the combination of recently fixed organic matter and aged organic matter in the surface sediments.

This result is consistent with previous suggestions that the benthic DOC

fluxes or cross-shelf DOC exports from the continental margins as an important source of DOC to the oceans (Bauer and Druffel, 1998; Burdige et al., 1999; Hung et al., 2003; Wang et al., 2004; Fichot et al., 2014). Although previous studies have investigated that the cross-shelf export of terrestrial DOC is significant in ocean margins (Hung et al., 2003; Wang et al., 2004; Fichot et al., 2014), those estimates are highly influenced by river discharge and riverine materials. Thus, our study seems to be the first report on the production of additional DOC in the continental shelf with minor influence of river waters using seawater data.

5.5 Estimation of the shelf-borne DOC flux

The shelf-borne DOC fluxes in the YSW to the ECS was estimated using the following equation:

$$Flux = [(DOC_{YSW} - DOC_{KCW}) \times V_{YSW}] / \tau_{YSW} \quad (5)$$

where DOC_{YSW} is the end-member values of DOC in the YSW and DOC_{KCW} is the end-member values of DOC in the KCW. The end-member value of DOC_{YSW} was obtained by extrapolation of the correlation between f values and DOC concentrations (Fig. 5–6a), while the DOC_{KCW} is the average of observed values at stations in line A, which is located on the main path of the Tsushima Warm Current, a branch of the Kuroshio Current. V_{YSW} is the total water volume of the YSW (unit: km^3) ($4 \times 10^5 km^2 \times 50 m$); τ_{YSW} is the water residence time in the Yellow Sea. Using this equation, the

annual flux of shelf-borne DOC from the Yellow Sea to the ECS was estimated to be $2.2 \pm 0.6 \text{ Tg C yr}^{-1}$, which is at least comparable to the DOC flux from the Changjiang River discharge (1.6 Tg C yr^{-1}) (Wang et al., 2012). The uncertainty includes the scattering in the relationship between f values and DOC concentrations, although there are more uncertainties occurred from the water residence time, water volume, and spatiotemporal variations, which is hard to be considered quantitatively in this simple calculation. Nevertheless, we can only recognize the importance of continental shelf sources of DOC in the ocean from this rough estimation.

The Changjiang River appears to be the main source of DOC and FDOM_H over the northwestern Pacific continental shelf in summer when the riverine discharge is dominant in this region. However, in winter and spring, there was an additional supply of DOC in the YSW. The source of the additional DOC is from the sedimentary organic matter based on the analyses of carbon isotope ratios and FDOM_H . We estimated that approximately $2.2 \pm 0.6 \text{ Tg C}$ is additionally exported from the Yellow Sea continental shelf to the ECS per year, albeit with a large uncertainty. This shelf-borne DOC flux from the YSW forms another important source of DOC in the northwestern Pacific margin. Since the area of the continental shelf in the study region is about 0.25% of the world ocean (Tsunogai et al., 1999), while the Changjiang River water discharge ($900 \text{ km}^3 \text{ yr}^{-1}$) (Yang et

al., 2015) is $\sim 2.4\%$ of the global river discharge ($37,288 \pm 662 \text{ km}^3 \text{ yr}^{-1}$) (Dai et al., 2012), if our results are scaled linearly up to the global scale, shelf-borne DOC flux may rival the terrestrial DOC inputs. This aspect needs to be further studied in other important shelves in global oceans. Furthermore, the significant impacts of shelf-borne DOC flux should be considered in the marine carbon flux and cycle.

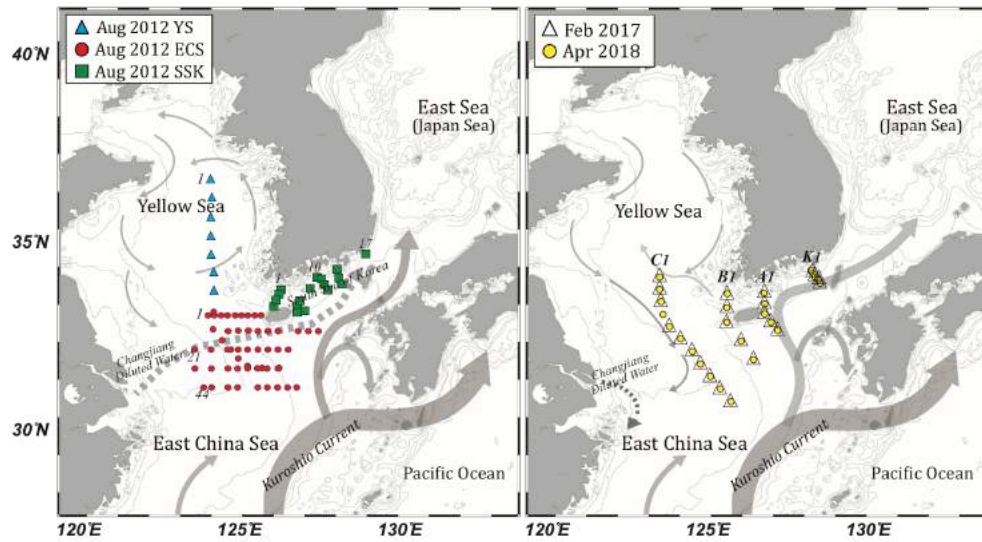


Figure 5.1 Maps of sampling stations, bottom topography, and schematic patterns of surface currents on the northwestern Pacific continental shelf during the sampling periods.

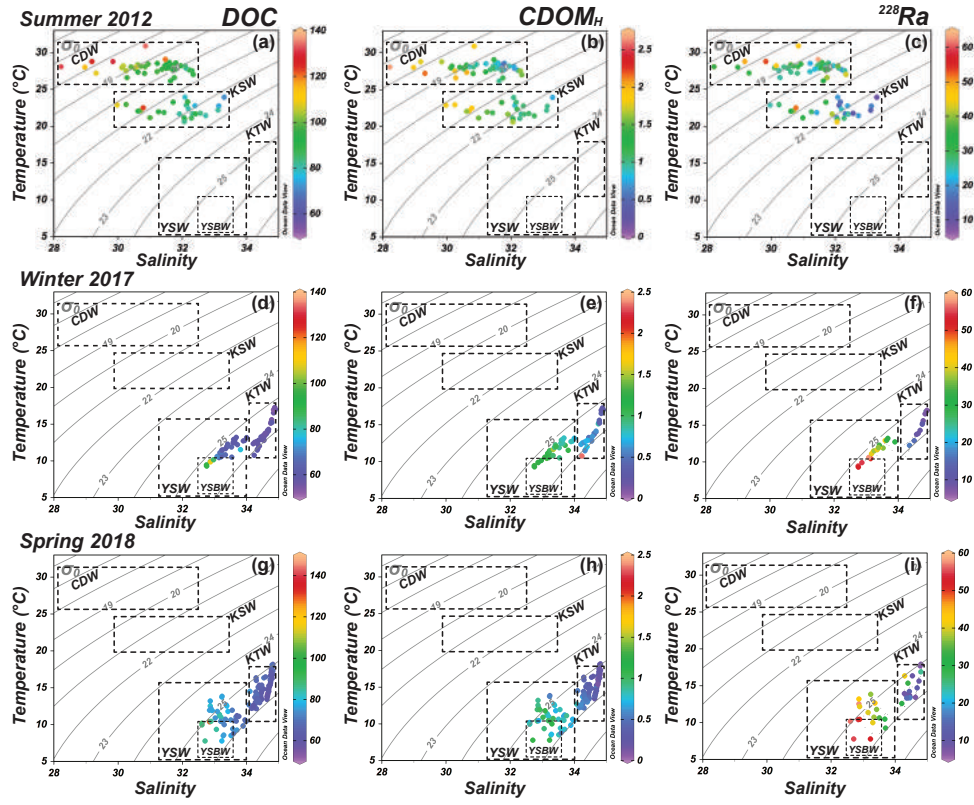


Figure 5.2 T-S diagrams for summer 2012, winter 2017, and spring 2018 (a, d, g) DOC concentrations, (b, e, h) $CDOM_H$, and (c, f, i) ^{228}Ra activities are presented in different color of the symbols.

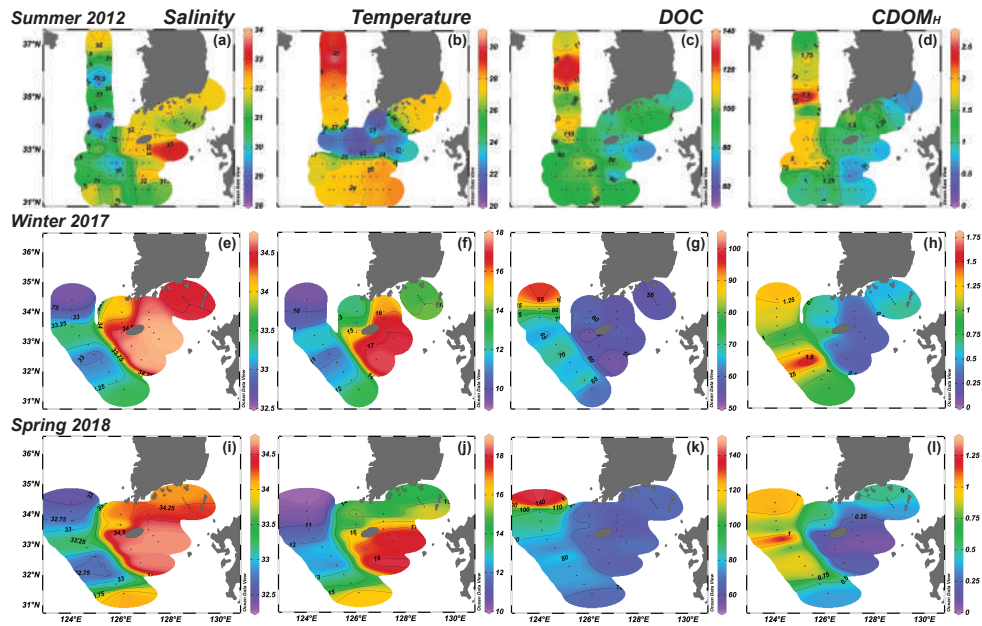


Figure 5.3 Contour figures of (a, d, g) salinity, (b, f, j) temperature, (c, g, k) DOC, (d, h, l) $CDOM_H$ in the surface water of the ECS continental shelf in summer 2012, winter 2017, and spring 2018. The contour plots were created using Ocean Data View software version 4.7.6.

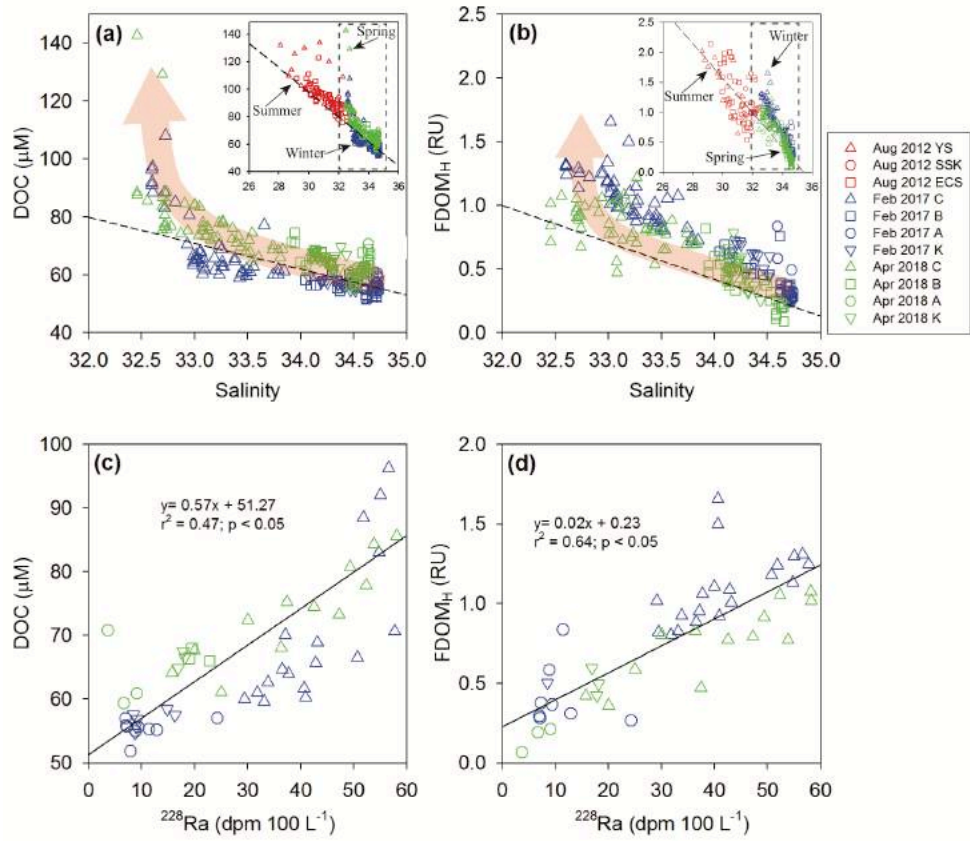


Figure 5.4 Correlations of the (a) DOC concentrations versus salinity, (b) FDOM_H versus salinity, (c) DOC concentrations versus activities of ²²⁸Ra, and (d) FDOM_H versus activities of ²²⁸Ra in the continental shelf waters during the sampling periods. FDOM_H and ²²⁸Ra data are from Kim et al. (2018) and Lee et al. (2014). Solid lines represent regression lines, while the dashed lines represent end-member mixing lines.

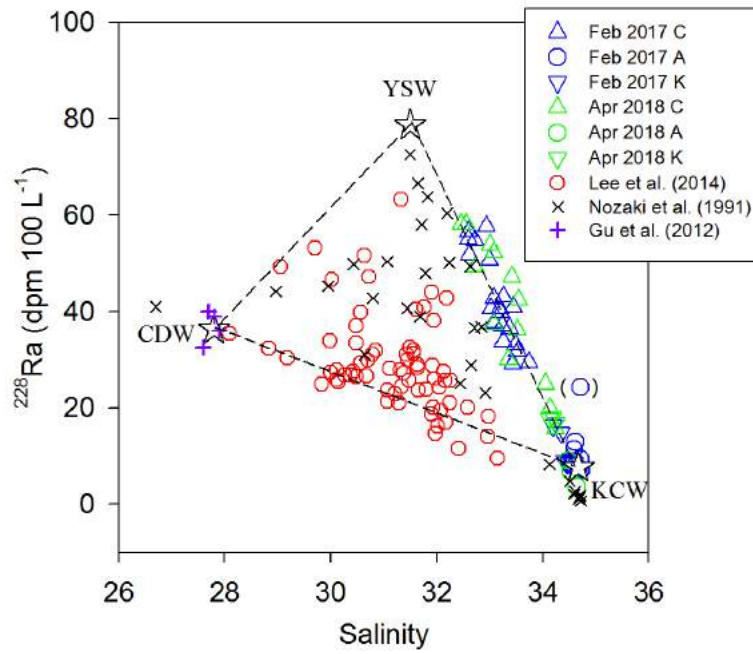


Figure 5.5 A diagram between the activities of ^{228}Ra versus salinity.

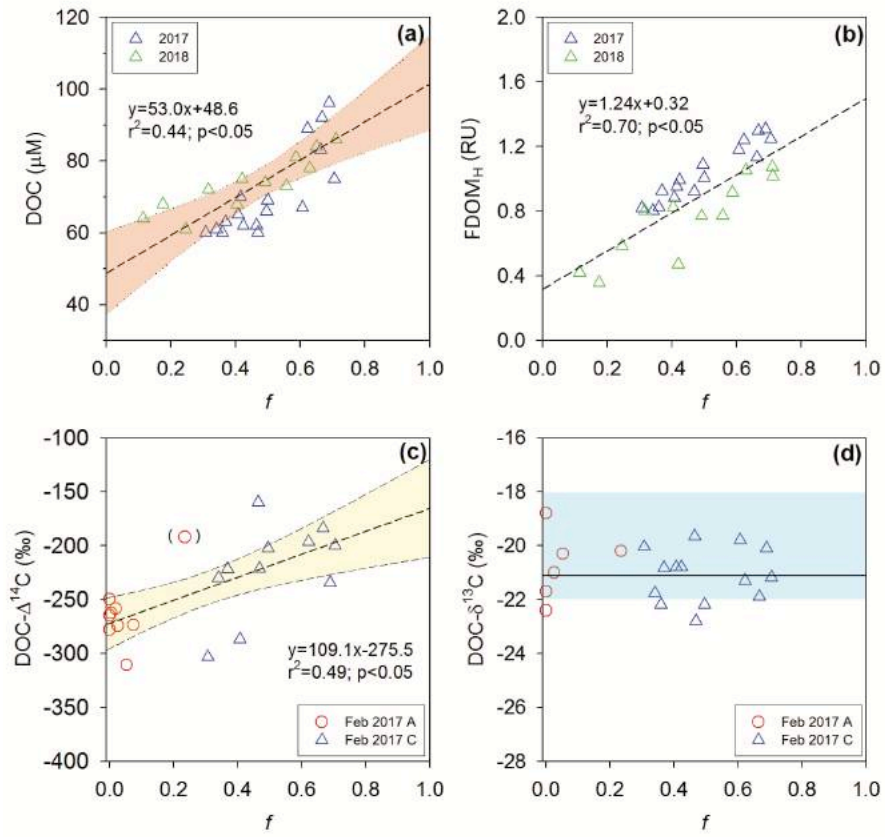


Figure 5.6 Correlations between the mixing fraction, f ($f=1$ for Yellow Sea water), against concentrations of (a) DOC, (b) FDOM_H, (c) DOC- $\Delta^{14}\text{C}$, and (d) DOC- $\delta^{13}\text{C}$ values. Dashed lines represent end-member mixing lines.

6. Distributions, sources, and sink of DOM in the marginal sea

6.1 Study site

The East Sea (Japan Sea) is a semi-enclosed marginal sea located in the northwestern Pacific Ocean, surrounded by Korean, Japanese, and Russian territories, with a maximum depth of 3,500 m and an average depth of 1,700 m (Fig. 6–1). The exchange of water within the Pacific Ocean occurs only through the shallow straits (<100 m) as Tsushima Warm Water (TWW) enters the East Sea and exit to the Pacific Ocean through Tsugaru, Soya, and Tatar Straits (Talley et al., 2003) (Fig. 6–1). Thus, the surface water includes the warm water in the south, the cold water in the north, fronts, and many mesoscale eddies (Fig. 6–2). In the East Sea, the warm eddies are frequently present near the Ulleung Island, which are elliptical with a mean diameter of about 130 km (An et al., 1994; Kim et al., 2012). These anti-cyclonic eddies are generally developed from the East Korean Warm Current originated from a northward branch of the TWW (Shin et al., 2005; Kim et al., 2012). The eddy core areas are often extended through the mixed layer and penetrate the pycnocline, enhancing the diapycnal transport in the upper layer (Zhong et al., 2017). Meanwhile, the deep water is formed by thermohaline circulation and deep convection and is constantly cold (<1°C) below 1,000 m (Kim and Kim, 1996).

In the East Sea, the Changjiang River is known to be the major source of humic-like FDOM in the surface water, and approximately 10% of the surface humic-like FDOM originates from the deep layer (Kim and Kim, 2016). In the deep ocean, humic-like FDOM is mainly produced by the degradation of sinking particles (Nelson and Siegel, 2013; Kim and Kim, 2016). The major removal mechanisms are photochemical oxidation by UV radiation and/or microbial degradation (Nelson and Siegel, 2013). In this study, we further investigated the distributions, sources, and sinks of FDOM in the East Sea, a miniature of the global ocean, to determine the major processes occurring in the major global oceans.

6.2 Distributions of DOC and FDOM in the East Sea

In the East Sea, the PARAFAC model characterized three fluorescent components: terrestrial humic-like FDOM (FDOM_H; Ex/Em = 315/478 nm; C peak), protein-like peak (tryptophan-like; FDOM_P; Ex/Em = 275/313 nm; T peak), and marine humic-like peak (FDOM_M; Ex/Em = 300/370 nm; M peak), which are consistent to previous results (Kim and Kim, 2015) (Fig. 6–3). The spectral characteristic of FDOM_H is usually derived from the terrestrial sources and autochthonous processes, while the FDOM_M is derived from the biological and microbial processes (Coble, 2007; Kim and Kim, 2015). The FDOM_P is derived from the autochthonous processes, which originates mainly from biological production (Coble, 2007; Kim and

Kim, 2015).

In the upper ocean (0–200 m), TWW brings saline (>34.3) and warmer ($>10^{\circ}\text{C}$) water into the southern part relative to the cold water mass in the northern part of the East Sea (Kim et al., 2004). During the sampling period, the southern part of the front was fully occupied by oceanic eddies, and the sampling stations in the southern part were highly affected by anti-cyclonic eddies (An et al., 1994) (Fig. 6–2). The distributions of salinity and temperature showed a mixed layer from 0 to 50 m, and the surface water penetrated deeper to 150 m in the southern part, which was associated with convergent warm eddies (Fig. 6–2, 6–4).

In the mixed layer, the concentrations of DIN and DIP ranged from 0 to 11 μM (average = 2 ± 3 μM) and 0 to 0.7 μM (average = 0.2 ± 0.2 μM), respectively, and the ratios of DIN to DIP were $\sim 12\pm7$, indicating the limitation of DIN in biological production (Kim and Kim, 2013) (Fig. 6–4). The concentrations of DSi in the mixed layer ranged from 0 to 16 μM (average = 4 ± 3 μM) (Fig. 6–4). The lower concentrations of nutrients were observed down to 150 m for some stations (M6, M7, M8, st41, st40, M12, and M17), depending on the physical mixing conditions (Fig. 6–4). The concentrations of DOC in the mixed layer ranged from 51 to 79 μM (average = 69 ± 6 μM), and they were relatively low (<60 μM) in the

northernmost stations (M16 and M17) (Fig. 6–4).

The concentrations of C peak and M peak ranged from 0.14 to 0.32 RU (average = 0.23 ± 0.04 RU) and 0.10 to 0.17 RU (average = 0.13 ± 0.02 RU), respectively, in the mixed layer. The concentrations of both peaks were relatively low, but the patterns were irregular throughout the entire 0–200 m layer (Fig. 6–4). The concentrations of T peak ranged from 0.0 to 0.12 RU (average = 0.01 ± 0.02 RU). Notably, T peak occurred only in the mixed layer of the southern part of the East Sea (Fig. 6–4).

The salinity and temperature below 200 m ranged from 33.9 to 34.2 and 0.1 to 6.8°C in the entire ocean, respectively (Fig. 6–5). Almost uniform salinity (~ 34.1) and temperature ($0.2 \pm 0.1^\circ\text{C}$) were observed below 800 m in the deep East Sea (Fig. 6–5), although the deep water mass is divided into East Sea Intermediate Water, Central Water, Deep Water, and Bottom Water by physical oceanographers (Kim and Kim, 1996; Kim et al., 2004).

The concentrations of DOC below 200 m were in the range of 46–65 μM (average = 57 ± 4 μM) (Fig. 6–5 and 6–6). The higher concentrations of DOC (70 ± 4 μM) in the surface water affected down to 1,000 m (~ 60 μM) at some stations (M4, M6, M7, M8, and M9) near the Ulleung Basin (Fig. 6–5). The vertical distribution patterns and ranges of DOC concentrations

observed in this study were consistent with those of a previous study in this sea (Kim et al., 2015) (Fig. 6–5 and 6–6). The DOC concentrations in the deep East Sea ($54 \pm 2 \mu\text{M}$, $>800 \text{ m}$) were higher than those in the deep Pacific Ocean ($34\text{--}43 \mu\text{M}$, $1000\text{--}5000 \text{ m}$) (Hansell and Carlson, 1998), but similar to those observed in the deep Arctic Ocean ($54 \pm 3 \mu\text{M}$, $\sim 4000 \text{ m}$) (Benner et al., 2005) and the deep Nordic Seas ($50 \mu\text{M}$, $\sim 3500 \text{ m}$) (Amon et al., 2003), where the deep water is formed (Kim et al., 2015).

The concentrations of C peak, M peak, and T peak below 200 m were in the range of 0.22–0.53 RU (average = $0.38 \pm 0.08 \text{ RU}$), 0.11–0.26 RU (average = $0.15 \pm 0.02 \text{ RU}$), and 0.0–0.04 RU (average = $0.0003 \pm 0.04 \text{ RU}$), respectively (Fig. 6–5 and 6–6). T peak below 400 m was lower than the detection limit (Fig. 6–6). The ratio of peak C to M (C/M ratio), indicating the extent of surface photobleaching, ranged from 1.0 to 3.4 (average = 2.2 ± 0.5) with relatively lower values in the surface layer and higher values in the deep layer (Fig. 6–6).

6.3 Sources of DOM in the East Sea

The distributions of nutrients and DOC in the upper ocean were largely dependent on hydrographic dynamics based on temperature and salinity (Fig. 6–4). The anti-cyclonic eddies seem to deepen the low-nutrient surface water down to 100 m as shown by Hyun et al. (2009) (Fig. 6–4).

This result suggests that the production and degradation had not been changed according to the eddy formation in this region, although significant changes in biogeochemical conditions were observed in many eddies in other study regions (McGillicuddy and Robinson, 1997; Kim et al., 2012; Kolansinski et al., 2012; Uchiyama et al., 2017).

The concentrations of DOC and T peak were relatively higher in the southern region, perhaps due to the higher biological production in warmer water during this season (Fig. 6–4). However, these component did not show any significant correlations against chlorophyll a or nutrient concentrations, indicating that their production and degradation are not proportional to biological production in the euphotic zone (Fig. 6–4 and 6–7). The concentrations of the labile FDOM component, T peak, were only observed in the surface mixed layer due to its rapid removal in the surface layer before reaching the deep ocean (Jørgensen et al., 2011) (Fig. 6–4 and 6–6).

In the deep ocean (>200 m), the average concentration of DOC in the northern part (57 ± 3 μM) was slightly lower than that in the southern part (59 ± 3 μM) although the hydrographic features of the deep East Sea were relatively uniform (Fig. 6–5). The average concentration of DOC in the deep sea of the northern part was similar to that reported in a previous study

($59 \pm 3 \mu\text{M}$) (Kim et al., 2015). Kim et al. (2015) suggested that DOC degradation with age results in slightly higher DOC concentrations in the northern part of the East Sea. However, the average DOC concentration in the deep sea of the southern part was slightly higher than that reported by Kim et al. (2015) ($55 \pm 2 \mu\text{M}$). In this study, such higher DOC concentrations in the southern part could occur if the high DOC surface water invades directly into the deep sea (Fig. 6–5). For example, the combination of the oceanic eddies and internal waves (Polzin et al., 1997; MacKinnon et al., 2017; Legg, 2020) developed by the complex structure of the Ulleung Basin topography could result in deep ocean mixing (Fig. 6–5). If this happened, the higher DOC concentrations in the deep sea of the southern part might include a larger proportion of semi-labile DOC during the sampling period than the northern part of the East Sea (Fig. 6–5). Moreover, relatively higher DOC concentration in the deep East Sea compared with the global ocean ($>45 \mu\text{M}$) (Hansell, 2005) could be due to the low degradation rate of DOC under the low water temperature ($<1^\circ\text{C}$) (Hansell, 2005; Kim et al., 2015).

Significant correlations between AOU and C peak ($r^2=0.85$; $p<0.05$) or M peak ($r^2=0.19$; $p<0.05$) in the East Sea indicate that the major production of both FDOM components in the interior of the East Sea (200 m–intermediate layer) is due to the microbial remineralization of sinking organic matter as previously documented (Yamashita and Tanoue, 2008;

Jørgensen et al., 2011; Tanaka et al., 2014; Catalá et al., 2015; Kim and Kim, 2015) (Fig. 6–8). In addition, excess concentrations of C peak and M peak were observed in the deep East Sea (>750 m), which is independent on AOU, as previously reported by Kim and Kim (2016). Kim and Kim (2016) suggested that approximately 8–15% of humic-like FDOM was produced by anaerobic remineralization of organic matter in the subsurface bottom sediments. Our results also showed similar (~12–13%) inputs of humic-like FDOM by the anaerobic microbial production of C peak and M peak in bottom sediments (Fig. 6–9).

In this study, C peak gradually increased with depth, while M peak remained almost constant level except for the surface layer (Fig. 6–6). As such, the C/M ratios showed the lowest value in the surface layer and gradually increased to 1,000 m (Fig. 6–6). However, our results were different from previous studies (Tanaka et al., 2014; Kim and Kim, 2015; Kim and Kim, 2016) that showed a similar trend for both C peak and M peak in the upper 1,000 m. This difference could be due to the use of different instruments, which have varying sensitivities for different wavelengths and peak locations.

This uniform distribution of M peak in the entire water column could be due to the ineffective production of M peak relative to C peak as shown

by the different slopes of both components against AOU (Fig. 6–6, 6–8). The amount of M peak increase at a given level of AOU increase was significantly lower than that for C peak (Fig. 6–8). Previous studies also showed a relatively lower production rate of M peak relative to C peak in laboratory experiments (Nelson and Gauglitz, 2016) and field observations (Tanaka et al., 2014; Catalá et al., 2015; Kim et al., 2020).

Alternatively, relatively higher concentrations of M peak found in the upper layer could be due to more rapid UV degradation of C peak relative to M peak (Fig. 6–6). In general, the changes in concentrations of C peak were known to be higher than those of M peak in the upper ocean due to more rapid UV degradation of C peak. This trend was also verified based on laboratory experiments (Cory et al., 2007; Moran et al., 2000; Helms et al., 2013) and field observations of absorption indices such as absorption coefficients and spectral slope ratios in other studies (Helms et al., 2013; Yamashita et al., 2013). Thus, the ratio of C peak to M peak (C/M ratio) is often used as an indicator of different photochemical histories of DOM in the surface layer (Helms et al., 2013; Hansen et al., 2016). This fractionation of C peak and M peak in the surface water of the East Sea could be further intensified with the contribution of the continental shelf water flowing into the East Sea, which has a long residence time in the Yellow Sea and the East China Sea (Nozaki et al., 1991; Kim et al., 2005; Kim and Kim, 2015; Kim

et al., 2018) (Fig. 6–6). The surface water with low C/M ratios could be effectively mixed downward up to 800 m as suggested by a previous study based on the rare earth element tracers (Seo and Kim, 2020) (Fig. 6–6).

Overall, the distributions of humic-like FDOM (C peak and M peak) seem to be influenced by their production (water column) and photochemical degradation (surface layer) mechanisms in the East Sea. Therefore, further studies are needed to evaluate the dominant mechanisms (production versus degradation) controlling the FDOM distributions in the East Sea.

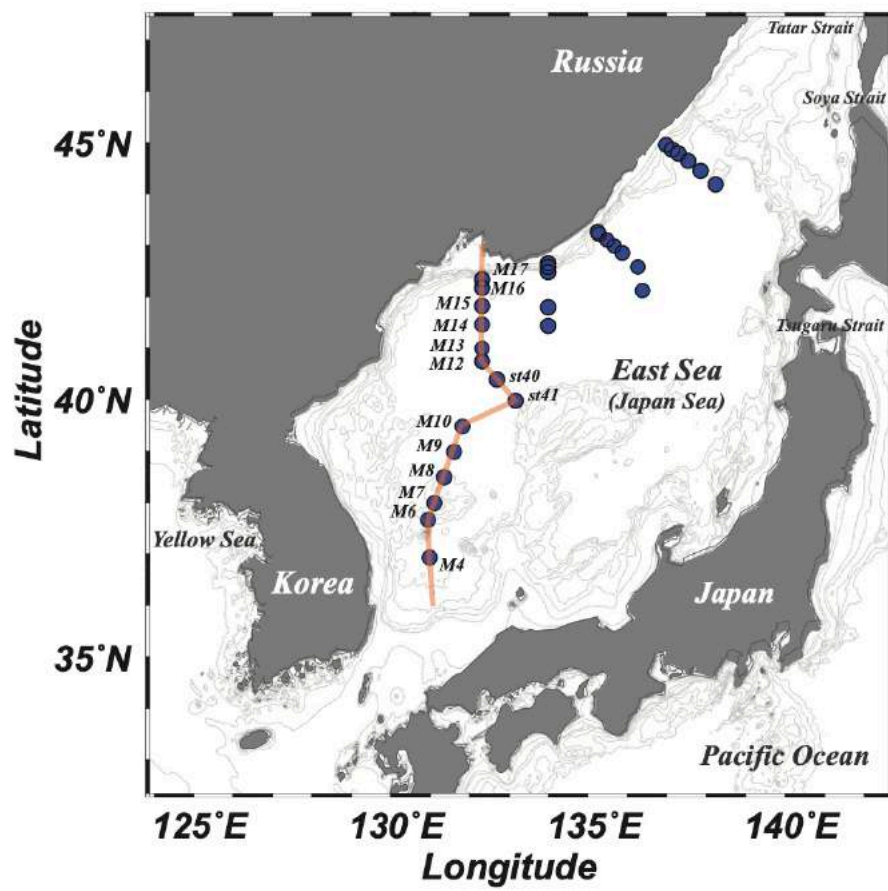


Figure 6.1 Map showing the bottom topography and sampling stations in the East Sea (Japan Sea).

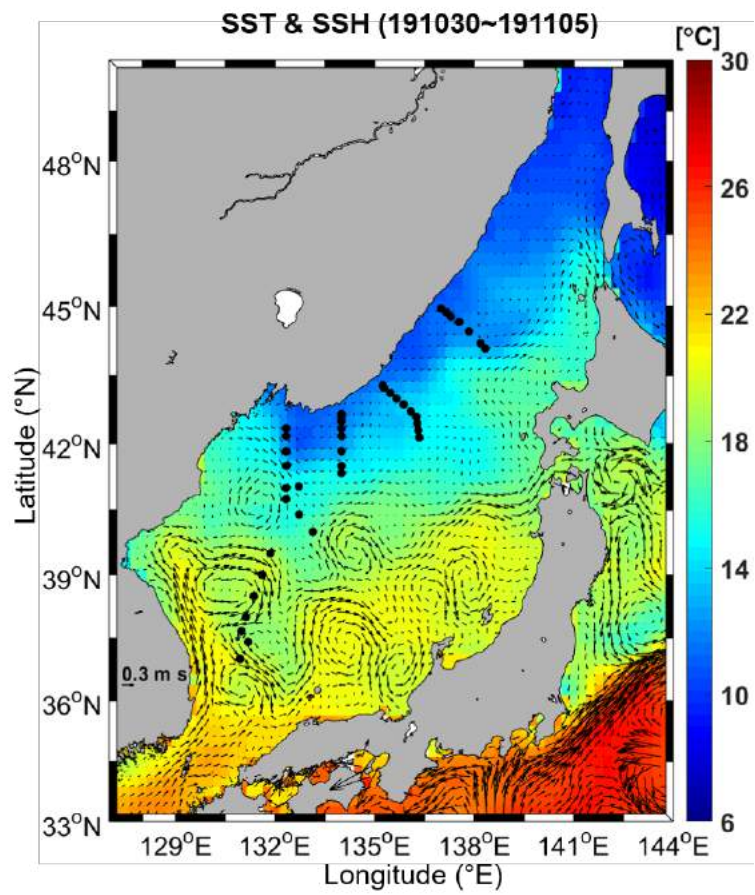


Figure 6.2 Map showing a sea surface temperature and sea surface height in the East Sea.

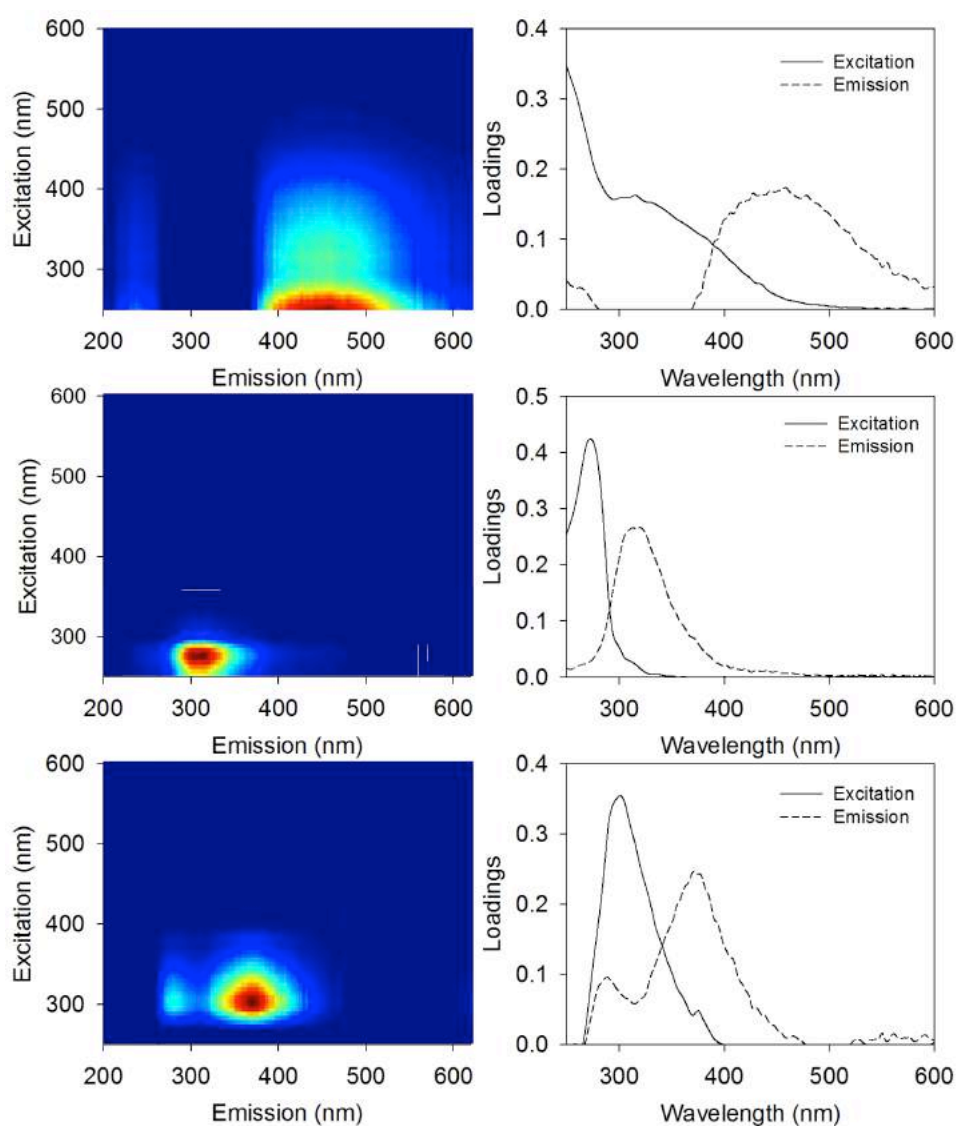


Figure 6.3 Fluorescence EEM spectra and excitation-emission loadings of terrestrial humic-like (C1), protein-like (tryptophan; C3), and marine humic-like (C2) components identified from the PAFARAC model in the East Sea.

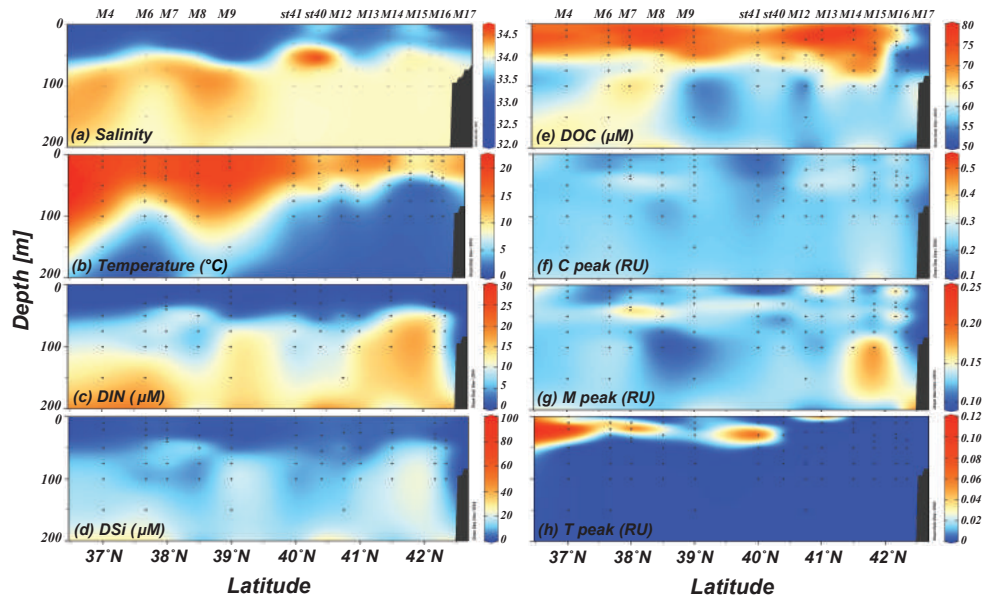


Figure 6.4 Vertical distributions of salinity, temperature, concentrations of DIN, DSi, DOC, C peak, M peak, and T peak in the upper ocean (0–200 m) in a SW–NE cross-section of the East Sea.

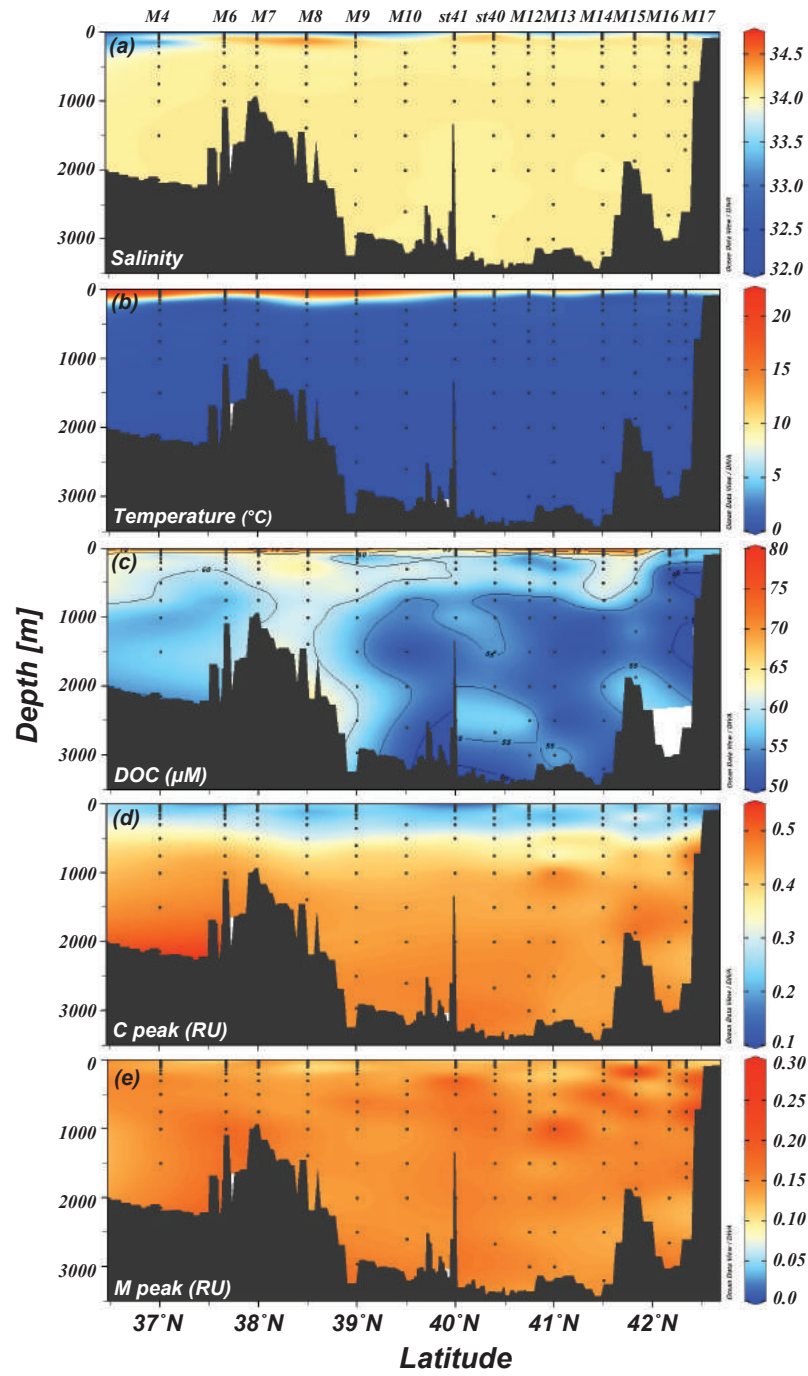


Figure 6.5 Vertical distributions of salinity, temperature, concentrations of DOC, C peak, and M peak in a SW-NE cross-section of the East Sea.

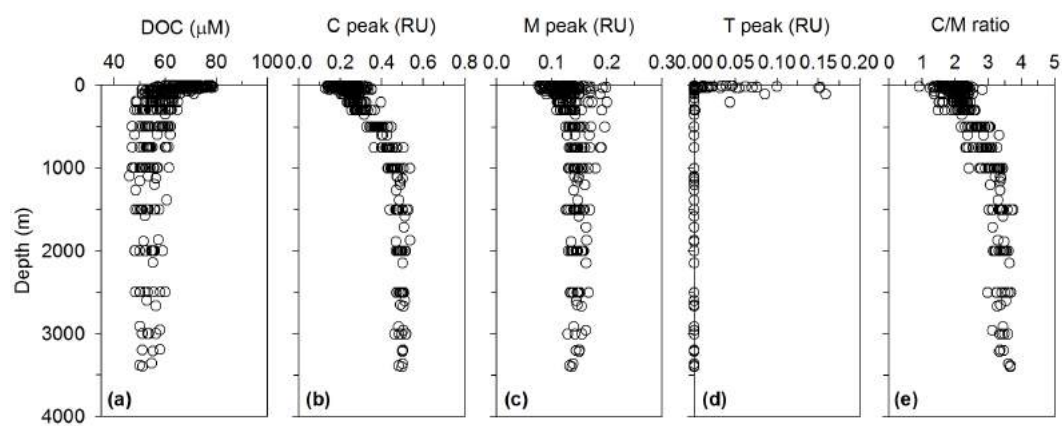


Figure 6.6 Vertical distributions of (a) DOC, (b) C peak, (c) M peak, (d) T peak, and (e) the ratio of C peak to M peak in the East Sea.

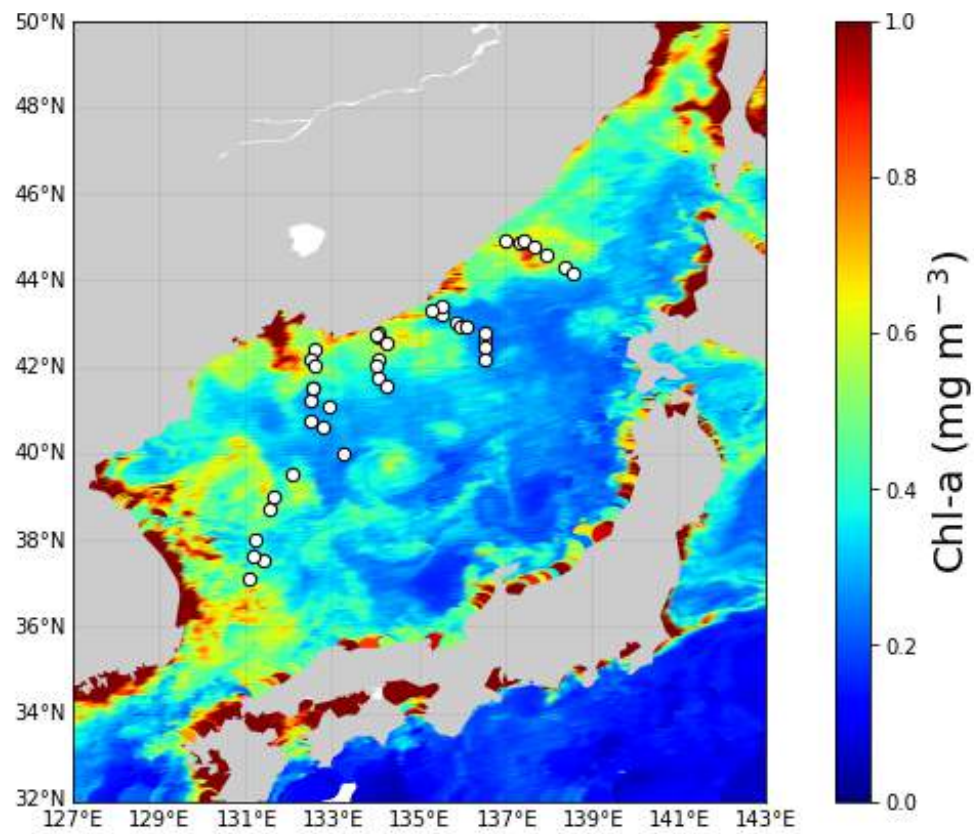


Figure 6.7 Map showing the concentration of chlorophyll-*a* in the surface layer of the East Sea.

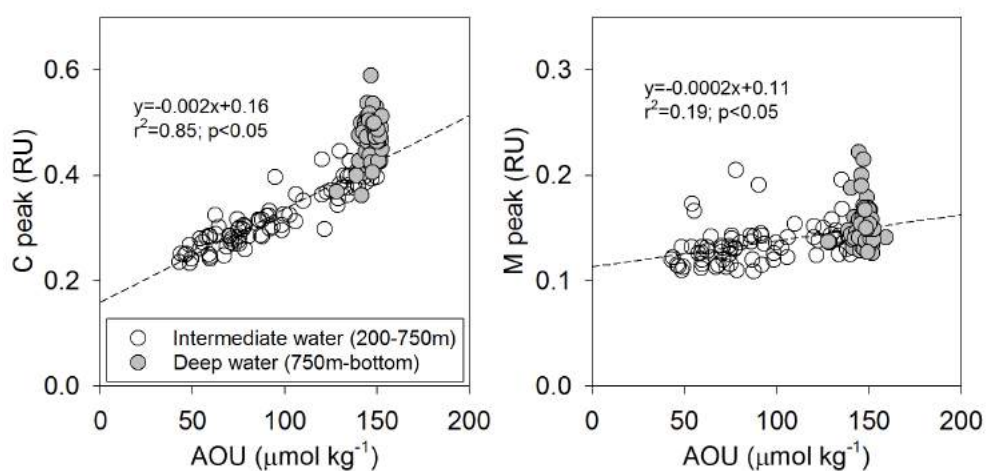


Figure 6.8 Scatterplots of AOU against the C peak and M peak in the East Sea (200 m–bottom depth). Empty circles represent the intermediate water layer (200–750 m), and filled circles represent the deep water layer (750 m–bottom depth).

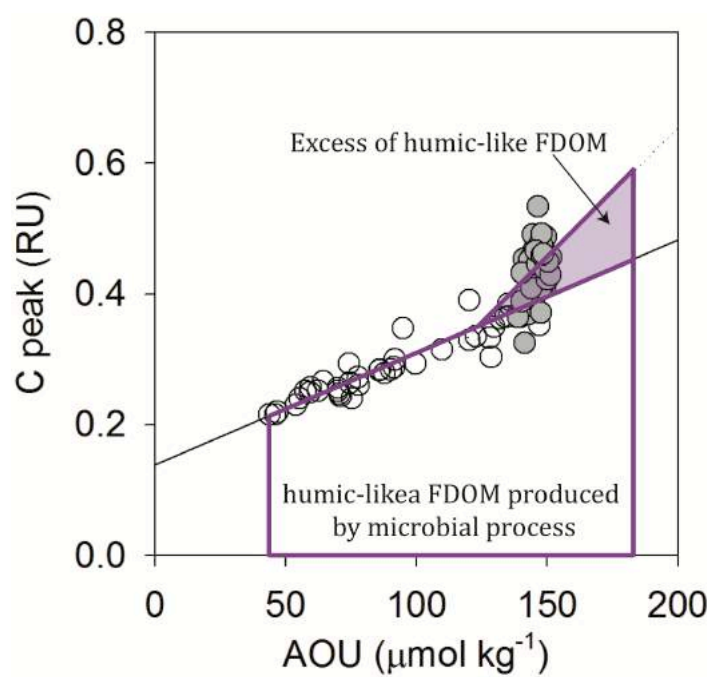


Figure 6.9 Schematic diagram illustrating the fluorescence intensity of excess C peak.

7. Summary and conclusion

The sources, sinks, processes, and biogeochemistry of DOM were determined using the multiple biogeochemical tracers including stable- and radio-carbon isotopes, optical properties of DOM (absorbance and fluorescence), radionuclide (^{228}Ra), and other chemical constituents in the urban city atmosphere and various aquatic environments: (1) an artificial lake (Sihwa Lake), (2) the East China Sea continental shelf, and (3) the marginal sea (the East Sea). This study has provided important implications for our understanding of and insight into the sources and fates of DOC/WSOC in the atmosphere and various aquatic environments. Also, this study successfully demonstrated that combining these tools could be further applied effectively in many different environments where the sources and nature of the DOM are complex.

Bibliography

- Alkhatib, M., del Giorgio, P. A., Gelinas, Y., and Lehmann, M. F. (2013). Benthic fluxes of dissolved organic nitrogen in the lower St. Lawrence estuary and implications for selective organic matter degradation. *Biogeosciences*, 10, 7609–7622, <https://doi.org/10.5194/bg-10-7609-2013>.
- Alperin, M. J., Martens, C. S., Albert, D. B., Suayah, I. B., Benninger, L. K., Blair, N. E., and Jahnke, R. A. (1999). Benthic fluxes and porewater concentration profiles of dissolved organic carbon in sediments from the North Carolina continental slope. *Geochim. Cosmochim. Acta.*, 63, 427–448, [https://doi.org/10.1016/S0016-7037\(99\)00032-0](https://doi.org/10.1016/S0016-7037(99)00032-0).
- Amon, R. M. W., Budéus, G., Meon, B. (2003). Dissolved organic carbon distribution and origin in the Nordic Seas: Exchanges with the Arctic Ocean and the North Atlantic. *J. Geophys. Res.*, 108. <https://doi.org/10.1029/2002JC001594>.
- An, H. S., Shim, K. S., Shin, H. R. (1994). On the warm eddies in the southwestern part of the East Sea (the Japan Sea). *J. Korean Soc. Oceanogr.*, 29, 152–163.
- Andreae, M. O. and Gelencsér, A. (2006). Black carbon or brown carbon? The nature of light-absorbing carbonaceous aerosols. *Atmospheric Chemistry and Physics*, 6, 3131–3148, <https://doi.org/10.5194/acp-6-3131-2006>.
- Baduel, C., Voisin, D., and Jaffrezo, J. L. (2009). Comparison of analytical methods for Humic Like Substances (HULIS) measurements in atmospheric particles. *Atmospheric Chemistry and Physics*, 9, 5949–5962, <https://doi.org/10.5194/acp-9-5949-2009>.
- Baduel, C., Voisin, D., and Jaffrezo, J. L. (2010). Seasonal variations of concentrations and optical properties of water soluble HULIS collected in urban environment. *Atmospheric Chemistry and Physics*, 10, 4085–4095, <https://doi.org/10.5194/acp-10-4085-2010>.
- Bae, Y. H., Kim, K. O., and Choi, B. H. (2010). Lake Sihwa tidal power plant project, *Ocean Engineering*, 37, 454–463, 119

<https://doi.org/10.1016/j.oceaneng.2010.01.015>.

- Bao, R., McIntyre, C., Zhao, M., Zhu, C., Kao, S.-J., Eglinton, T. I. (2016). Widespread dispersal and aging of organic carbon in shallow marginal seas. *Geology*, 44, 791–794.
- Bauer, J. E. and Bianchi, T. S. (2011). Dissolved organic carbon cycling and transformation, in: *Treatise on estuarine and coastal science*, edited by: Wolanski, E. and Mcluski, D. S., 5, 7–67, Academic Press, Waltham.
- Bauer, J. E., Cai, W.-J., Raymond, P. A., Bianchi, T. S., Hopkinson, C. S., Regnier, P. A. G. (2013). The changing carbon cycle of the coastal ocean. *Nature*, 504, 61–70.
- Bauer, J. E., Druffel, E. R. M. (1998). Ocean margins as a significant source of organic matter to the deep open ocean. *Nature*, 392, 483–485.
- Bauer, J. E., Druffel, E. R. M., Wolgast, D. M., Griffin, S. (2001). Sources and cycling of dissolved and particulate organic radiocarbon in the northwest Atlantic continental margin. *Global Biogeochemical Cycle*, 15, 615–636.
- Beaupre, S. R., Druffel, E. R. M., Griffin, S. (2007). A low blank photochemical extraction system for concentration and isotopic analyses of marine dissolved organic carbon. *Limnology and Oceanography: Methods*, 5, 174–184.
- Benner, R., Louchouart, P., Amon, R. M. W. (2005). Terrigenous dissolved organic matter in the Arctic Ocean and its transport to surface and deep waters of the North Atlantic. *Global Biogeochem. Cycles.*, 19, GB2025.
- Benner, R., Pakulski, J. D., McCarthy, M., Hedges, J. I., and Hatcher, P. G. (1992). Bulk chemical characteristics of dissolved organic matter in the ocean, *Science*, 255, 1561–1564, <https://doi.org/10.1126/science.255.5051.1561>.
- Birdwell, J. E. and Engel, A. S. (2010). Characterization of dissolved organic matter in cave and spring waters using UV-Vis absorbance and fluorescence spectroscopy, *Organic Geochemistry*, 41, 270–280, <https://doi.org/10.1016/j.orggeochem.2009.11.002>.
- Bro, R., 1997. PARAFAC. Tutorial and applications. *Chemometrics and Intelligent Laboratory Systems*, 38, 149–171.
- Carlson, C. A. and Hansell, D. A. (2015). Chapter 3 – DOM sources, sinks,

- reactivity, and budgets, in: *Biogeochemistry of marine dissolved organic matter* (Second Edition), edited by: Hansell, D. A. and Carlson, C. A., 65–126, Academic Press, Boston.
- Carpenter, J. H. (1965). The Chesapeake Bay institute technique for the Winkler dissolved oxygen method, *Limnology and Oceanography*, 10, 141–143.
- Catalá, T. S., Reche, I., Álvarez, M., Khatiwala, S., Guallart, E. F., Benítez-Barrios, V. M., Fuentes-Lema, A., Romera-Castillo, C., Nieto-Cid, M., Pelejero, C., Fraile-Nuez, E., Ortega-Retuerta, E., Marrasé, C., and Álvarez-Salgado, X. A. (2015). Water mass age and aging driving chromophoric dissolved organic matter in the dark global ocean, *Global Biogeochemical Cycle*, 29, 917–934, <https://doi.org/10.1002/2014GB005048>.
- Catalá, T. S., Reche, I., Fuentes-Lema, A., Romera-Castillo, C., Nieto-Cid, M., Ortega-Retuerta, E., Calvo, E., Álvarez, M., Marrasé, C., Stedmon, C. A., Álvarez-Salgado, X. A. (2015). Turnover time of fluorescent dissolved organic matter in the dark global ocean. *Nat. commun.*, 6, 5986.
- Chari, N. V. H. K., Sarma, N. S., Pandi, S. R., Murthy, K. N. (2012). Seasonal and spatial constraints of fluorophores in the midwestern Bay of Bengal by PARAFAC analysis of excitation emission matrix spectra. *Estuar. Coast. Shelf Sci.*, 100, 162–171.
- Chen, C.-T. A. (2009). Chemical and physical fronts in the Bohai, Yellow and East China Seas. *Journal of Marine Systems*, 78, 394–410.
- Chen, Q., Ikemori, F., and Mochida, M. (2016). Light absorption and excitation-emission fluorescence of urban organic aerosol components and their relationship to chemical structure, *Environmental Science and Technology*, 50, 10859–10868, <https://doi.org/10.1021/acs.est.6b02541>.
- Chen, X., Zhang, F., Lao, Y., Wang, X., Du, J., Santos, I. R. (2018). Submarine groundwater discharge-derived carbon fluxes in mangroves: An important component of blue carbon budgets? *Journal of Geophysical Research: Oceans*, 123, 6962–6979.
- Coble, P. G. (1996). Characterization of marine and terrestrial DOM in seawater

- using excitation-emission matrix spectroscopy. *Mar. Chem.*, 51, 325–346.
- Coble, P. G. (2007). Marine optical biogeochemistry: the chemistry of ocean color, *Chemical Reviews*, 107, 402–418, <https://doi.org/10.1021/cr050350+>.
- Cory, R. M., McKnight, D. M., Chin, Y. P., Miller, P., Jaros, C. L. (2007). Chemical characteristics of fulvic acids from Arctic surface waters: Microbial contributions and photochemical transformations. *J. Geophys. Res. Biogeosciences*, 112, G4.
- Dai, M. Yin, Z., Meng, F., Liu, Q., Cai, W-J. (2012). Spatial distribution of riverine DOC inputs to the ocean: an updated global synthesis. *Current Opinion in Environmental Sustainability*, 4, 170–178.
- Das, O., Wang, Y., and Hsieh, Y.-P. (2010). Chemical and carbon isotopic characteristics of ash and smoke derived from burning of C₃ and C₄ grasses, *Organic Geochemistry*, 41, 263–269, <https://doi.org/10.1016/j.orggeochem.2009.11.001>.
- Dasari, S., Andersson, A., Bikkina, S., Holmstrand, H., Budhavant, K., Satheesh, S., Asmi, E., Kesti, J., Backman, J., Salam, A., Bisht, D. S., Tiwari, S., Hameed, Z., and Gustafsson, Ö. (2019). Photochemical degradation affects the light absorption of water-soluble brown carbon in the South Asian outflow, *Science Advances*, 5, eaau8066, <https://doi.org/10.1126/sciadv.aau8066>.
- Del Vecchio, R. and Blough, N. V. (2002). Photobleaching of chromophoric dissolved organic matter in natural waters: Kinetics and modelling, *Marine Chemistry*, 78, 231–253, [https://doi.org/10.1016/S0304-4203\(02\)00036-1](https://doi.org/10.1016/S0304-4203(02)00036-1).
- Després, V. R., Huffman, J. A., Burrows, S. M., Hoose, C., Safatov, A. S., Buryak, G., Fröhlich-Nowoisky, J., Elbert, W., Andreae, M. O., Pöschl, U., and Jaenicke, R. (2012). Primary biological aerosol particles in the atmosphere: a review, *Tellus B*, 64, 15598, <https://doi.org/10.3402/tellusb.v64i0.15598>.
- Druffel, E. R. M. (1992). Cycling of dissolved and particulate organic matter in the open ocean. *Journal of Geophysical Research*, 97, 639–659.
- Druffel, E. R. M., Bauer, J. E. (2000). Radiocarbon distributions in Southern Ocean dissolved and particulate organic matter. *Geophysical Research Letters*, 27, 1495–1498.
- Druffel, E. R. M., Griffin, S. (2015). Radiocarbon in dissolved organic carbon of

- the South Pacific Ocean. *Geophysical Research Letters*, 42, 4096–4101.
- Druffel, E. R. M., Griffin, S., Honjo, S., and Manganini, J. (1998). Evidence of old carbon in the deep water column of the Panama Basin from natural radiocarbon measurements. *Geophysical Research Letters*, 25, 1733–1736.
- Duarte, R. M. B. O. and Duarte, A. C. (2013). Atmospheric organic matter, *eMagRes*, 2, 415–426, <https://doi.org/10.1002/9780470034590.emrstm1331>.
- Dunne, J. P., Sarmiento, J. L., Gnanadesikan, A. (2007). A synthesis of global particle export from the surface ocean and cycling through the ocean interior and on the seafloor. *Global Biogeochemical Cycle*, 21, GB4006.
- Feng, Y., Ramanathan, V., and Kotamarthi, V. R. (2013). Brown carbon: A significant atmospheric absorber of solar radiation, *Atmospheric Chemistry Physics*, 13, 8607–8621, <https://doi.org/10.5194/acp-13-8607-2013>.
- Fichot, C. G. and Benner, R. (2012). The spectral coefficient of chromophoric dissolved organic matter ($S_{275-295}$) as a tracer of terrigenous dissolved organic carbon in river-influenced ocean margins. *Limnology and Oceanography*, 57, 1453–1466.
- Fichot, C. G., Lohrenz, S. E., and Benner, R. (2014). Pulsed, cross-shelf export of terrigenous dissolved organic carbon to the Gulf of Mexico. *Journal of Geophysical Research*, 119, 1176–1194.
- Follett, C. L., Repeta, D. J., Rothman, D. H., Xu, L., and Santinelli, C. (2014). Hidden cycle of dissolved organic carbon in the deep ocean. *Proceedings of the National Academy of Sciences*, 111, 16706–16711.
- Forrister, H., Liu, J., Scheuer, E., Dibb, J., Ziemba, L., Thornhill, K. L., Anderson, B., Diskin, B., Perring, A. E., Schwarz, J. P., Campuzano-Jost, P., Day, D. A., Palm, B. B., Jimenez, J. L., Nenes, A., and Weber, R. J. (2015). Evolution of brown carbon in wildfire plumes, *Geophysical Research Letters*, 42, 4623–4630, <https://doi.org/10.1002/2015GL063897>.
- Fu, P., Kawamura, K., Chen, J., Qin, M., Ren, L., Sun, Y., Wang, Z., Barrie, L. A., Tachibana, E., Ding, A., and Yamashita, Y. (2015). Fluorescent water-soluble organic aerosols in the High Arctic atmosphere, *Scientific Reports*, 5, 9845, <https://doi.org/10.1038/srep09845>.
- Fukuzaki, K., Imai, I., Fukushima, K., Ishii, K. I., Sawayama, S., Yoshioka, T. (2014). Fluorescent characteristics of dissolved organic matter produced by

- bloom-forming coastal phytoplankton. *J. Plankton Res.*, 36, 685–694.
- Gabriel, R., Mayol-Bracero, O. L., and Andreae, M. O. (2002). Chemical characterization of submicron aerosol particles collected over the Indian Ocean, *Journal of Geophysical Research*, 107, 8005, <https://doi.org/10.1029/2000JD000034>.
- Gearing, J. N. (1988). The use of stable isotope ratios of tracing the nearshore-offshore exchange of organic matter, in: *Coastal-offshore ecosystem interactions*, edited by: Jansson, B.-O., 69–101, Springer-Verlag, Berlin.
- Gelencsér, A., May, B., Simpson, D., Sánchez-Ochoa, A., Kasper-Giebl, A., Puxbaum, H., Caseiro, A., Pio, C., and Legrand, M. (2007). Source appointment of PM_{2.5} organic aerosol over Europe: Primary/secondary, natural/anthropogenic, and fossil/biogenic origin. *Journal of Geophysical Research: Atmospheres*, 112, D23, <https://doi.org/10.1029/2006JD008094>.
- Ghan, S. J. and Schwartz, S. E. (2007). Aerosol properties and processes: A path from field and laboratory measurements to global climate models, *American Meteorological Society*, 88, 1059–1083.
- Goldstein, A. H. and Galbally, I. E. (2007). Known and unexplored organic constituents in the Earth's atmosphere. *Environmental Science and Technology*, 41, 1514–1521.
- Graber, E. R. and Rudich, Y. (2006). Atmospheric HULIS: How humic-like are they? A comprehensive and critical review. *Atmospheric Chemistry and Physics*, 6, 729–735, <https://doi.org/10.5194/acp-6-729-2006>.
- Griffith, D. R. and Raymond, P. A. (2011). Multiple-source heterotrophy fuelled by aged organic carbon in an urbanized estuary. *Marine Chemistry*, 124, 14–22, <https://doi.org/10.1016/j.marchem.2010.11.003>.
- Gu, H., Moore, W. S., Zhang, L., Du, J., and Zhang, J. (2012). Using radium isotopes to estimate the residence time and the contribution of submarine groundwater discharge (SGD) in the Changjiang effluent plume, East China Sea. *Continental Shelf Research*, 35, 95–107.
- Guo, L. and Macdonald, R. W. (2006). Source and transport of terrigenous organic matter in the upper Yukon River: Evidence from isotope ($\delta^{13}\text{C}$, $\Delta^{14}\text{C}$, and $\delta^{15}\text{N}$) composition of dissolved, colloidal, and particulate phases. *Global Biogeochemical Cycle*, 20, GB2011.

- Gustafsson, Ö., Kruså, M., Zencak, Z., Sheesley, R. J., Granat, L., Engström, E., Praveen, P. S., Rao, P. S. P., Leck, C., and Rodhe, H. (2009). Brown clouds over South Asia: biomass or fossil fuel combustion? *Science*, 323, 495–498, <https://doi.org/10.1126/science.1164857>.
- Han, H., Kim, G., Seo, H., Shin, K.-H., and Lee, D.-H. (2020). Significant seasonal changes in optical properties of brown carbon in the midlatitude atmosphere, *Atmospheric Chemistry and Physics*, 20, 2709–2718, <https://doi.org/10.5194/acp-20-2709-2020>.
- Hansell, D. A. (2005). Dissolved organic carbon reference material program. *EOS American Geophysical Union*, 86, 318.
- Hansell, D. A., Carlson, C. A. (1998). Deep-ocean gradients in the concentration of dissolved organic carbon. *Nature*, 395, 263–266.
- Hansen, A. M., Kraus, T. E. C., Pellerin, B. A., Fleck, J. A., Downing, B. D., and Bergamaschi, B. A. (2016). Optical properties of dissolved organic matter (DOM): Effects of biological and photolytic degradation. *Limnology and Oceanography*, 61, 1015–1032, <https://doi.org/10.1002/lno.10270>.
- Healy, R. M., Wang, J. M., Sofowote, U., Su, Y., Debosz, J., Noble, M., Munoz, A., Jeong, C.-H., Hilker, N., Evans, G. J., and Doerksen, G. (2019). Black carbon in the Lower Fraser Valley, British Columbia: Impact of 2017 wildfires on local air quality and aerosol optical properties. *Atmospheric Environment*, 217, 116976, <https://doi.org/10.1016/j.atmosenv.2019.116976>.
- Hedges, J. I., Ertel, J. R., Quay, P. D., Grootes, P. M., Richey, J. E., Devol, A. H., Farwell, G. W., Schmidt, F. W., and Salati, E. (1986). Organic carbon-14 in the Amazon River system. *Science*, 231, 1129–1131.
- Helms, J. R., Stubbins, A., Perdue, E. M., Green, N. W., Chen, H. and Mopper, K. (2013). Photochemical bleaching of oceanic dissolved organic matter and its effects on absorption spectral slope and fluorescence. *Marine Chemistry*, 155, 81–91.
- Helms, J. R., Stubbins, A., Ritchie, J. D., and Minor, E. C. (2008). Absorption spectral slopes and slope ratios as indicators of molecular weight, source, and photobleaching of chromophoric dissolved organic matter, *Limnology and Oceanography*, 53, 955–969, <https://doi.org/10.4319/lo.2008.53.3.0955>.
- Hennigan, C. J., Sullivan, A. P., Collett, J. L., and Robinson, A. L. (2010).

- Levoglucosan stability in biomass burning particles exposed to hydroxyl radicals, *Geophysical Research Letters*, 37, L09806, <https://doi.org/10.1029/2010GL043088>.
- Hoffer, A., Gelencsér, A., Guyon, P., Kiss, G., Schmid, O., Frank, G. P., Artaxo, P., and Andreae, M. O. (2006). Optical properties of humic-like substances (HULIS) in biomass-burning aerosols. *Atmospheric Chemistry and Physics*, 6, 3563–3570, <https://doi.org/10.5194/acp-6-3563-2006>.
- Hoffmann, D., Tilgner, A., Iinuma, Y., and Herrmann, H. (2010). Atmospheric stability of levoglucosan: a detailed laboratory and modeling study, *Environmental Science and Technology*, 44, 694–699, <https://doi.org/10.1021/es902476f>.
- Hopkinson, C. S. and Vallino, J. J. (2005). Efficient export of carbon to the deep ocean through dissolved organic matter. *Nature*, 433, 142–145.
- Huang, T.-H., Fu, Y.-H., Pan, P.-Y., and Chen, C.-T. A. (2012). Fluvial carbon fluxes in tropical rivers. *Current Opinion in Environmental Sustainability*, 4, 162–169.
- Hung, J.-J., Chen, C.-H., Gong G.-C., Sheu, D.-D., and Shiah, F.-K. (2002). Distributions, stoichiometric patterns and cross-shelf exports of dissolved organic matter in the East China Sea. *Deep-sea Research. Part II*, 50, 1127–1145.
- Hur, H. B., Jacobs, G. A., and Teague, W. J. (1999). Monthly variations of water masses in the Yellow and East China Seas, November 6, 1998. *Journal of Oceanography*, 55, 171–184.
- Hwang, J., Druffel, E. R. M., and Eglinton, T. I. (2010). Widespread influence of resuspended sediments on oceanic particulate organic carbon: Insights from radiocarbon and aluminum contents in sinking particles. *Global Biogeochemical cycles*, 24, GB4016.
- Hyun, J. H., Kim, D., Shin, C., Noh, J. H., Yang, E. J., Mok, J. S., Kim, S. H., Kim, H., Yoo, S. (2009). Enhanced phytoplankton and bacterioplankton production coupled to coastal upwelling and anticyclonic eddy in the Ulleung Basin, East Sea. *Aquat. Microb. Ecol.*, 54, 45–55.
- Iavorivska, L., Boyer, E. W., and DeWalle, D. R. (2016). Atmospheric deposition of organic carbon via precipitation. *Atmospheric Environment*, 146, 153–

- Jiao, N., Herndl, G. J., Hansell, D. A., Benner, R., Kattner, G., Wilhelm, S. W., Kirchman, D. L., Weinbauer, M. G., Luo, T., Chen, F., and Azam, F. (2010). Microbial production of recalcitrant dissolved organic matter: Long-term carbon storage in the global ocean. *Nature Reviews Microbiology*, 8, 593–599.
- Jørgensen, L., Stedmon, C. A., Kragh, T., Markager, S., Middelboe, M., and Søndergaard, M. (2011). Global trends in the fluorescence characteristics and distribution of marine dissolved organic matter. *Marine Chemistry*, 126, 139–148, <https://doi.org/10.1016/j.marchem.2011.05.002>.
- Kanakidou, M., Duce, R. A., Prospero, J. M., Baker, A. R., Benitez-Nelson, C., Dentener, F. J., Hunter, K. A., Liss, P. S., Mahowald, N., Okin, G. S., Sarin, M., Tsigaridis, K., Uematsu, M., Zamora, L. M., and Zhu, T. (2012). Atmospheric fluxes of organic N and P to the global ocean. *Global Biogeochemical Cycle*, 26, GB3026.
- Kanakidou, M., Seinfeld, J. H., Pandis, S. N., Barnes, I., Dentener, F. J., Facchini, M. C., Van Dingenen, R., Ervens, B., Nenes, A., Nielsen, C. J., Swietlicki, E., Putaud, J. P., Balkanski, Y., Fuzzi, S., Horth, J., Moortgat, G. K., Winterhalter, R., Myhre, C. E. L., Tsigaridis, K., Vignati, E., Stephanou, E. G., and Wilson, J. (2005). Organic aerosol and global climate modelling: a review, *Atmospheric Chemistry and Physics*, 5, 1053–1123, <https://doi.org/10.5194/acp-5-1053-2005>.
- Kawakami, H. and Kusakabe, M. (2008). Surface water mixing estimated from ^{228}Ra and ^{226}Ra in the northwestern North Pacific. *Journal of Environmental Radioactivity*, 99, 1335–1340.
- Kawasaki, N. and Benner, R. (2006). Bacterial release of dissolved organic matter during cell growth and decline: molecular origin and composition. *Limnology and Oceanography*, 51, 2170–2180, <https://doi.org/10.4319/lo.2006.51.5.2170>.
- Kawashima, H. and Haneishi, Y. (2012). Effects of combustion emissions from the Eurasian continent in winter on seasonal $\delta^{13}\text{C}$ of elemental carbon in aerosols in Japan. *Atmospheric Environment*, 46, 568–579, <https://doi.org/10.1016/j.atmosenv.2011.05.015>.

- Kelly, S. D., Stein, C., and Jickelle, T. D. (2005). Carbon and nitrogen isotopic analysis of atmospheric organic matter. *Atmospheric Environment*, 39, 6007–6011, <https://doi.org/10.1016/j.atmosenv.2005.05.030>.
- Kieber, R. J., Whitehead, R. F., Reid, S. N., Willey, J. D., and Seaton, P. J. (2006). Chromophoric dissolved organic matter (CDOM) in rainwater, Southeastern North Carolina, USA. *Journal of Atmospheric Chemistry*, 54, 21–41.
- Kim, D., Yang, E. J., Kim, K. H., Shin, C. W., Park, J., Yoo, S., Hyun, J. H. (2012). Impact of an anticyclonic eddy on the summer nutrient and chlorophyll a distributions in the Ulleung Basin, East Sea (Japan Sea). *ICES J. Mar. Sci.*, **69**, 23–29. <https://doi.org/10.1093/icesjms/fsr178>.
- Kim, G., Lee, K.-K., Park, K.-S., Hwang, D.-W., and Yang, H.-S. (2003). Large submarine groundwater discharge (SGD) from a volcanic island. *Geophysical Research Letters*, 30, 2098.
- Kim, G., Ryu, J.-W., Yang, H.-S., and Yun, S.-T. (2005). Submarine groundwater discharge (SGD) into the Yellow Sea revealed by ^{228}Ra and ^{226}Ra isotopes: Implications for global silicate fluxes. *Earth and Planetary Science Letters*, 237, 156–166.
- Kim, J. and Kim, G. (2015). Importance of colored dissolved organic matter (CDOM) inputs from the deep sea to the euphotic zone: Results from the East (Japan) Sea. *Mar. Chem.*, 169, 33–40.
- Kim, J. and Kim, G. (2016). Significant anaerobic production of fluorescent dissolved organic matter in the deep East Sea (Sea of Japan). *Geophysical Research Letters*, 43, 7609–7616, <https://doi.org/10.1002/2016GL069335>.
- Kim, J. and Kim, T.-H. (2018). Distribution of humic fluorescent dissolved organic matter in lake Shihwa: the role of the redox condition. *Estuaries and Coasts*, <https://doi.org/10.1007/s12237-018-00491-0>.
- Kim, J., Cho, H.-M., and Kim, G. (2015). ^{228}Ra flux in the northwestern Pacific Marginal Seas: Implications for disproportionately large submarine groundwater discharge. *Ocean Science Journal*, 50, 195–202.
- Kim, J., Cho, H.-M., and Kim, G. (2018). Significant production of humic fluorescent dissolved organic matter in the continental shelf waters of the northwestern Pacific Ocean. *Scientific Reports*, 8, 4887.
- Kim, K., Kim, K.-R., Kim, Y. G., Cho, Y. K., Kang, D. J., Takematsu, M., Volkov,

- Y. (2004). Water masses and decadal variability in the East Sea (Sea of Japan). *Prog. Oceanogr.*, 61, 157–174.
- Kim, K. T., Kim, E. S., Cho, S. R., and Park, J. K. (2009). Distribution and temporal change of heavy metals in the surface sediments of lake Shihwa and adjacent sea, Korea. *Journal of Coastal Research*, 56, 817–821.
- Kim, K.-R., Kim, K. (1996). What is happening in the East Sea (Japan Sea)? Recent chemical observations during CREAMS 93–96. *J. Korean Soc. Oceanogr.*, 31, 164–172.
- Kim, K.-R., Lee, S. H., Park, K.-A., Park, J. J., Suh, Y.-S., Lee, D.-K., Kang, D.-J., and Chang, K.-I. (2015a) General Introduction. In: Chang Ki et al. (eds) *Oceanography of the East Sea (Japan Sea)*. Springer, Cham, 1–31.
- Kim, M., Hwang, J., Rho, T., Lee, T., Kang, D. J., Chang, K. I., Noh, S., Joo, H., Kwak, J. H., Kang, C. K., and Kim, K. R. (2017). Biogeochemical properties of sinking particles in the southwestern part of the East Sea (Japan Sea). *Journal of Marine Systems*, 167, 33–42.
- Kim, T.-H. and Kim, G. (2010). Distribution of dissolved organic carbon (DOC) in the southwestern East Sea in summer. *Ocean Polar Research*, 32, 291–297.
- Kim, T.-H. and Kim, G. (2013). Changes in seawater N:P ratios in the northwestern Pacific Ocean in response to increasing atmospheric N deposition: Results from the East (Japan) Sea. *Limnol. Oceanogr.*, 58, 1907–1914.
- Kim, T.-H. and Kim, G. (2014). Estimating benthic fluxes of trace elements to hypoxic coastal waters using ^{210}Po . *Estuarine, Coastal and Shelf Science*, 151, 324–330, <https://doi.org/10.1016/j.ecss.2014.05.008>.
- Kim, T.-H., Kim, G., Lee, S.-A., and Dittmar, T. (2015b). Extraordinary slow degradation of dissolved organic carbon (DOC) in a cold marginal sea. *Scientific Reports*, 5, 13808, <https://doi.org/10.1038/srep13808>.
- Kim, T.-H., Kwon, E., Kim, I., Lee, S.-A., and Kim, G. (2013). Dissolved organic matter in the subterranean estuary of a volcanic island, Jeju: Importance of dissolved organic nitrogen fluxes to the ocean. *Journal of Sea Research*, 78, 18–24.
- Kinsey, J. D., Corradino, G., Ziervogel, K., Schnetzer, A., Osburn, C. L. (2018). Formation of chromophoric dissolved organic matter by bacterial

- degradation of phytoplankton-derived aggregates. *Front. Mar. Sci.*, 4, 430.
- Kirillova, E. N., Andersson, A., Han, J., Lee, M., and Gustafsson, Ö. (2014a). Sources and light absorption of water-soluble organic carbon aerosols in the outflow from northern China. *Atmospheric Chemistry and Physics*, 14, 1413–1422, <https://doi.org/10.5194/acp-14-1413-2014>.
- Kirillova, E. N., Andersson, A., Tiwari, S., Sribastava, A. K., Bisht, D. S., and Gustafsson, Ö. (2014b). Water-soluble organic carbon aerosols during a fall New Delhi winter: Isotope-based source apportionment and optical properties. *Journal of Geophysical Research: Atmosphere*, 119, 3476–3485, <https://doi.org/10.1002/2013JD020041>.
- Koepfler, E. T., Benner, R., and Montagna, P. A. (1993). Variability of dissolved organic carbon in sediments of a Seagrass bed and an unvegetated area within an estuary in Southern Texas. *Estuaries*, 16, 391–404.
- Kolasinski, J., Kaehler, S., and Jaquemet, S. (2012). Distribution and sources of particulate organic matter in a mesoscale eddy dipole in the Mozambique Channel (south-western Indian Ocean): Insight from C and N stable isotopes. *J. Mar. Syst.* 96–97, 122–131. <https://doi.org/10.1016/j.jmarsys.2012.02.015>.
- Kothawala, D.N., Murphy, K. R., Stedmon, C. A., Weyhenmeyer, G. A., and Tranvik, L. J. (2013). Inner filter correction of dissolved organic matter fluorescence. *Limnol. Oceanogr. Meth*, 11, 616–630.
- Kowalczyk, P., Copper, W. J., Whitehead, R. F., Durako, M. J., and Sheldon, W. (2003). Characterization of CDOM in an organic rich river and surrounding coastal ocean in the South Atlantic Bight. *Aquatic Sciences*, 65, 381–398.
- Kowalczyk, P., Zablocka, M., Sagan, S., and Kulinski, K. (2010). Fluorescence measured in situ as a proxy of CDOM absorption and DOC concentration in the Baltic Sea. *Oceanologia*, 52, 431–471.
- Kuang, B. Y., Lin, P., Huang, X. H. H., and Yu, J. Z. (2015). Sources of humic-like substances in the Pearl River Delta, China: positive matrix factorization analysis of PM_{2.5} major components and source markers. *Atmospheric Chemistry and Physics*, 15, 1995–2008, <https://doi.org/10.5194/acp-15-1995-2015>.
- Kuhlbusch, T. (1998). Black carbon and the carbon cycle. *Science*, 280, 1903.

- Laglera, L. M., Battaglia, G., and van den Berg, C. M. G. (2007). Determination of humic substances in natural waters by cathodic stripping voltammetry of their complexes with iron. *Anal. Chim. Acta.* 599, 58–66. <https://doi.org/10.1016/j.aca.2007.07.059>.
- Laglera, L. M. and van den Berg, C. M. G. (2009). Evidence for geochemical control of iron by humic substances in seawater. *Limnol. Oceanogr.* 54, 610–619.
- Lakowicz, J.R. (1983). *Principles of fluorescence spectroscopy*. Plenum Press, New York, 529–575 p.
- Lang, S. Q., Lilley, M. D., and Hedge, J. I. (2007). A method to measure the isotopic (^{13}C) composition of dissolved organic carbon using a high temperature combustion instrument. *Marine Chemistry*, 103, 318–326.
- Laskin, A., Laskin, J., and Nizkorodov, S. A. (2009). Chemistry of Atmospheric Brown Carbon, *Chemical Reviews*, 115, 4335–4382, <https://doi.org/10.1021/cr5006167>.
- Lawaetz, A. J. and Stedmon, C. A. (2009). Fluorescence intensity calibration using the raman scatter peak of water, *Applied Spectroscopy*, 63, 936–940, <https://doi.org/10.1366/000370209788964548>.
- Lead, C. (2001). The carbon cycle and atmospheric carbon dioxide. 183–238, www.grida.no/climate/ipcc_tar_wgl/pdf/tar-03.pdf.
- Lee, C.-H., Lee, B.-Y., Chang, W. K., Hong, S., Song, S. J., Park, J., Kwon, B., Khim, J. S. (2014). Environmental and ecological effects of Lake Shihwa reclamation project in South Korea: A review, *Ocean and Coastal Management*, 102, 545–558, <https://doi.org/10.1016/j.ocecoaman.2013.12.018>.
- Lee, H., Kim, G., Kim, J., Park, G., and Song, K.-H. (2014). Tracing the flow rate and mixing ratio of the Changjiang diluted water in the northwestern Pacific marginal seas using radium isotopes. *Geophysical Research Letters*, 41, 4637–4645.
- Lee, H. S., Kwon, K. K., Yang, S. H., Bae, S. S., Park, C. H., Kim, S. J., Lee, J. H. (2008). Description of *Croceitalea* gen. nov. in the family *Flavobacteriaceae* with two species, *Croceitalea eckloniae* sp. nov. and *Croceitalea dokdonensis* sp. nov., isolated from the rhizosphere of the marine algae

- Ecklonia kurome. *International Journal of Systematic and Evolutionary Microbiology*, 58, 2505–2510.
- Lee, J., Hong, S., Yoon, S. J., Kwon, B., Ryu, J., Giesy, J. P., Allam, A. A., Alkhedhairy, A. A., and Khim, J. S. (2017). Long-term changes in distributions of dioxin-like and estrogenic compounds in sediments of Lake Sihwa, Korea: Revisited mass balance. *Chemosphere*, 181, 767–777, <https://doi.org/10.1016/j.chemosphere.2017.04.074>.
- Lee, S.-A. and Kim, G. (2018). Sources, fluxes, and behaviors of fluorescent dissolved organic matter (FDOM) in an estuarine mixing zone: Results from the Nakdong-River Estuary. *Biogeosciences*, 15, 1115–1122.
- Lee, S.-A., Kim, T.-H., and Kim, G. (2020). Tracing terrestrial versus marine sources of dissolved organic carbon in a coastal bay using stable carbon isotopes. *Biogeosciences*, 17, 135–144, <https://doi.org/10.5194/bg-17-135-2020>.
- Lee, S.-A., Lee, J., Han, Y., and Kim, G. (2020). Biogeochemical alteration and fluxes of dissolved organic matter and nutrients in coastal bays. *Estuar. Coast. Shelf Sci.*, 245, 106992, <https://doi.org/10.1016/j.ecss.2020.106992>.
- Lee, S.-I., Kim, B.-C., and Oh, H.-J. (2002). Evaluation of lake modification alternatives for Lake Sihwa, Korea, *Environmental Management*, 29, 57–66, <https://doi.org/10.1007/s00267-001-0040-0>.
- Legg, S. (2021). Mixing by oceanic lee waves. *Ann. Rev. Fluid Mech.* 53, 173–201.
- Li, X., Han, J., Hopke, P. K., Hu, J., Shu, Q., Chang, Q., and Ying, Q. (2019). Quantifying primary and secondary humic-like substances in urban aerosol based on emission source characterization and a source-oriented air quality model. *Atmospheric Chemistry and Physics*, 19, 2327–2341, <https://doi.org/10.5194/acp-19-2327-2019>.
- Lie, H.-J. and Cho, C.-H. (2016). Seasonal circulation patterns of the Yellow and East China Sea derived from satellite-tracked drifter trajectories and hydrographic observations. *Progress Oceanography*, 146, 121–141.
- Lin, C. Y., Sheng, Y. F., Chen, W. N., Wang, Z., Kuo, C. H., Chen, W. C., and Yang, T. (2012). The impact of channel effect on Asian dust transport dynamics: a case in southeastern Asia. *Atmospheric Chemistry and Physics*, 12, 271–285,

<https://doi.org/10.5194/acp-12-271-2012>.

- Lin, P., Huang, X.-F., He, L.-Y., and Yu, J. Z. (2010). Abundance and size distribution of HULIS in ambient aerosols at a rural site in South China. *Journal of Aerosol Science*, 41, 74–87, <https://doi.org/10.1016/j.jaerosci.2009.09.001>.
- Lukács, H., Gelencsér, A., Hammer, S., Puxbaum, H., Pio, C., Legrand, M., Kasper-Giebl, A., Handler, M., Limbeck, A., Simpson, D., and Preunkert, S. (2007). Seasonal trends and possible sources of brown carbon based on 2-year aerosol measurements at six sites in Europe. *Journal of Geophysical Research*, 122, D23S18, <https://doi.org/10.1029/2006JD008151>.
- MacKinnon, J. A., Zhao, Z., Whalen, C. B., Waterhouse, A. F., Trossman, D. S., Sun, O. M., St Laurent, L. C., Simmons, H. L., Polzin, K., Pinkel, R., Pickering, A., Norton, N. J., Nash, J. D., Musgrave, R., Merchant, L. M., Melet, A. V., Mater, B., Legg, S., Large, W. G., Kenze, E., Klymak, J. M., Jochum, M., Jayne, S. R., Hallberg, R. W., Griffies, S. M., Diggs, S., Danabasoglu, G., Chassignet, E. P., Buijsman, M. C., Bryan, F. O., Briegleb, B. P., Barna, A., Arbic, B. K., Ansong, J. K., and Alford, M. H. (2017). Climate process team on internal wave-driven ocean mixing. *Bull. Amer. Meteor.* 98, 2429–2454. <https://doi.org/10.1175/BAMS-D-16-0030.1>.
- Maenhaut, W., Raes, N., Chi, X., Cafmeyer, J., and Wang, W. (2007). Chemical composition and mass closure for PM_{2.5} and PM₁₀ aerosols at K-puszt, Hungary, in summer 2006. *X-RAY Spectrometry*, 37, 193–197, <https://doi.org/10.1002/xrs.1062>.
- Masiello, C. A. and Druffel, E. R. M. (1998). Black carbon in deep-sea sediments. *Science*, 280, 1911–1913.
- Matos, J. T. V., Freire, S. M. S. C., Duarte, R. M. B. O., and Duarte, A. C. (2015). Natural organic matter in urban aerosols: comparison between water and alkaline soluble components using excitation-emission matrix fluorescence spectroscopy and multiway data analysis. *Atmospheric Environment*, 102, 1–10, <https://doi.org/10.1016/j.atmosenv.2014.11.042>.
- Maybeck, M. (1982). Carbon, nitrogen, and phosphorus transport by world rivers. *American Journal of Science*, 282, 401–450.

- McGillicuddy Jr. D. J. and Robinson, A. R. (1997). Eddy-induced nutrient supply and new production in the Sargasso Sea. *Deep-Sea Res. Pt 1*, 44, 1427–1450.
- Mendoza, W. G., Kang, Y., Zika, R. G. (2012). Resolving DOM fluorescence fractions during a *Karenia brevis* bloom patch on the Southwest Florida Shelf. *Continental Shelf Res.*, 32, 121–129.
- Mladenov, N., Lopez-Ramos, J., McKnight, D. M., and Reche, I. (2009). Alpine lake optical properties as sentinels of dust deposition and global change. *Limnology and Oceanography*, 54, 6–2, 2386–2400, https://doi.org/10.4319/lo.2009.54.6_part_2.2386.
- Mladenov, N., Sommaruga, R., Morales-Baquero, R., Laurion, I., Camarero, L., Diéguez, M. C., Camacho, A., Delgado, A., Torres, O., Chen, Z., Felip, M., and Reche, I. (2011). Dust inputs and bacteria influence dissolved organic matter in clear alpine lakes. *Nature Communication*, 2, 405, <https://doi.org/10.1038/ncomms1411>.
- Moore, W. S. (1976). Sampling ^{228}Ra in the deep ocean. *Deep-Sea Research Oceanographic Abstracts*, 23, 647–651.
- Moran, M. A., Sheldon, W. M., and Zepp, R. G. (2000). Carbon loss and optical property changes during long-term photochemical and biological degradation of estuarine dissolved organic matter. *Limnology and Oceanography*, 45, 1254–1264.
- Murphy, K. R., Stedmon, C. A., Wenig, P., and Bro, R. (2014). OpenFluor- an online spectral library of auto-fluorescence by organic compounds in the environment. *Analytical Methods*, 6, 658–661.
- Nelson, N. B. and Gauglitz, J. M. (2016). Optical signatures of dissolved organic matter transformation in the global ocean. *Front. Mar. Sci.*, 2, 118. <https://doi.org/10.3389/fmars.2015.00118>.
- Nelson, N. B., Siegel, D. A. (2013). The global distribution and dynamics of chromophoric dissolved organic matter. *Ann. Rev. Mar. Sci.*, 5, 447–476.
- Nozaki, Y., Kasemsupaya, V., and Tsubota, H. (1989). Mean residence time of the shelf water in the East China and the Yellow Seas determined by $^{228}\text{Ra}/^{226}\text{Ra}$ measurements. *Geophysical Research Letters*, 16, 1297–1300.
- Nozaki, Y., Kasemsupaya, V., and Tsubota, H. (1990). The distribution of ^{228}Ra and ^{226}Ra in the surface waters of the northern North Pacific. *Geochemical*

Journal, 24, 1–6.

- Nozaki, Y., Tsubota, H., Kasemsupaya, V., Yashima, M., and Ikuta, N. (1991). Residence times of surface water and particle-reactive ^{210}Pb and ^{210}Po in the East China and Yellow Seas. *Geochimica et Cosmochimica Acta*, 55, 1265–1272.
- Opsahl, S. and Benner, R. (1997). Distribution and cycling of terrigenous dissolved organic matter in the ocean. *Nature*, 386, 480–482, <https://doi.org/10.1038/386480a0>.
- Parlanti, E., Wörz, K., Geoffroy, L., and Lamotte, M. (2000). Dissolved organic matter fluorescence spectroscopy as a tool to estimate biological activity in a coastal zone submitted to anthropogenic inputs. *Org. Geochem.*, 31, 1765–1781.
- Painter, S. C., Lapworth, D. J., Malcolm, E., Woodward, S., Kroeger, S., Evans, C. D., Mayor, D. J., and Sanders, R. J. (2018). Terrestrial dissolved organic matter distribution in the North Sea. *Science of the Total Environment*, 630, 630–647.
- Panetta, R. J., Ibrahim, M., and Gélinas, Y. (2008). Coupling a high-temperature catalytic oxidation total organic carbon analyzer to an isotope ratio mass spectrometer to measure natural-abundance $\delta^{13}\text{C}$ -dissolved organic carbon in marine and freshwater samples. *Analytical Chemistry*, 80, 5232–5239, <https://doi.org/10.1021/ac702641z>.
- Park, S. S. and Son, S.-C. (2017). Relationship between carbonaceous components and aerosol light absorption during winter at an urban site of Gwangju, Korea, *Atmospheric Research*, 185, 73–83, <https://doi.org/10.1016/j.atmosres.2016.11.005>.
- Park, S. S., Kim, Y. J., Cho, S. Y., and Kim, S. J. (2007). Characterization of $\text{PM}_{2.5}$ aerosols dominated by local pollution and Asian dust observed at an urban site in Korea during aerosol characterization experiments (ACE)-Asia project. *Journal of the Air and Waste Management Association*, 57, 434–443.
- Pöhlker, C., Huffman, J. A., and Pöschl, U. (2012). Autofluorescence of atmospheric bioaerosols – fluorescent biomolecules and potential interferences. *Atmospheric Measurement Techniques*, 5, 37–71, <https://doi.org/10.5194/amt-5-37-2012>.

- Polzin, K. L., Toole, J. M., Ledwell, J. R., and Schmitt, R. W. (1997). Spatial variability of turbulent mixing in the abyssal ocean. *Science* 276, 93–96. doi:10.1126/science.276.5309.93.
- Ra, K., Bang, J.-H., Lee, J.-M., Kim, K.-T., and Kim, E.-S. (2011). The extent and historical trend of metal pollution recorded in core sediments from the artificial Lake Shihwa, Korea. *Marine Pollution Bulletin*, 62, 1814–1821, <https://doi.org/10.1016/j.marpolbul.2011.05.010>.
- Ramanathan, V., Ramana, M. V., Roberts, G., Kim, D., Corrigan, C., Chung, C., and Winker, D. (2007). Warming trends in Asia amplified by brown cloud solar absorption, *Nature*, 448, 575–578, <https://doi.org/10.1038/nature06019>.
- Raymond, P. A. and Bauer, J. E. (2001a). Riverine export of aged terrestrial organic matter to the North Atlantic Ocean. *Nature*, 409, 497–500.
- Raymond, P. A. and Bauer, J. E. (2001b). Use of ^{14}C and ^{13}C natural abundances for evaluating riverine, estuarine, and coastal DOC and POC sources and cycling: a review and synthesis. *Organic Geochemistry* 32, 469–485.
- Raymond, P. A. and Spencer, R. G. M. (2015). Chapter 11 – Riverine DOM, in: *Biogeochemistry of marine dissolved organic matter (Second Edition)*, edited by: Hansell, D. A. and Carlson, C. A., 509–535, Academic Press, Boston.
- Romera-Castillo, C., Sarmiento, H., Alvarez-Salgado, X. A., Gasol, J. M., Marrase, C. (2010). Production of chromophoric dissolved organic matter by marine phytoplankton. *Limnol. Oceanogr.*, 55, 446–454.
- Romera-Castillo, C., Sarmiento, H., Alvarez-Salgado, X.A., Gasol, J.M., Marrase, C. (2011). Net production and consumption of fluorescent colored dissolved organic matter by natural bacterial assemblages growing on marine phytoplankton exudates. *Appl. Environ. Microbiol.*, 77, 7490–7498.
- Saleh, R., Robinson, E. S., Tkacik, D. S., Ahern, A. T., Liu, S., Aiker, A. C., Sullivan, R. C., Presto, A. A., Dubey, M. K., Yokelson, R. J., Donahue, N. M., and Robinson, A. L. (2014). Brownness of organics in aerosols from biomass burning linked to their black carbon content. *Nature Geoscience*, 7,

36940, <https://doi.org/10.1038/ngeo2220>.

- Seinfeld, J. H., Carmichael, G. R., Arimoto, R., Conant, W. C., Brechtel, F. J., Bates, T. S., Cahill, T. A., Clarke, A. D., Doherty, S. J., Flatau, P. J., Huebert, B. J., Kim, J., Markowicz, K. M., Quinn, P. K., Russell, L. M., Russell, P. B., Shimizu, A., Shinozuka, Y., Song, C. H., Tang, Y., Uno, I., Vogelmann, A. M., Weber, R. J., Woo, J.-H., and Zhang, X. Y. (2004). ACE-ASIA: Regional climatic and atmospheric chemical effects of Asian dust and pollution. *Bulletin of the American Meteorological Society*, 85, 367–380.
- Seo, H., Kim, G. (2020). Rare earth elements in the East Sea (Japan Sea): Distributions, behaviors, and applications. *Geochim. Cosmochim. Ac.*, 286, 19–28.
- Shimotori, K., Omori, Y., Hama, T. (2009). Bacterial production of marine humic-like fluorescent dissolved organic matter and its biogeochemical importance. *Aquat. Microb. Ecol.*, 58, 55–66.
- Shin, H. R., Shin, C. W., Kim, C., Byun, S. K., and Hwang, S. C. (2005). Movement and structural variation of warm eddy WE92 for three years in the western East/Japan Sea. *Deep Sea Res.*, 52, 1742–1762.
- Stedmon, C. A. and Bro, R. (2008). Characterizing dissolved organic matter fluorescence with parallel factor analysis: a tutorial. *Limnology and Oceanography: Method*, 6, 11, 572–579, <https://doi.org/10.4319/lom.2008.6.572>.
- Stedmon, C. A. and Nelson, N. B. (2015). Chapter 10 – The optical properties of DOM in the ocean, in: *Biogeochemistry of marine dissolved organic matter* (Second Edition), edited by: Hansell, D. A. and Carlson, C. A., 481–508, Academic Press, Boston.
- Stein, A. F., Draxler, R. R., Rolph, G. D., Stunder, B. J. B., Cohen, M. D., and Ngan, F. (2015). NOAA's HYSPLIT atmospheric transport and dispersion modeling system. *Bulletin of the American Meteorological Society*, 96, 2059–2077, <https://doi.org/10.1175/BAMS-D-14-00110.1>.
- Stolpe, B., Zhou, Z., Guo, L., Shiller, A. M. (2014). Colloidal size distribution of humic- and protein-like fluorescent organic matter in the northern Gulf of Mexico. *Mar. Chem.*, 164, 25–37.

- Suksomjit, M., Nagao, S., Ichimi, K., Yamadam, T., Tada, K. (2009). Variation of dissolved organic matter and fluorescence characteristics before, during and after phytoplankton bloom. *J. Oceanogr.*, 65, 835–846.
- Talley, L. D., Lobanov, V., Ponomarev, V., Salyuk, A., Tishchenko, P., Zhabin, I., and Riser, S. (2003) Deep convection and brine rejection in the Japan Sea. *Geophysical Research Letters*, 30, <https://doi.org/10.1029/2002GL016451>.
- Talley, L. D., Min, D.-H., Lobanov, V. B., Luchin, V. A., Ponomarev, V. I., Salyuk, A. N., Shcherbina, A. Y., Tishchenko, P. Y., and Zhabin, I. (2006) Japan/East Sea water masses and their relation to the sea's circulation. *Oceanography*, 19, 32–49.
- Tan, J., Xiang, P., Zhou, X., Duan, J., Ma, Y., He, K., Cheng, Y., Yu, J., and Querol, X. (2016) Chemical characterization of humic-like substances (HULIS) in PM_{2.5} in Lanzhou, China. *Science of the Total Environment*, 573, 1481–1490, <https://doi.org/10.1016/j.scitotenv.2016.08.025>.
- Tanata, K., Kuma, K., Hamasaki, K., Yamashita, Y. (2014). Accumulation of humic-like fluorescent dissolved organic matter in the Japan Sea. *Sci. Rep.*, 4, 5292.
- Taylor, S. R. and McLennan, S. M. (1995) The geochemical evolution of the continental crust. *Review of Geophysics*, 33, 241–265, <https://doi.org/10.1007/s10201-006-0194-9>.
- Tedetti, M., Guigue, C., and Goutx, M. (2010) Utilization of a submersible UV fluorometer for monitoring anthropogenic inputs in the Mediterranean coastal waters. *Marine Pollution Bulletin*, 60, 350–362, <https://doi.org/10.1016/j.marpolbul.2009.10.018>.
- Tedetti, M., Longhitano, R., Garcia, N., Guigue, C., Ferretto, N., and Goutx, M. (2012). Fluorescence properties of dissolved organic matter in coastal Mediterranean waters influenced by a municipal sewage effluent (Bay of Marseilles, France). *Environ. Chem.*, 9, 438–449. <https://doi.org/10.1071/EN12081>.
- Troyer, I. D., Bouillon, S., Barker, S., Perry, C., Coorevits, K., and Merckx, R. (2010) Stable isotope analysis of dissolved organic carbon in soil solutions using a catalytic combustion total organic carbon analyzer-isotope ratio mass

- spectrometer with a cryofocusing interface. *Rapid Communications Mass Spectrometry*, 24, 365–374, <https://doi.org/10.1002/rcm.4403>.
- Tsukuda, S., Sugiyama, M., Harita, Y., and Nishimura, K. (2005) Atmospheric bulk deposition of soluble phosphorus in Ashiu Experimental Forest, Central Japan: source apportionment and sample contamination problem. *Atmospheric Environment*, 39, 823–836, <https://doi.org/10.1016/j.atmosenv.2004.10.028>.
- Tsunogai, S., Watanabe, S., Sato, T. (1999). Is there a “continental shelf pump” for the absorption of atmospheric CO₂? *Tellus*, 51B, 701–712.
- Twardowski, M. S., Boss, E., Sullivan, J. M., and Donaghay, P. L. (2004). Modeling the spectral shape of absorbing chromophoric dissolved organic matter *Marine Chemistry*, 89, 69–88, <https://doi.org/10.1016/j.marchem.2004.02.008>.
- Uchiyama, Y., Suzue, Y., and Yamazaki, H. (2017). Eddy-driven nutrient transport and associated upper-ocean primary production along the Kuroshio. *J. Geophys. Res.*, 166, 5046–5062.
- Vetter, T. A., Perdue, E. M., Ingall, E., Koprivnjak, J.-F., and Pfromm, P. H. (2007). Combining reverse osmosis and electrodialysis for more complete recovery of dissolved organic matter from seawater. *Separation and Purification Technology*, 56, 383–387, <https://doi.org/10.1016/j.seppur.2007.04.012>.
- Voliotis, A., Prokeš, R., Lammel, G., and Samara, C. (2017). New insights on humic-like substances associated with wintertime urban aerosols from central and southern Europe: Size-resolved chemical characterization and optical properties. *Atmospheric Environment*, 166, 286–299, <https://doi.org/10.1016/j.atmosenv.2017.07.024>.
- Walker, B. D., Beaupre, S. R., Guilderson, T. P., McCarthy, M. D., and Druffel, E. R. M. (2016). Pacific carbon cycling constrained by organic matter size, age and composition relationships. *Nature Geoscience*, 9, 888–891.
- Walsh, J. J. Rowe, G. T., Iverson, R. L., and McRoy, C. P. (1981). Biological export of shelf carbon is a sink of the global CO₂ cycle. *Nature*, 292, 196–201.
- Wang, S.-L., Chen, C.-T. A., Hong, G.-H., and Chung, C.-S. (2000). Carbon dioxide and related parameters in the East China Sea. *Continental Shelf Research*, 20, 525–544.

- Wang, X.-C., Chen, R. F., and Gardner, G. B. (2004). Sources and transport of dissolved and particulate organic carbon in the Mississippi River estuary and adjacent coastal waters of the northern Gulf of Mexico. *Marine Chemistry*, 89, 241–256.
- Wang, X., Ma, H., Li, R., Song, Z., and Wu, J. (2012). Seasonal fluxes and source variation of organic carbon transported by two major Chinese Rivers: The Yellow River and Changjiang (Yangtze) River. *Global Biogeochemical Cycle*, 26, GB2025.
- Ward, N. D., Bianchi, T. S., Medeiros, P. M., Seidel, M., Richey, J. E., Keil, R. G., and Sawakuchi, H. O. (2017). Where carbon goes when water flows: carbon cycling across the aquatic continuum. *Frontiers in Marine Science*, <https://doi.org/10.3389/fmars.2017.00007>.
- Willey, J. D., Kieber, M. S., Eyman, M. S., and Avery, G. B. (2000). Rainwater dissolved organic carbon: Concentrations and global flux. *Global Biogeochemical Cycle*, 14, 139–148.
- Williams, P. M. and Druffel, E. R. M. (1987). Radiocarbon in dissolved organic matter in the central North Pacific Ocean. *Nature*, 330, 246–248.
- Wozniak, A. S., Bauer, J. E., and Dickhut, R. B. (2012). Characteristics of water-soluble organic carbon associated with aerosol particles in the eastern United States. *Atmospheric Environment*, 46, 181–188, <https://doi.org/10.1016/j.atmosenv.2011.10.001>.
- Xie, X., Chen, Y., Nie, D., Liu, Y., Liu, Y., Lei, R., Zhao, X., Li, H., and Ge, X. (2020). Light-absorbing and fluorescent properties of atmospheric brown carbon: A case study in Nanjing, China. *Chemosphere*, 251, 126350.
- Yamashita, Y., Jaffé, R., Maie, N., Tanoue, E. (2008). Assessing the dynamics of dissolved organic matter (DOM) in coastal environments by excitation emission matrix fluorescence and parallel factor analysis (EEM-PARAFAC). *Limnol. Oceanogr.*, 53, 1900–1908.
- Yamashita, Y., Nosaka, Y., Suzuki, K., Ogawa, H., Takahashi, K., and Saito, H. (2013). Photobleaching as a factor controlling spectral characteristics of

- chromophoric dissolved organic matter in open ocean. *Biogeosciences* 10, 7207–7217.
- Yamashita, Y., Tanoue, E. (2003). Chemical characterization of protein-like fluorophores in DOM in relation to aromatic amino acids. *Mar. Chem.*, 82, 255–271.
- Yamashita, Y., Tanoue, E. (2008). Production of bio-refractory fluorescent dissolved organic matter in the ocean interior. *Nat. Geosci.* 1, 579–582.
- Yan, G. and Kim, G. (2012). Dissolved organic carbon in the precipitation of Seoul, Korea: Implications for global wet depositional flux of fossil-fuel derived organic carbon. *Atmospheric Environment*, 59, 117–124, <https://doi.org/10.1016/j.atmosenv.2012.05.044>.
- Yan, G. and Kim, G. (2015). Sources and fluxes of organic nitrogen in precipitation over the southern East Sea/Sea of Japan. *Atmospheric Chemistry Physics*, 15, 2761–2774, <https://doi.org/10.5194/acp-15-2761-2015>.
- Yan, G. and Kim, G. (2017). Speciation and sources of brown carbon in precipitation at Seoul, Korea: Insights from excitation-emission matrix spectroscopy and carbon isotopic analysis. *Environmental Science and Technology*, <https://doi.org/10.1021/acs.est.7b02892>.
- Yan, G., Cho, H.-M., Lee, I., and Kim, G. (2012). Significant emissions of ^{210}Po by coal burning into the urban atmosphere of Seoul, Korea. *Atmospheric Environment*, 54, 80–85, <https://doi.org/10.1016/j.atmosenv.2012.02.090>.
- Yang, S. L., Xu, K. H., Milliman, J. D., Yang, H. F., and Wu, C. S. (2015). Decline of Yangtze River water and sediment discharge: Impact from natural and anthropogenic changes. *Scientific Reports*, 5, 12581.
- Yoon, S.-T., Chang, K.-I., Nam, S., Rho, T., Kang, D.-J., Lee, T., Park, K.-A., Lobanov, V., Kaplunenko, D., Tishchenko, P., and Kim, K.-R. Re-initiation of bottom water formation in the East Sea (Japan Sea) in a warming world. *Scientific Reports*, 8, 1576, 2018.
- Zepp, R. G., Sheldon, W. M., Moran, M. A. (2004). Dissolved organic fluorophores in southeastern US coastal waters: correction method for eliminating Rayleigh and Raman scattering peaks in excitation-emission matrices. *Mar.*

Chem., 89, 15–36.

Zhong, Y., Bracco, A., Tian, J., Dong, J., Zhao, W., and Zhang, Z. (2017). Observed and simulated submesoscale vertical pump of an anticyclonic eddy in the South China Sea. *Scientific Reports*, 7, 44011.

Abstract (Korean)

대기 및 해수 중 유기물의 기원과 순환을 이해하는 것은 전 지구적 탄소 순환과 기후변화를 이해하는데 매우 중요하다. 대기과 해수의 유기탄소 중에는 상당한 양으로 빛에 반응하는 과학적 특성을 갖는 휴믹한 유기물이 존재하는데, 이러한 유기탄소는 대기에서는 갈색탄소라 하며 해양환경에서는 용존유색유기물이라 부른다. 이러한 대기과 해수 중 유기물의 대부분을 차지하고 있는 용존유기탄소의 기원과 제거 기작, 공급량, 작용은 안정탄소와 방사성탄소의 동위원소, 유색용존유기물과 용존유기탄소의 농도, 생물학적지표, 광학적 특성 등을 조합하여 보다 효과적으로 알 수 있다. 본 연구에서 이러한 생지화학적 추적자의 효과적인 조합을 이용하여 대기과 해수 중 유기탄소의 기원과 공급량, 제거기작을 알아보고자 하였다. 본 연구를 위해 대기 입자 시료는

대기 중 많은 양으로 존재하고 있는 갈색탄소의 기원과 제거 기작은 대한민국 서울에서 1년여 기간동안 관찰연구를 통해 발견되었다. 연구 지역에서 발생하는 갈색 탄소의 기원은 주로 바이오매스 연소에 의한 것으로 알려졌고, 이렇게 발생한 갈색 탄소는 광분해로 인해 대기에서 효과적으로 제거되는 것을 관찰 연구와 실험실 실험에서 모두 증명하였다. 이는 광분해가 대기 갈색 탄소의 질과 양에 크게 영향이 끼친다는 것을 의미하며, 광분해 요소는 이후 대기 연구 및 모

텔링에 중요하게 고려되어야 한다는 점을 시사한다.

해양과 육지가 연결되어있는 연안은 가장 활발한 탄소 순환이 이루어지는 지역이다. 이러한 지역에서 용존유기탄소의 다양한 기원을 구별하는 것은 해양 탄소 순환을 이해하는데 매우 중요하다. 본 연구에서는 안정탄소동위원소와 유기물의 광학적 특성을 이용하여 연안 매립지이며 인공호수인 시화호에서 과잉공급으로 관찰된 용존유기탄소의 기원을 2017년과 2018년 두 계절동안 알아보았다. 연구 지역에서 발생하는 용존유기탄소는 주로 해양 퇴적물에서 생성되는 것으로 밝혀졌고, 2017년에 관찰된 과잉의 용존유기탄소는 육지 기원의 것으로 안정탄소동위원소값과 광학적 특성을 이용하여 밝혔다. 이 육지기원의 과잉의 용존유기탄소는 매립지와 해수의 직접적인 상호작용에 의해 연안으로 공급된 것으로 보인다.

최근, 강물 영향이 지배적인 연안지역에서 대륙붕 기원의 용존유기탄소의 공급은 많은 관심을 받아왔다. 그러나, 강물의 영향이 배제된 지역에서의 대륙붕 생성 유기물의 영향과 공급량에 대해서는 연구가 진행되지 않았다. 본 연구에서는 전지구적으로 가장 큰 대륙붕 중의 한 곳으로 알려진, 동중국해와 황해에 위치해 있는 대륙붕에서 용존유기탄소의 기원과 공급량을 안정탄소동위원소, 방사성탄소동위원소과 유색용존유기물의 농도를 이용하여 알아보았다. 여름철 황해에서 관측되는 용존유기탄소의 경우 양자강 기원의 것으로 보이

며, 더욱 높은 농도로 관측되는 겨울과 봄철 용존유기탄소는 주로 대륙붕에서 생성된 것으로 보이며, 대륙붕 생성 용존유기탄소의 공급량 ($2.2 \pm 0.6 \text{ Tg C yr}^{-1}$)은 양자강에서 공급되는 탄소의 양 (1.6 Tg C yr^{-1})과 거의 유사하거나 훨씬 많은 양이 동중국해로 공급되는 것으로 보인다.

동해는 북서태평양에 위치한 반폐쇄성 해역으로 전 대양의 축소판으로도 불린다. 동해 남부 해역에서 발생하는 난수성 소용돌이에 의한 표층 용존유기탄소의 심층으로의 유입이 발견되었으며, 휴믹한 용존유색유기물의 경우 약 90%가 수층에서 미생물 활동에 의해 생성되고, 약 10%가 심층 퇴적물 내 무산소 기작에 의해 생성되는 것으로 나타났다. 특히, 표층에서는 육지 기원의 휴믹한 유색용존유기물과 해양기원의 휴믹한 유색용존유기물이 서로 다른 거동을 보였는데, 이는 육지 기원의 휴믹한 유색용존유기물이 해양기원의 휴믹한 유색용존유기물보다 광분해에 의해 빠르게 제거되거나 비교적 낮은 해양기원의 휴믹한 유색용존유기물의 생산량 때문으로 보인다. 따라서, 동해 유색용존유기물의 분포는 수직 혼합과 표층 광분해와 저층 생산량의 영향을 받는 것으로 보인다.

본 연구는 대기 및 다양한 해양 환경에서 여러 생지화학적 추적자를 사용하여 용존유기탄소의 기원과 거동에 대한 이해와 공부에 중요한 의미를 알아냈다. 이러한 추적자의 조합은 이후 다양한 환경

에서보다 보다 효과적으로 유기탄소의 기원과 거동을 아는데 사용될 수 있다.

주요어: 용존유기물, 용존유기탄소, 갈색탄소, 안정탄소동위원소, 방사성탄소동위원소, 광학적특성

학번: 2017 - 30218